DEFORMATION MECHANISMS IN PD NANOWHISKERS

Lisa YingYing Chen

A DISSERTATION

in

Materials Science and Engineering

Presented to the Faculties of the University of Pennsylvania

in

Partial Fulfillment of the Requirements for the

Degree of Doctor of Philosophy

2014

Supervisor of Dissertation

_____

Daniel S. Gianola, Skirkanich Assistant Professor of Innovation, MSE

Graduate Group Chairperson

_____

Shu Yang, Professor, MSE

Dissertation Committee

Robert Carpick, John Henry Towne Professor and Chair, MEAM

I-Wei Chen, Skirkanich Professor of Innovation, MSE

Vaclav Vitek, Harold Pender Professor, MSE

DEFORMATION MECHANISMS IN PD NANOWHISKERS

COPYRIGHT

2014

Lisa YingYing Chen

To my parents and to Joseph

ACKNOWLEDGMENT

The work encompassed in this thesis would not have been possible without the support and contributions of many others. First and foremost I would like to thank my advisor Dr. Daniel Gianola for taking me on as one of the first PhD students in the group and supporting me with boundless enthusiasm and a reservoir of patience. These qualities along with his experimental lab savvy, breadth of knowledge, and uncanny communication skills inspired me throughout my time at Penn. I did not always make things easy for you due to my natural talent to overload on external commitments and the occasional damage to expensive equipment, but you always stood by me and enabled me to overcome my weaknesses and further bolster my strengths. You also has a clear sense of fun, having provided funding via the NSF CAREER grant (NSF-DMR 1056293) for my European escapades and late night parties in LRSM, Singh, and what was once known as Edison. Thank you!!!

It was a great experience to be part of a small new group and see it grow over the years. Many thanks to the current and former members of the Gianola group for being such a supportive team and bearing with my super-long presentations and bad science jokes. I would especially like to recognize Dr. Kathryn Murphy, who has been in this group with me since the beginning. Together we were partners in crime seeking out the mysterious arts of wire bonding, nanowire manipulation, metallic adhesives, and Matlab. I have also had the privilege of working with TEM guru Dr. Mo-Rigen. Your

was really crucial to keeping me sane in the worst of times. Thank my committee members, Professors Carpick, Chen, and Vitek, who have been invested in my success since I first stepped on campus. As my teachers they provided the fundamentals to start my research and as my thesis committee they provided the feedback I needed to finish it. Also thanks to the faculty at Penn for providing support and guidance throughout the years, including Profs. Peter Davies and Vivek Shenoy. Many endless thanks to Irene Clements, Patricia Overend, Vicky Lee, Fred Hellmig, and Enrique Vargas for ensuring that I was well-fed, had health insurance, and did not freeze to death, and in general providing the organization needed to make things easy for the rest of us; and to Steve Szewczyk, who has been an endless reservoir of lab equipment expertise and technical knowledge. I am also truly grateful for the friendships with my doctorate colleagues, because even if no experiments were working out on a given day, lunch or coffee hour usually would. Additionally, many of you have put up with my bizarre scientific and technical questions or provided assistance (and equipment) that has been crucial to my research, so I would like to take the chance to expression my appreciation to: Rahul Agarwal, Dr. Carlos Aspetti, Dr. Chi-Mon Chen, Vicky Doan-Nguyen, Dr. Tevis Jacobs, Dr. Mark Licurse, Dan Magagnosc, Pavan Nukala, Dr. Michael O'Reilly, Dr. Brian Piccione, Matt Puster, Frank Streller, Danny Strickland, Walter Tung, Spencer Thomas, and Sharon Wang.

Thank you to Jeff Barnes, who woke up after a crazy night in Beijing to listen to me rant on Skype about the power of palladium and reacting positively to some of my crazy science ideas when all I could think to myself was "No, no, no." Thank you again

to Dr. Kathryn Murphy, this time for read part of this thesis, providing valuable feedback, and assuring me that I am almost there and will in fact make it!

Finally, I want to express my gratitude, appreciation, and love for those closest to me. I would like to thank my mom and dad for being supportive throughout this entire time, especially when times were difficult. My dad was my inspiration for taking on a PhD, having overcome many difficulties in life to ultimately reach the success and renown he has now through hard work and passion. Having known how much harder to come by the opportunity was for you makes me even more appreciative than before of how privileged I am. My mom has made many sacrifices to make my life better, and I will never be able to thank her enough. You truly are the strongest person I know, and any given day when I feel that the odds are against me, just thinking about you and your strength on our family's behalf enables me to pull through. Last but never least, thank you Joseph for not just proofreading this whole thing, but for the love and support that you have given me throughout this crazy time. I am not sure what it was that I did that was so wonderful that allowed me to have you in my life, but let it be known that I am one lucky lady.

Also, as of November 4, 2014, you no longer have the privilege to lord it over me that you have a doctorate degree and I do not.

ABSTRACT

DEFORMATION MECHANISMS IN PD NANOWHISKERS

Lisa Y. Chen

Daniel S. Gianola

The reduced length scales inherent in nanoscale materials enable access to properties that are otherwise not achievable in bulk. The application of their novel structural and functional responses however is hindered by a lack of understanding of their mechanical behavior, which affects their assimilation into device fabrication as well as their reliability during performance. In contrast to bulk materials, nanoscale materials possess a non-negligible proportion of surface atoms, which can exert significant influence on the overall mechanical response. In addition, structures with small volumes can possess much lower defect densities, which could potentially be driven out of the volume instead of interacting and promoting traditional deformation behavior. Systematic experimental investigations will be crucial to developing the necessary understanding, although they remain challenging due to limited access to suitable test specimens and testing methodologies for directly extracting pertinent results. By employing a MEMS-based tensile testing system and a temperature-controlled cryostat configuration to test defect-free and –scarce Pd nanowhiskers, we have been able to

systematically investigate some of the important deformation mechanisms in nanoscale single crystals.

We first address the elastic behavior in nanoscale crystals, which is predicted to differ from bulk behavior due to the reduced coordination of surface atoms. We measured size-dependent deviations from bulk elastic behavior in nanowhiskers with diameters as small as ~30 nm. In addition to size-dependent variations in Young's modulus in the small strain limit, we measured nonlinear elasticity at strains above ~1%. In addition to providing the first measurements of higher-order elasticity in Pd, our study shows that the elasticity response in Pd nanowhiskers can be attributed to higher-order elasticity in the bulk-like core upon being biased from its equilibrium configuration due to the role of surface stresses in small volumes. Comparison of the size-independent values of δ in our nanowhiskers with studies on bulk FCC metals lends further insight into the role of length scales on both elastic and plastic mechanical behavior.

We then consider incipient plasticity in nanoscale Pd nanowhiskers, which is governed not by the initial motion of pre-existing dislocations but rather the nucleation of dislocations. Whereas nucleation strengths are weakly size- and strain-rate-dependent, strong temperature dependence is uncovered, corroborating predictions that nucleation is assisted by thermal fluctuations. We measure activation volumes as small as singular atomic volumes, which explain both the ultrahigh athermal strength as well as the temperature-dependent scatter, evident in our experiments and well captured by a thermal activation model. Our experiments highlight the pronounced probabilistic nature of

surface dislocation nucleation, which is crucial input to device design using nanoscale building blocks.

In total, this body of work demonstrates that distinctly different processes are responsible for the deformation behavior in small volumes and underscores the importance of comprehensive characterization of material properties at the relevant length scales.

TABLE OF CONTENTS

LIST OF TABLES

LIST OF ILLUSTRATIONS

1 Introduction

Technological progress requires not only access to suitable materials but also a thorough understanding of their properties – both the mechanisms by which they operate as well as how to tune these properties. One of the earliest examples of the manipulation of materials to achieve superior properties can be traced back to the Bronze Age, where the introduction of tin into copper produced an alloy with much higher strength than any known pure metals [1]. Prior to the 19th century, progress was limited to a small pool of known materials and empirical knowledge of their properties; however, over the past century, systematic study of structure-property relationships has provided the knowledge essential to enabling deliberate and informed modification of material characteristics [2]. Examples of this stepwise progress include the development of the iron-carbon phase diagram [3] and the discovery of high electrical conductivity at elevated temperatures, which marked the beginning of research into semiconductors [4]. More recently, the ability to assemble materials – and thereby control their properties – at length scales near the atomic level has catalyzed many of the discoveries that have shaped the field of nanotechnology.

The growing interest in nanoscale materials is not driven only by a desire to create smaller, more portable and energy efficient devices but also to take advantage of the material properties that arise in extremely small structures. These include quantum confinement effects resulting in novel optical, electronic, and chemical characteristics,

such as high quantum yield fluorescence [5] and enhanced surface catalytic activity [6]. Superior mechanical properties exhibited by numerous material systems such as metal nanostructures and carbon nanotubes mark them as prime components for flexible electronics [7,8]. Additionally, structures at submicron length scales can interact directly with biological systems, and are thereby suited for potential life-saving applications such as drug delivery and early disease detection [9,10].

Many of the applications envisioned for these building blocks entail extreme environments and large or cyclic mechanical loads [11–16]. Like many other properties, the mechanical response differs greatly from bulk behavior, and a lack of understanding of the processes responsible for elastic and plastic deformation at the nanoscale is a detriment to device design and material modifications. Yield strength measurements in many material systems, including metals, ceramics, and semiconductors, have indicated deviation from bulk values even at micron length scales, as demonstrated early on by mechanical tests on whisker specimens [17–21]. Even with critical dimensions limited to microns, these structures exhibited roughly an order of magnitude greater strength than bulk. This high strength behavior was attributed to limited population of critical defects or weak spots in smaller volumes, supported by the increasingly higher strengths exhibited by testing subsequently fractured whisker segments [17,22]. Moreover, since the strength limit was determined by a much more discrete distribution of flaw strengths, measured strengths within even the same batch of materials exhibited large scatter, requiring new approaches in characterizing mechanical strength in order to account for this stochasticity [17,23].

The nanoscale brings more challenges to the forefront in understanding the deformation behavior in relevant materials. In particular, surface properties, including surface stresses and reconstructions, are expected to be very important in dictating deformation behavior in both the elastic and plastic regimes [24–28]. Material properties that were once considered immutable, such as the Young's modulus, may display deviations not only due to size [29–33] but also higher-order effects that are expected at very large strains, which are accessible due to high strength [25,34,35]. Additionally, in the extreme limit where materials can be assembled into structures free of the defects that lower their strength in bulk, plastic deformation or fracture must proceed by alternative means [13,27,36–38]. Experimentally investigating these processes is often very challenging: access to high quality samples possessing the appropriate structure to target a specific inquiry (e.g. deformation in defect-free materials) is often a foremost obstacle to carrying out these studies [17,22,39]; even with the right model material, the process of harvesting, aligning, and securing specimens for testing is highly rate-limiting; and the lack of already standardized, suitable testing platforms and procedures necessitates the development of new methods and tools [40–45].

The purpose of this work is to provide further insight into the processes and mechanisms governing specific deformation responses in nanoscale crystalline materials. Due to widespread technological interest in the structural and functional properties of metal nanostructures, our experimental study focuses on the deformation mechanics of Pd nanowhiskers (NWs). In this first chapter, we cover some of the fundamentals of

deformation behavior in crystalline solids and provide context for the specific questions

we aim to address.

1.1   Fundamentals of Elastic Deformation

While there are many methods that can be used to characterize the mechanical

response of a material, the tensile test is the most widely used. This involves applying

uniaxial load to a given specimen, from which many of the most fundamental properties

and deformation characteristics of a material can be directly obtained by evaluating the

relationship between stress and strain. For a uniaxial load P, the stress σ over the

specimen's initial cross section A_0 is:

$$\sigma = \frac{P}{A_0}$$ **Eq. 1-1**

The response to the load will be an elongation of original length l_0 to final length l, and

the difference is the strain ε:

$$\varepsilon = \frac{l - l_0}{l_0}$$ **Eq. 1-2**

Up to a certain displacement, the mechanical response will be elastic, where upon release

of the load the specimen will return to its original configuration.

For many materials, including metals, ceramics, and semiconductors, the initial

elastic regime is defined by a linear correlation between stress and strain (or load and

displacement), much like an ideal spring. Hence, Hooke's Law, which relates force and

4

displacement in an ideal spring, can be rewritten to relate stress and strain through the material stiffness E, known as Young's modulus:

$\sigma = E\varepsilon$ **Eq. 1-3**

While the Young's modulus is considered a fundamental material property, Eq. 1-3 represents a very specific case of uniaxial tension applied to an isotropic or randomly-oriented polycrystalline sample; however, most engineering materials are elastically anisotropic and many applications involve non-uniaxial loading states. In general, the stress and strain are symmetric second-rank tensors related through the stiffness tensor C_{ijkl} (or its inverse, the compliance tensor S_{ijkl}), where:

$$\sigma_{ij} = \sum_{k=1}^{3}\sum_{l=1}^{3} C_{ijkl}\varepsilon_{kl}$$ **Eq. 1-4**

$$\varepsilon_{ij} = \sum_{k=1}^{3}\sum_{l=1}^{3} S_{ijkl}\sigma_{kl}$$ **Eq. 1-5**

Due to the symmetry of the stress and strain tensors (e.g. $\varepsilon_{12} = \varepsilon_{21} = \varepsilon_{xy}$), C_{ijkl} and S_{ijkl} can be reduced from the original 81 terms to 36 independent components. Additionally, in the case of the cubic crystal lattice, there are only three independent components which can be related to stress and strain in the three orthogonal directions:

$$\begin{bmatrix} \varepsilon_{xx} \\ \varepsilon_{yy} \\ \varepsilon_{zz} \\ \varepsilon_{xy} \\ \varepsilon_{yz} \\ \varepsilon_{xz} \end{bmatrix} = \begin{bmatrix} S_{11} & S_{12} & S_{12} & 0 & 0 & 0 \\ S_{12} & S_{11} & S_{12} & 0 & 0 & 0 \\ S_{12} & S_{12} & S_{11} & 0 & 0 & 0 \\ 0 & 0 & 0 & S_{44} & 0 & 0 \\ 0 & 0 & 0 & 0 & S_{44} & 0 \\ 0 & 0 & 0 & 0 & 0 & S_{44} \end{bmatrix} \begin{bmatrix} \sigma_{xx} \\ \sigma_{yy} \\ \sigma_{zz} \\ \sigma_{xy} \\ \sigma_{yz} \\ \sigma_{xz} \end{bmatrix}$$ **Eq. 1-6**

With the three independent components, one can then calculate the Young's modulus for a single crystal:

$$\frac{1}{E} = S_{11} - 2\left[(S_{11} - S_{12}) - \frac{1}{2}S_{44}\left(l_1^2 l_2^2 + l_2^2 l_3^2 + l_3^2 l_1^2\right)\right]$$ **Eq. 1-7**

Where l_1, l_2, and l_3 are direction cosines relative to the <100> direction.

1.2   Higher-order and Size-dependent Elasticity

The magnitudes of the stiffness or compliance tensor components are related to the interatomic potential, which results from a balance of the long-range attractive and short-range repulsive forces between atoms. This minimum of this sum corresponds to zero net force and determines the equilibrium spacing between atoms; hence, a periodic arrangement of this minimum determines the structure of the crystal lattice. The stiffness associated with displacing a fully-coordinated atom from its equilibrium position is related to the curvature of this potential. Hence, for displacements that do not deviate far from the equilibrium position, this stiffness, defined by the curvature $\left.\frac{\partial^2 U}{\partial x^2}\right|_{x=x_0}$, is assumed to be constant (Figure 1-1) [46].

6
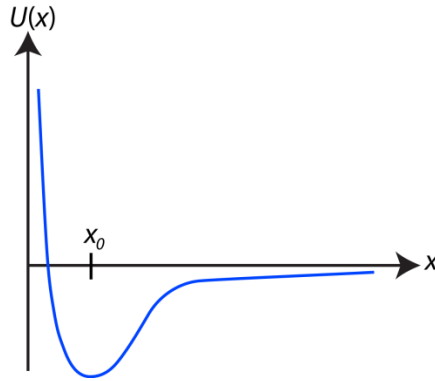
Figure 1-1 Schematic of the interatomic potential energy curve. The curvature of the potential energy minimum determines the (low-strain) elastic stiffness.

In reality, the elasticity of a crystalline material is a function of strain, becoming nonlinear at higher strains, and is directly tied to lattice anharmonicity (Figure 1-2).
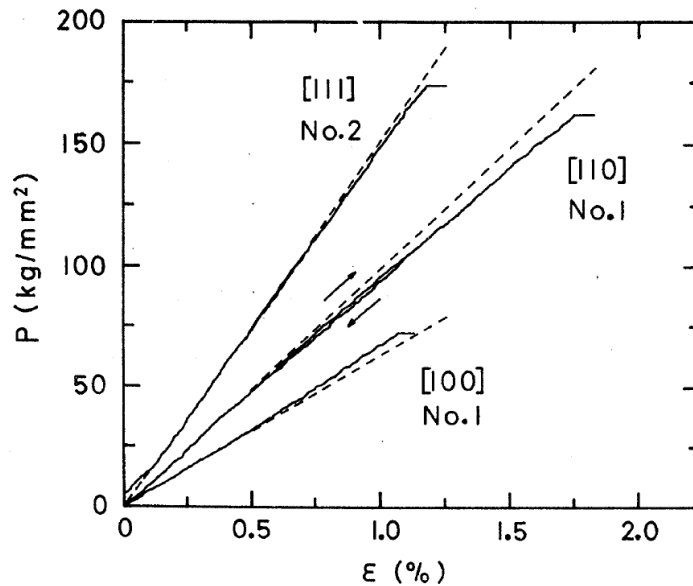
Figure 1-2 Nonlinear elasticity measured in Cu whiskers. From Ref. [34]. Copyright 1973 by The American Physical Society)

7

Several important material properties are defined by this anharmonic regime, including thermal expansion [46–48], phonon interactions [46,49,50], and temperature- and pressure-dependence of elastic constants [51–53]. Measurements of anharmonicity in bulk materials have often been performed through ultrasound velocity measurements or microwhisker tensile testing, the latter of which requires the introduction of large stresses. For mechanical testing, the constitutive relationship of Eq. 1-3 can be expanded to account for higher-order effects:

$$\sigma = E\varepsilon + D\varepsilon^2 + \cdots \qquad \textbf{Eq. 1-8}$$

We note that this relationship has been used in evaluating the large-strain elastic response of other nanostructures such as graphene [26,35,54]. D can be expressed in terms of the third-rank stiffness tensor C_{iklmn}, which has six independent terms for cubic crystals [55]. Assuming that v, the ratio between the transverse and axial strains, is the same for both transverse directions and expressing C_{iklmn} in Voigt notation:

$$D = C_{111} + 4vC_{112} + 2v^2C_{112} + 2v^2C_{123} \qquad \textbf{Eq. 1-9}$$

Likewise, an inverse relationship can be developed for strain as a function of stress:

$$\varepsilon = \left(\frac{\sigma}{E}\right) + \delta\left(\frac{\sigma}{E}\right)^2 \qquad \textbf{Eq. 1-10}$$

Here, nonlinearity is characterized by the stress-expanded parameter δ [49,56,57].

As shown in Table 1-1 for various FCC metals, the measured nonlinearity is both material- and orientation-dependent. While it has been feasible to quantify the nonlinearity in a number of materials, these experiments are very much limited by the onset of plastic relaxation mechanisms that occur at low stresses relative to the nonlinear elastic regime [34]. Recent advances in mechanical testing allow for investigating the response of nominally defect-free crystalline nanostructures in which stresses near theoretically predicted levels are required for plasticity to occur [40,44,58], although rarely has nonlinear elasticity's role at the nanoscale been addressed.

Table 1-1 Nonlinearity parameters for different FCC transition metals determined either directly from tensile stress-strain data or indirectly from calculations using second- and third-order elastic constants from sound velocity measurements.

Element	δ_{100}	δ_{110}	δ_{111}	Method
Cu	-4.4	8.9	2.1	Tensile testing – whiskers [59]
Ag	-3.7	8.5	---	Tensile testing – whiskers [57]
Au	-4.51	10.57	3.73	Sound velocity [60]
Ni	-3.33	2.88	2.11	Sound velocity[a] [56]

[a] These δ values were actually calculated from the second- and third-order elastic constants of two separate studies, as opposed to being directly measured from the same body of experiments.

Despite the lack of understanding of nonlinear elasticity, nanoscale volumes comprising large fractions of miscoordinated atoms residing at surfaces and interfaces are expected to play an increasingly important role in deformation behavior. Nanostructures such as thin films and nanowires are essentially composites of atomically miscoordinated surfaces (and edges) encompassing a bulk-like core; therefore, it should be expected that

the relative contributions of surface and bulk effects on elastic behavior are roughly correlated to the surface-to-volume ratio [26,35,61].

In investigating material properties at the nanoscale, observed deviations from bulk behavior are often analyzed within the framework of surface contributions attributed to the reduced number of nearest neighbors at the surface [32,62–65]. Similar to a liquid, there is a surface energy γ associated with the reversible work to create a new surface as well as a surface stress τ to elastically stretch the surface [65]. Whereas in a liquid, $\gamma = \tau$ because atoms can readily flow to the surface and maintain a constant areal density, this is not the case in a solid, where the number of atoms remain the same while the area changes. Rather, the quantity of the surface stress will be dependent on the strain and can be related to the surface energy as follows:

$$\tau(\varepsilon) = \gamma + \frac{\partial \gamma}{\partial \varepsilon} \qquad \qquad \textbf{Eq. 1-11}$$

Because the bonding environment is different at the surface, both the equilibrium spacing of surface atoms as well as the stiffness of the bonds between atoms will be different from the of fully-coordinated bulk atoms. The latter is accounted for by modeling the various structures as composites, e.g. bulk-like core encapsulated in a shell with different elastic properties [32]. The consequence of the former is a surface-induced initial stress state in the bulk: in perfect registry with the bulk, a surface will have an initial stress τ_0, which can be relaxed elastically with strain induced in the bulk [30,32].

$$\tau(\varepsilon) = \tau_0 + S\varepsilon \qquad \qquad \textbf{Eq. 1-12}$$

These surface effects have been considered in a number of analytical continuum models [30–32,66–69] as well as atomistic simulations [25,32,70]. While these models have demonstrated how size-dependent elastic behavior can manifest for very small sample dimensions, the critical chracteristic length scale at which deviations from bulk occur is about 10 nm or smaller, which is much smaller than the sizes at which changes in apparent elastic behavior occur [29,32,33] (Figure 1-3). McDowell *et al.* performed atomistic simulations to investigate the influence of features in real nanowires such as surface roughness and faceting and found that these could not account for the observed experimental behavior [71].

Within the body of experimental literature there are also many contradictions. Most experimental studies on the size-dependent elastic behavior of nanowires have employed bending or resonance tests and yielded very different results even within the same material (Figure 1-3) [67–69,72–79]. For example, studies on various Ag nanowires have identified both size-dependent [69,72] and –independent [75] deviations from bulk E as well as no deviations at all [77]. Some of the discrepancies can be attributed to the measurement methods, such as the poorly defined boundary conditions and increasing axial strains when performing bending tests [75,77]. Additionally, sample quality is important in these tests with respect to contamination and surface roughness have been cited as issues in some of these experiments [29,69].
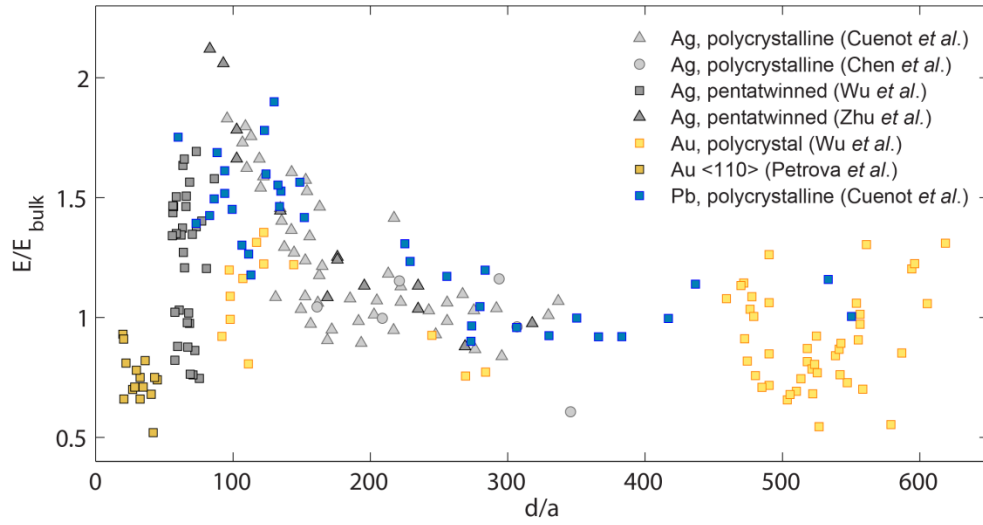
Figure 1-3 Measurements of apparent elastic modulus in FCC nanowires. For comparison purposes, elastic modulus values E and nanowire diameter d are normalized with respect to the bulk Young's modulus E_{bulk} and lattice parameter a. Data included are from Refs. [67,68,72,74,77,80].

However, a primary limitation present in most studies, both experimental and theoretical, is that they only address changes in the linear elastic behavior. Given the significant relaxation strains these structures can undergo, there has been a push to incorporate higher-order elasticity in order to more accurately reflect material behavior [81−83]. In particular, a number of studies using molecular statics have proposed that bulk nonlinear elasticity is the source of size-dependent changes in elastic modulus in nanowires undergoing high surface-induced relaxations [26,35,82]. Since the surface stress would drive the bulk to compressively relax for very small diameters, the apparent elastic modulus of a nanowire is directly related to the strain to which it relaxes. This *relaxation* strain, measured by the difference between the compressed and unstrained lattice parameter along the axial direction, is directly correlated with the elastic modulus in the bulk material at the same *applied* strain (Figure 1-4). Thus for orientations with

very large nonlinearity, the apparent elastic modulus of the nanowire changes rapidly as a function of size.
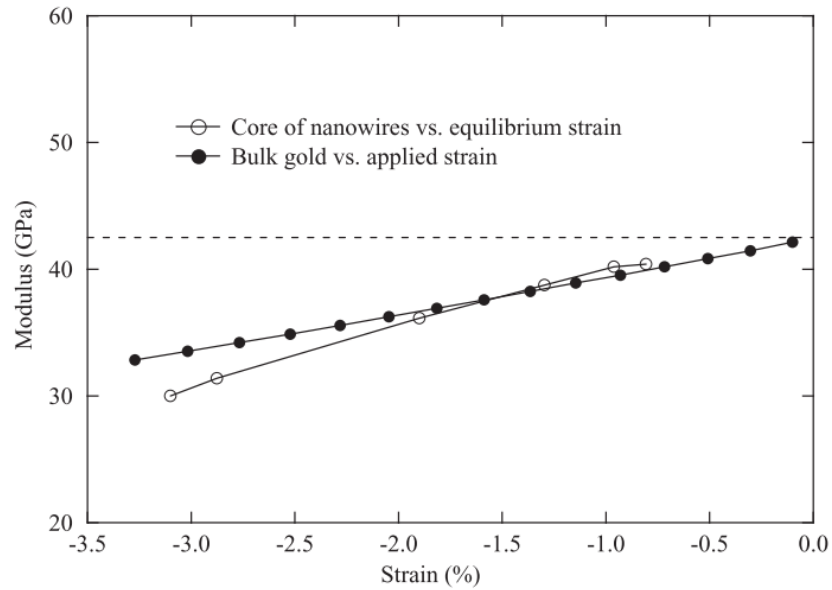
Figure 1-4 Direct correlation between nonlinear elasticity of bulk gold and the stiffness of gold nanowire cores under different relaxation or equilibrium strain, from Ref. [26] (Copyright 2004, with permission from Elsevier).

Both anharmonicity and increasing surface influence are expected to be important for elastic behavior at large strains in nanoscale materials. Moreover, if the small-strain elastic behavior is affected by relaxation, the apparent elastic behavior at large strains should be as well, and this effect has not been considered at all either computationally or experimentally. Such experiments would provide new insight into the mechanisms governing elasticity at reduced dimensions, and greater understanding of the interactions between bulk-like interiors and surfaces could also potentially inform on mechanical behavior beyond the elastic regime.

1.3 Plastic Deformation in FCC Metals

When sufficient load is applied to a material, it can no longer sustain elastic deformation and permanently deforms. In an ideal crystal, this is the load required to shear or separate two atomic planes and is therefore directly related to the strength of interatomic bonds. This is illustrated in Figure 1-5 where the top row of atoms are moving to the right with respect to the bottom row. As mentioned in the last section on the interatomic potential, the equilibrium positions correspond to minima in the potential energy. Thus the potential energy as a function of displacement, as well as the stress required to move to each position, can be approximated by a sinusoidal curve. The latter can be expressed with respect to the maximum theoretical shear strength τ_{th} and equilibrium interatomic spacing b as

$$\tau(x) = \tau_{th} \sin \frac{2\pi x}{b} \qquad\qquad \textbf{Eq. 1-13}$$
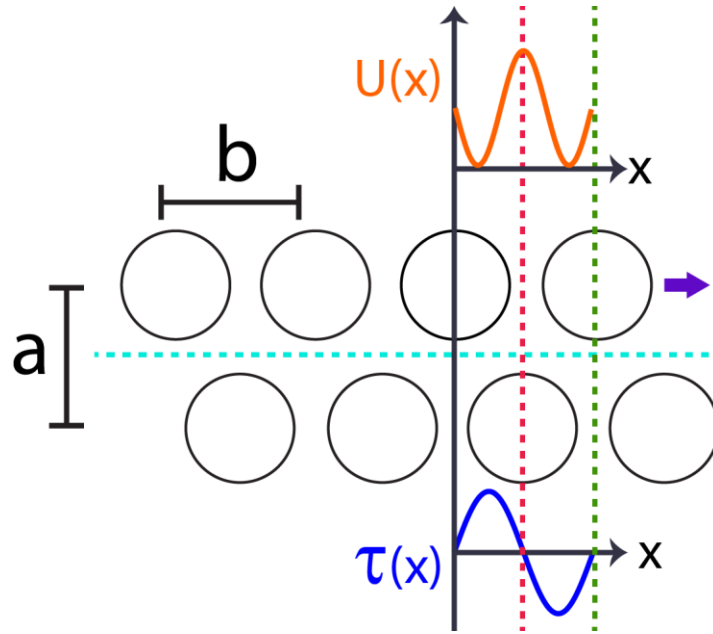
Figure 1-5 Schematic of the periodic nature of the lattice. $U(x)$ represents the potential energy as a function of position, $\tau(x)$ represents the corresponding shear stress required to move the top row of atoms to the right (purple arrow), and a and b are the interplanar and equilibrium interatomic spacings, respectively.

For shear deformation, the relationship between τ and shear strain γ

$$\tau = \mu\gamma \qquad\qquad \textbf{Eq. 1-14}$$

Where μ is the shear modulus, the elastic stiffness within the shear plane. For small displacements, $\gamma \approx x/a$, where a is the interplanar spacing (Figure 1-5). By equating Eq. 1-13 and Eq. 1-14 and approximating $\sin\dfrac{2\pi x}{b}$ as simply $\dfrac{2\pi x}{b}$ for small strains, one obtains

$$\tau_{th} \approx \frac{\mu b}{2\pi a} \qquad\qquad \textbf{Eq. 1-15}$$

Since for most crystals, *a* and *b* are of the same order, Eq. 1-15 can be simplified to yield an approximation of the theoretical shear strength of a perfect crystal:

$$\tau_{th} \approx \frac{\mu}{2\pi}$$ **Eq. 1-16**

For most common metals employed in structural applications, τ_{th} is on the order of 1-20 GPa; however, the experimental yield strengths for bulk materials can be lower by up to 4 orders of magnitude [84]. This is due to the presence of pre-existing defects that initiate permanent deformation at much lower applied stress and dramatically affect the plastic response. Line defects known as dislocations are one of the most important defects in crystalline materials and have been crucial for elucidating the properties and mechanical response of crystalline materials. Even before the invention of the transmission electron microscope (TEM) that facilitated direct observations of such defects [85,86], the concept of dislocations as a mechanism explaining the discrepancy between the theoretical strength in perfect crystals and the actual measured strength in real crystals was developed [87–90]. While it is widely known for explaining the ductile behavior and work hardening abilities in metals relevant to structural applications for many centuries prior, it has also informed other poorly understood phenomena in crystalline materials such as rapid crystal growth [91–93] and the occurrence of "mosaic" microstructures [94].

The structural role of dislocations extends well beyond plastic deformation and flow: for example, their organization within grains and at grain boundaries are important for facilitating diffusion-less phase transformations [95] and governing corrosion

behavior in alloys [96]. In functional settings, dislocations can alter the electronic properties in semiconductor [97] and piezoelectric materials owing to the perturbation of the otherwise perfect lattice in the vicinity of the defect, which can introduce distinct electronic states or induced local electric fields. Indeed, dislocations have been reported to degrade optoelectronic response in epitaxially layered systems such as heterojunction solar cells and light emitting diodes [98], augment phase change behavior in electronic memory devices [99], and limit electron mobility enhancements in strained field effect transistors [100]. Rational device design with long-term reliability in mind, thus, hinges on a thorough scientific understanding of dislocations.

Dislocations move by breaking one "line" of atomic bonds at a time rather than all bonds at once in order to shear a crystal across a plane (Figure 1-6).
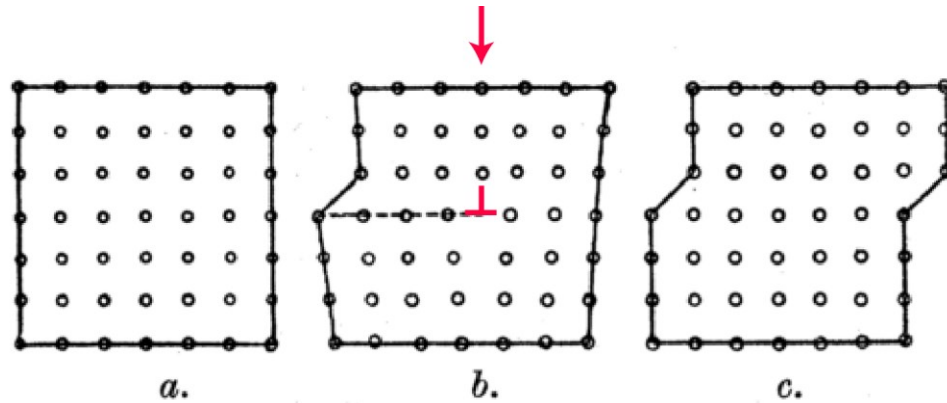
Figure 1-6 Schematic of dislocation slip. Beginning with a perfect single crystal in (a), slip between the top and bottom half commence from the left. The slip plane extends in and out of the page along the dotted line in (b) and the slip direction is towards the right. The red arrow indicates the "half-plane" structure characteristic of edge dislocations and the edge dislocation symbol ⊥ represents the core of the dislocation line, which extends into the page. Finally in (c) the edge dislocation has fully sheared the crystal and exited from the opposite site. (Adapted from Ref. [87], Copyright 1934, The Royal Society).

The plane and crystallographic direction in which the dislocation operates defines the slip system and corresponds to the shortest and least resistive paths between equilibrium positions, which often is in the close-packed direction in the close-packed plane. For FCC materials, the slip system for a full dislocation is in the {111} plane along the $[\bar{1}01]$ direction; however, it is also possible to travel the same net path on {111} via two sequential partial dislocations along $[\bar{2}11]$ and $[\bar{1}\bar{1}2]$ (Figure 1-7). The magnitude and direction of lattice distortion resulting from slip in these systems is quantified in their Burgers vector, $b = \frac{a}{2}[01\bar{1}]$, and $b = \frac{a}{6}[\bar{2}11]$ and $b = \frac{a}{6}[\bar{1}\bar{1}2]$, respectively, where a is the lattice parameter. Since the strain energy associated with the lattice distortions $E \propto \mu b^2$, in the absence of other obstacles the dissociation of the full dislocation is more energetically favorable [84]. Given that the leading and trailing partials have similar vector components, they will tend to repel each other and create stacking faults, regions where the atomic stacking order changes to that of hexagonal close-packed crystals [84]. Since the change in stacking can increase the total energy of the crystal, the separation between the partials is balanced by this energy gain and is thus inversely proportional to the stacking fault energy γ_{SF} [101]:

$$d = \frac{\mu b_1 b_2}{2\pi \gamma_{SF}} \qquad\qquad \textbf{Eq. 1-17}$$

Where b_1 and b_2 are the partial dislocation burgers vectors indicated in Figure 1-7. If partials nucleate on successively adjacent planes, this creates a twin, where the original crystal orientation is reflected about the interfacing {111} plane. Given the abundant

number of slip systems in bulk FCC metals, twinning during deformation is rarely observed except at high strain rates and cryogenic temperatures [2,84].
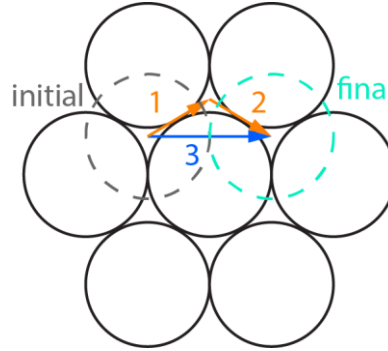
Figure 1-7 Slip on a {111} FCC plane. An atom at the initial position can reach the final position by either slipping via two partial dislocations (paths 1 and 2 together) or a full dislocation (path 3).

Whereas the creation of a dislocation in a pristine lattice via nucleation would require strengths near τ_{th}, dislocations are often already formed during the fabrication and processing of bulk materials require a much lower critical level of stress to mobilize. For a given applied tensile load σ, the resolved shear stress τ_{RSS} is:

$$\tau_{RSS} = \sigma \cos \phi \cos \lambda \qquad \textbf{Eq. 1-18}$$

Where ϕ is the angle between the tensile direction and the normal of the slip plane and λ is the angle between the slip and tensile directions.

For ductile materials, once it yields it will undergo plastic flow over a large strain range, which consists of two components [102]. The first involves the long-range elastic interactions between dislocations and features of the microstructure, including grain

boundaries and other dislocations. Their strength varies primarily with the elastic constants of the lattice and therefore is rather weakly dependent on temperature. The second contribution to flow occurs when dislocations encounter local obstacles, which must be overcome with a combination of very high stresses as well as thermal vibrations in the lattice [103]. While localized over small volumes, these thermally activated processes are important as they are the primary origins for temperature dependence in measured flow stresses of materials.

1.3.1 *Thermally Activated Plastic Flow*

These local glide events are often modeled within the framework of transition state theory (TST) [103–106], which describes the kinetic process of going from one stable equilibrium state to another [107]. The progress of advancement from the initial to the final state is measured by the reaction coordinate, and between the initial and final states is a local maximum that corresponds to an activated configuration [108]. The energy difference between the initial state and the activated state is the activation energy Q_{act} (Figure 1-8).
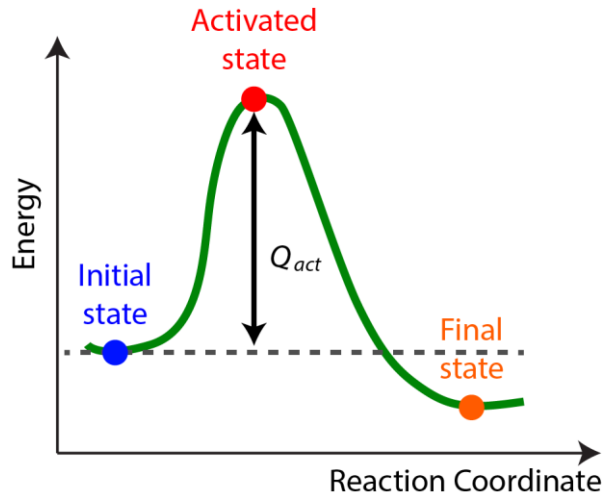
Figure 1-8 Schematic of energy along the reaction coordinate for a thermally activated process.

In the full configurational space, this maximum is in fact a saddle point, i.e. it is the peak of the minimum energy path between the initial and final states and a stable equilibrium state with respect to all other degrees of freedom except along the reaction coordinate [109,110]. A key assumption is that the measured process does in fact traverse this minimum energy path as opposed to other possible (non-equilibrium) energetic pathways [103,108,109]. For Q_{act}, the rate υ at which a reaction proceeds across the activated state is related via the Arrhenius expression:

$$\upsilon = f \exp\left(-\frac{Q_{act}}{k_B T}\right)$$

Eq. 1-19

21

Where k_B is the Boltzmann constant, T is the absolute temperature, and f is an effective attempt frequency. The exponential term describes the probabilistic likelihood of the system in question having a thermal fluctuation with energy greater than or equal to Q_{act}. For thermally activated processes in solid materials, the attempt frequency f is usually related to vibrations in the lattice that contribute to the forward reaction.

When there is no mechanical work being performed on the system, Q_{act} is represented as the Helmholtz free energy of activation $\Delta F_{act} = \Delta U_{act} - T\Delta S_{act}$, where ΔU_{act} is the activation (potential) energy and ΔS_{act} is the activation entropy [108]. When external work is applied, the Gibbs free energy of activation is used: $\Delta G_{act} = \Delta U_{act} - \Delta W_{act} - T\Delta S_{act} = \Delta H_{act} - T\Delta S_{act}$, where ΔH_{act} is the activation enthalpy [108,111]. When ΔW_{act} is zero or constant, the entropy contribution can be treated as a constant and incorporated into the attempt frequency.

$$\upsilon = f \exp\left(\frac{\Delta S_{act}}{k_B T}\right) \exp\left(-\frac{\left(\Delta U_{act} - \Delta W_{act}\right)}{k_B T}\right) = f_s \exp\left(-\frac{\Delta H_{act}}{k_B T}\right) \quad \textbf{Eq. 1-20}$$

This formulation suggests that the role of entropy is primarily in the form of contributions to thermal vibrations. The entropy, $\Delta S_{act} = -\left.\dfrac{\partial \Delta G_{act}}{\partial T}\right|_{\sigma}$, in general may be a strong function of stress (e.g. thermal expansion [103,112], changes in atomic vibration frequency due to large displacements and higher-order elasticity) and will be a maximum with $\sigma = 0$. Assuming weak temperature dependence of ΔS_{act}, which can be valid for large temperature ranges about room temperature [103,111], there is an upper

temperature bound T_M where the energy barrier disappears, i.e. $\Delta U_{act} - T_M \Delta S_{act} = 0$. For processes in a bulk crystal, such as dislocation glide, the temperature dependence is often associated with shear modulus μ; therefore, near room temperature, where μ changes very little, the apparent T_M can be at or above the bulk melting temperature [111,112].

For various processes in crystalline solids, such as diffusion or dislocation glide, the effective attempt frequency is often assumed to be on the order of – if not identical to – the atomic vibration frequency. This can be clearly illustrated in the statistical mechanics treatment of TST by Vineyard as applied to atomic self-diffusion in a crystal [109]. Evaluating υ yields:

$$\upsilon = \frac{\displaystyle\prod_{j=1}^{3N} \upsilon_j}{\displaystyle\prod_{j=1}^{3N-1} \upsilon_j{}'} \exp\left(-\frac{\Delta U_{act}}{k_B T}\right)$$

Eq. 1-21

For a crystal with N atoms, $3N$ is the total number of degrees of freedom, and υ_j and $\upsilon_j{}'$ represent the frequencies of vibration for the initial and activated states associated with each degree of freedom, respectively. Thus, in the activated state, there is one less degree of freedom as vibration along the reaction coordinate would result in decomposition to some final state. Within the harmonic approximation, one can assume that the vibrations at the saddle point are similar to those at the initial state except for one, such that f_s reduces the atomic frequency of the moving atom at its initial site [109]. As f is already assumed to be the atomic frequency, this leads to $\exp\left(\dfrac{\Delta S_{act}}{k_B T}\right) \sim 1$.

For obstacle-limited dislocation glide, the nucleation rate is determined by the measurable plastic steady-state strain $\dot{\gamma}$, where

$$\dot{\gamma} = \dot{\gamma}_0 \exp\left(-\frac{\Delta G_{act}}{k_B T}\right)$$

Eq. 1-22

Here, $\dot{\gamma}_0$ is the strain rate in the absence of local barriers, governed by the dislocation density and mobility [103,104]. For various experiments on metal systems, $\dot{\gamma}_0$ is on the order of 10^6 s^{-1} for dislocation glide overcoming discrete barriers [104]. Additionally, the stress contribution is expressed as $\Delta G_{act}(\sigma) = \Delta F_{act} - \Delta W_{act}(\sigma)$, where σ is the applied stress [103]. This leads to the concept of an athermal obstacle strength σ_{ath}, or the strength required to move a dislocation around or through an obstacle in the absence of thermal fluctuations:

$$\Delta G_{act}(\sigma, T)\big|_{T=0} = \Delta U_{act} - \sigma\Omega = \Delta U_{act}\left(1 - \left(\frac{\sigma}{\sigma_{ath}}\right)^p\right)^q$$

Eq. 1-23

In the case of work-hardened pure metals, for example, ΔG_{act} is taken to be μb^3 (on the order of 1eV) and $\sigma_{ath} = \mu b/l$, where l is inversely related to the density of forest dislocations [113]. Here, Ω is the activation volume and p and q are exponents related to the glide resistance profile and distribution of different obstacles. Ω at a fixed temperature is defined as $\Omega(\sigma) = -\dfrac{\partial \Delta G_{act}}{\partial \sigma}\bigg|_T = -k_B T \dfrac{\partial \ln(\dot{\gamma}/\dot{\gamma}_0)}{\partial \sigma}$. While not strictly a physical volume, it is directly related to the volume undergoing deformation. For many processes, the work is modeled as proportional to $\sigma b \Delta a$ (plus additional terms depending

on the process), where σ is an effective applied stress, b is the Burger's vector, and Δa is the area of the associated slipped region; hence, the activation volume is directly related to $b\Delta a$. While this provides a physical picture for the process of interest, it should be noted that the stress often performs work both on and around the slip region. For the operation of traditional Frank-Read sources, the activation volume is on the order of 100-1000b^3, which is consistent with observed rate-insensitivity of yield in bulk crystals. In contrast, activation volumes as small as $20b^3$ have been measured for nanocrystalline metals [114]. The stress dependence of $\Omega(\sigma)$ is determined by p and q, which in the simplest case, e.g. for regularly distributed, box-shaped obstacles, $p = q = 1$, whereas for randomly distributed obstacles of various shapes, the ranges found in most experiments are $0 \leq p \leq 1$ and $1 \leq q \leq 2$ [104].

To more clearly illustrate the joint temperature and stress dependences of the activation free energy, we derive here a form for ΔG_{act} that will be used extensively in our analysis in Chapter 4. For simplicity, we will assume that for the stress dependence (Eq. 1-23), $p = q = 1$. Where there is no applied stress,

$$\Delta G_{act}\big|_{\sigma=0} = \Delta F_{act} = \Delta U_{act} - T\Delta S_{act}\big|_{\sigma=0} \qquad \textbf{Eq. 1-24}$$
$$= \Delta U_{act}\left(1 - T\frac{\Delta S_{act}}{\Delta U_{act}}\right)$$

Equating this to the situation where the free energy barrier is overcome, $\Delta U_{act}(1 - T/T_M) = 0$, where T_M is the characteristic temperature at which the energy barrier is eliminated, we obtain

$$\Delta S_{act}\big|_{\sigma=0} = \frac{\Delta U_{act}}{T_M}$$

Likewise, we can obtain a maximum or athermal activation volume Ω_{ath} by considering the case when T = 0 K:

$$\Delta G_{act}\big|_{T=0} = \Delta H_{act} = \Delta U_{act} - \sigma \Omega_{ath}$$
$$= \Delta U_{act}\left(1 - \sigma\frac{\Omega_{ath}}{\Delta U_{act}}\right)$$

Equating the above expression to determine the threshold stress required for the activated state in the absence of thermal energy ΔU_{act} (1- σ/σ_{ath}) = 0 leads to:

$$\Omega_{ath} = \frac{\Delta U_{act}}{\sigma_{ath}}$$

In the most general case there will be both finite temperature and strain, and so the full form of the activation free energy must be evaluated:

$$\Delta G_{act}(\sigma,T) = \Delta U_{act} - T\Delta S_{act} - \sigma\Omega$$
$$= \Delta F_{act} - \sigma\Omega$$
$$= \Delta F_{act}\left(1 - \sigma\frac{\Omega}{\Delta F_{act}}\right)$$

This leads to a threshold stress quantity required to overcome the barrier at finite temperature (reduced by a factor of $T\Delta S_{act}$), which may or may not be temperature dependent:

$$\sigma_{max}(T) = \frac{\Delta F_{act}(T)}{\Omega(T)}$$

From this relationship, one can consider two possibilities: the first is that Ω is temperature independent and therefore equivalent to Ω_{ath}, in which case the denominator is a constant and the temperature dependence arises from that of ΔF_{act}, i.e. $\sigma_{max}(T) = \Delta F_{act}/\Omega \ (1 - T/T_M)$; the second possibility is that Ω is in fact temperature dependent and shares the same temperature dependence as ΔF_{act} (and thus of ΔG_{act}), which leads to

$$\frac{\Delta U_{act}\left(1 - {}^{T}\!/\!_{T_M}\right)}{\Omega_{ath}\left(1 - {}^{T}\!/\!_{T_M}\right)} = \sigma_{max}(T) = \sigma_{ath} \qquad \textbf{Eq. 1-30}$$

Using this relationship and Eq. 1-27, the full expression for the activation free energy in terms of the threshold temperature and stress can be determined:

$$\Delta G_{act} = \Delta U_{act} - T\Delta S_{act} - \sigma\Omega \qquad \textbf{Eq. 1-31}$$

$$= \left(\Delta U_{act} - \sigma\Omega_{ath}\right)\left(1 - \frac{T}{T_M}\right)$$

$$= \Delta U_{act}\left(1 - \frac{\sigma}{\sigma_{ath}}\right)\left(1 - \frac{T}{T_M}\right)$$

It should be noted that in Eq. 1-30, ΔF_{act} for finite stress was assumed to be the same as ΔF_{act} for $\sigma = 0$ (Eq. 1-24), which may not necessarily be true as ΔS_{act} can also be stress-dependent, i.e. $\Delta F_{act}(\sigma) = \Delta U_{act} - T\Delta S_{act}(\sigma)$. However, in taking an analogous approach to Eq. 1-28 by using $\Delta G_{act} = \Delta H_{act} - T\Delta S_{act}$ in order to solve for $T_{max}(\sigma)$, one can likewise assume that the stress dependence of ΔS_{act} is the same as that of ΔH_{act}:

$$\frac{\Delta H_{act}(\sigma)}{\Delta S_{act}(\sigma)} = \frac{\Delta U_{act}\left(1 - {}^{\sigma}\!/\!_{\sigma_{ath}}\right)}{\Delta S_{act}\big|_{\sigma=0}\left(1 - {}^{\sigma}\!/\!_{\sigma_{ath}}\right)} = T_{max}(\sigma) = T_M \qquad \textbf{Eq. 1-32}$$

Which enables the factoring out of $(1 - T/T_M)$ in the numerator Eq. 1-30. Introducing these results into the full expression for $\Delta G_{act} = \Delta H_{act} - T\Delta S_{act}$ will again have it reduce to the result presented in Eq. 1-31.

1.3.2 Size-dependent Strength in Crystalline Materials

Introducing microstructural features into the lattice in order to increase the energy required for dislocation slip is the basis for many of the strengthening treatments traditionally used on engineering metals [2,84]. The successful implementation of these methods, however, relies on mechanisms that primarily operate in bulk materials. In the mid-20th century, Brenner performed some of the first tensile tests on metal whiskers, where permanent deformation proceeded via other mechanisms entirely [17,18,115]. These whisker samples exhibited strengths much higher than bulk metals for diameters $d < 25\mu m$ [17,22]; the measured strengths exhibited significant scatter, although most of the data fit a rough relationship of $\sigma \propto \frac{1}{d}$ [17]. Similar trends were observed in other material systems such as ceramics [19,20] and semiconductors [21,116], which led to a general consensus that increased strength was due to decreased defect populations as well as a much more discrete distribution of critical strengths associated with these defects [22].

Brenner had also considered the possibility that reduced dimensions could inherently strengthen these weak points in a material that deforms by dislocation mechanisms [22]. The large strains observable in annealed bulk metals necessitated the generation of further dislocations to sustain ductility after the pre-existing ones glide

28

through. This can occur via the activation of pinned dislocation segments known as Frank-Read sources, where the strength required to bow out new dislocations from the original source scale inversely with the distance between the pinning points [84,117]. Thus if the critical dimensions of a specimen are comparable to the typical length between pinning obstacles in Frank-Read sources (on the order of microns [22]) this can give rise to source truncation, where the external dimensions of the specimen control the critical strength for plastic yield [118–123]. This model, along with the proposal of source exhaustion [118,121,124–126], where dislocations are mechanically annealed out of the volume during deformation, are the two main mechanisms that have been proposed for the size-dependent strengthening observed in more recent pillar tests.

The large volume of results for pillar and nanowire deformation have supported what appears to be a universal relationship between strength and size among samples with initial dislocation densities [127]. Dou and Derby proposed that this relationship takes on the form of

$$\frac{\tau_{RSS}}{\mu} = A \left(\frac{d}{b} \right)^{-m} \qquad\qquad \textbf{Eq. 1-33}$$

Where A and m are empirical constants [128]. For pillar compression [121,122,129–131] and tension [118,132] tests as well as a number of studies on nanowire plasticity [133,134], there is general agreement with the proposed constant of $m \sim 0.6$ for FCC crystals (Figure 1-9). This power law has also been applied to evaluate size-dependent strength in BCC and HCP micro- and nanostructures, yielding different (often lower) m [127,128], which has been supported by atomistic simulations clearly indicating the very

different dislocation mechanisms inherent in these crystal structures [135]. However, what remains still unclear is the mechanism that dictates the value of the power law exponent.
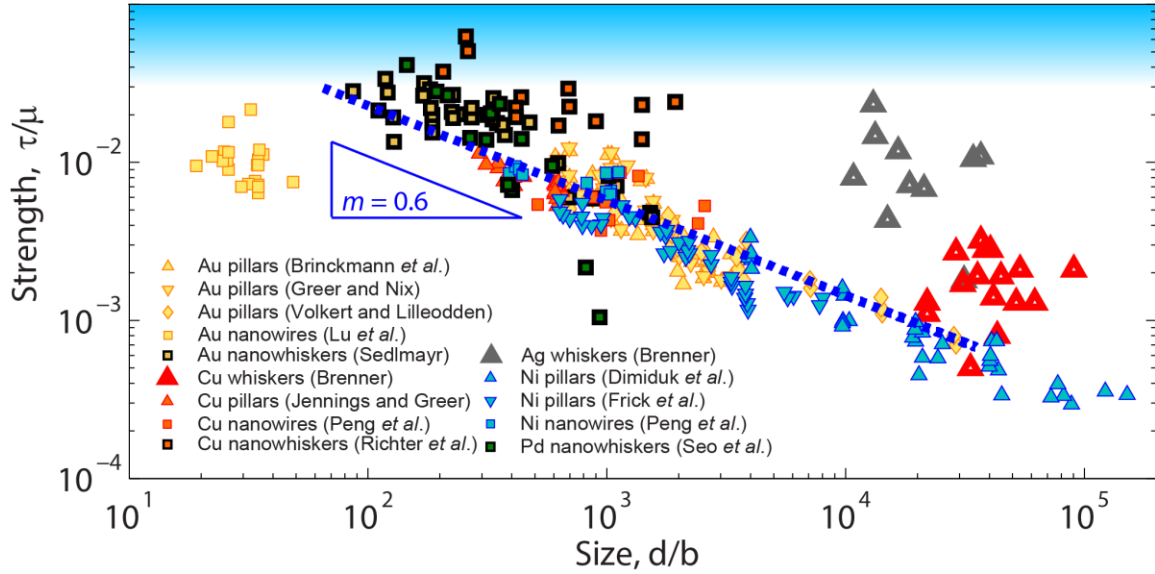
Figure 1-9 Experimental measurements of the strength of FCC single crystal micro- and nanostructures under uniaxial deformation. The dotted slope represents the power-law relationship between size and strength that has been seen in many of these studies. The gradient along the top of the plot indicates the range of τ_{th}. Nanowhisker specimens similar to the ones in this work are indicated by markers with thick black borders. Size is normalized with respect to the full burgers vector, whereas strength is calculated with respect to either the full or partial burgers vector for specimens with or without pre-existing dislocations, respectively. Data was obtained from Refs. [18,39,67,121,124,129,131–134,136–139].

One major counterexample to the "universal" law is from Bei *et al.*, who, by controlling the defect density in Mo-alloy fibers, were able to demonstrate the tunability of strength and plastic deformation in these structures [140]. Defects via pre-straining were introduced into the fibers by compressing the NiAl matrix in which they were

solidified. At the extremes of no pre-strain and 11% pre-strain, strength was generally found to be size-independent, with 0% pre-strain samples exhibiting high strengths similar to dislocation-free structures and 11% pre-strain samples behaving like bulk Mo. Only at intermediate pre-strains values was there observable size dependence accompanied by significant scatter. This illustrates that by simply changing the original configuration and concentration of defects, it is possible to achieve a variety of deformation responses.

This importance on initial dislocation density is further alluded to by some of the data sets in Figure 1-9, which consist of specimens mostly free of pre-existing dislocations. These include whiskers grown via halide reduction [18], defect-free nanowhiskers produced by physical vapor deposition [39,139,141], and cold-welded nanowires [136]. Some of these specimens do not fall on the trend line at all, such as the silver whiskers and gold nanowires, whereas the nanowhisker specimens may show similar or greater size dependence. As these specimens are generally free of pre-existing carriers of plasticity, they rely on processes such as surface dislocation nucleation to plastically deform and hence would not necessarily exhibit the same size dependences as non-defect-free specimens. On the other hand, predictions and calculations have suggested that the strength in defect-free systems should be weakly size-dependent [110,140] except in the presence of non-negligible surface stress at very small diameters [25,142], and this does not appear to be the case for the tested nanowhiskers.

Computational studies into dislocation nucleation have shown that these structures demonstrate very pronounced tension-compression asymmetry not observed in

31

pillar specimens. This is due to combined effects of surface stress-induced relaxations, asymmetries in the Schmid factors of the first nucleating partials, and asymmetry in the associated generalized stacking fault energy curves [24–26,28]. Additionally, size dependence of strength is predicted to arise not only from the number of dislocation sites, which would scale with surface area [28,143] or axial length [110], but also the applied strain rate and temperature due to the local, thermally activated nature of the nucleation process [28,110,111,144].

1.4 Dislocation Nucleation-mediated Plasticity

Despite a rich understanding of the structure of dislocations pre-existing within crystals, their interactions with other defects, and even their annihilation, it is striking that the introduction – or nucleation – of dislocations in pristine crystals is so poorly understood. Nonetheless, there is a need to characterize this process, which can degrade both mechanical and functional performance in otherwise pristine crystals. In bulk metal crystals, large populations of dislocations exist (between $\sim 10^{10}$ and 10^{15} m^{-2}) following synthesis or treatment, yet descriptions of their origin remain largely phenomenological. In semiconductor synthesis, extreme measures are taken to limit dislocation densities (down to $\sim 10^{5}$ m^{-2}), although the presence of these defects is nevertheless ubiquitous, given the extreme conditions during crystal growth and relatively low energy barriers for nucleation. Recently it has been possible to synthesize nanostructures with few or even zero defects owing to the miniscule volumes of material and near-equilibrium crystal growth [39,145]. These materials, thus, operate in a regime where conventional

32

dislocation processes are abated and must rely on nucleation to relieve large stresses and facilitate plastic deformation if brittle fracture is to be mitigated. Since a large fraction of atoms in nanostructures resides at surfaces and interfaces, these materials are particularly prone to heterogeneous dislocation nucleation at ultrahigh stresses near the theoretical upper limit [37]. In these extreme settings, deformation mechanisms can be dramatically different from their bulk counterparts. For instance, plastic deformation in otherwise brittle semiconductor materials such as Si is no longer dominated by crack propagation but instead by dislocation generation and glide, in some cases resulting in superplastic-like behavior [146–148].

Despite a relative scarcity of experiments able to directly observe or measure dislocation nucleation [39,149–154], several recent studies have employed atomistic simulations to not only demonstrate the nucleation mechanism under various loading conditions but also, in combination with transition state theory, reveal the pronounced thermally activated nature of this process [110,155–158]. These simulations and experiments all unequivocally show that ultrahigh stresses near the theoretical strength are required for the nucleation process, with a value that is generally much less sensitive to specimen size in the absence of pre-existing dislocations and sources compared with micrometer-sized crystals [127,151,159,160]. Furthermore, nucleation is assisted by thermal activation with very small activation volumes of the order of the atomic volume (corresponding to the nucleation of the first partial dislocation), in stark contrast to bulk crystals (e.g. face-centered cubic (FCC)) where it ranges from 100-1000b^3. These predictions have been corroborated by systematic temperature-dependent nanoindentation

studies using excursions of the load-displacement response during surface loading of FCC crystals as the signature of dislocation nucleation, albeit in a complex state of loading with large stress gradients and a presumed location for nucleation [149,161].

A striking implication from the small activation volumes is an intrinsic thermal uncertainty [37,149,162] that in experiments or device operation would manifest as a pronounced stochasticity of nucleation strengths, thereby necessitating a statistical approach to any study and demanding a non-deterministic approach to device design. Whereas a broad distribution of nucleation strengths would be expected at finite temperature, the strength and associated scatter are predicted to be temperature-dependent, with a singular deterministic strength emerging in the athermal limit (0 K). No experimental study, to our knowledge, exists that fully characterizes the temperature-, size-, and strain-rate-dependent nucleation process, with quantifiable mechanistic, energetic, and kinetic deliverables, in defect-scarce materials subjected to spatially uniform stress states. Such a study would serve to bolster the scientific knowledge base on dislocations in crystals in their most embryonic state – at the point of nucleation.

1.5 Material Background

The material system we have chosen to look at in this study is Pd. In addition to being able to grow high-aspect ratio nanowhisker samples suitable for tensile testing with zero or near-zero defect density, bulk Pd possesses a higher melting temperature than other metals and is highly resistant to oxidation. These characteristics lend confidence in

the thermal and chemical stability of these structures for non-ambient temperature testing. Moreover, palladium exhibits many other electronic and chemical properties that are important for many applications, and hence its structural integrity is of technological importance. The surface of Pd serves as an outstanding catalyst for various chemical reactions [163–167]. Most notably, Pd is extremely active in the presence of hydrogen, which readily adsorbs onto its surface and absorbs into its lattice up to very high concentrations [168–170]. In spite of Pd being both expensive and heavy relative to other hydrogen storage materials [171], research remains active in applying Pd for other related technologies such as hydrogen filtration and sensing [170,172].

Nanoscale Pd structures are promising for a number of advantages over bulk Pd. By virtue of their small volume, Pd nanostructures are prime candidates in hydrogen sensing applications: hydrogen is able to diffuse rapidly throughout the entire volume, and measurable resistance changes or volume expansions can be readily observed at low concentrations [16,173–175]. The absorption of hydrogen near room temperature results in "naklep" or phase transformation strain hardening as Pd goes from a low H-concentration α-phase to a β-phase hydride: the Pd matrix undergoes 11% volume expansion and extensive dislocation generation while traversing the α-β miscibility gap (Figure 1-10), leading to matrix embrittlement [168,176–178]. The mechanical work required for this process leads to the pressure hysteresis often seen during hydrogen cycling, where the pressure plateau over the miscibility gap is much greater when loading from α to β than during unloading. The generation of dislocations, however, is suppressed if the phase transformation can maintain coherence with the matrix. This has been

35

observed for phase nucleation in thin foils, where small spherical or disc-like particles with nanometer dimensions appear near the surfaces of the foil to reduce their overall strain energy [179,180]. These observations suggest that for sufficiently small volumes and close surfaces it may be possible to avoid dislocation generation and thereby maintain the structural integrity of Pd structures over repeated cycles.
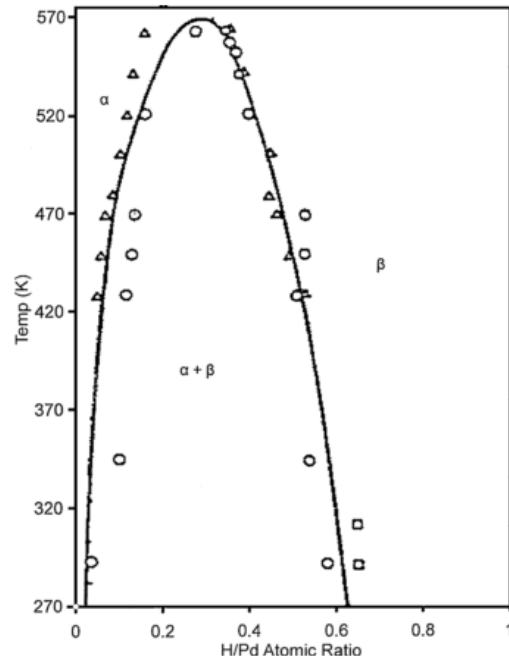
Figure 1-10 Palladium-hydrogen phase diagram, from Ref. [178] **(**Copyright 2009, with Permission from Elsevier).

Research into interactions between Pd and hydrogen at the nanoscale have revealed interesting results with implications for the mechanical behavior. In a study by Jeon *et al.*, Pd nanowires were shown to have increased sensitivity (change in resistance) to hydrogen at smaller diameters, due to higher occupancy of hydrogen atoms at surface and subsurface sites than in bulk Pd [181]. In addition, studies on the absorption

hydrogen in Pd structures with dimensions less than 100 nm show reduced pressure hysteresis, increased plateau pressure, lower critical temperatures for the miscibility gap and changes in solubility limits for α and β phases [165,182,183]. Moreover, pre-existing elastic strains within the lattice as well as changes in the electron density of states for structures with dimensions below 10nm have also been considered as methods to modify the interaction between Pd and hydrogen [6,184]. Given the demonstrated importance of mechanical deformation in the interactions between Pd and hydrogen, we expect that our results on defect-free Pd nanowhiskers will provide extremely valuable knowledge to many current areas of active research.

1.6 Overview

We have shown that both elastic and plastic deformation in nanoscale single crystals can fundamentally differ from those observed in bulk materials, although there remains a great deal to be understood regarding the responsible mechanisms. Much of the current knowledge has been informed by theoretical and computational studies [26,27,110]: while they may not always accurately reflect experimental conditions, they have nonetheless provided valuable insight that has been challenging to obtain in experiment. Additionally, many theoretical and computational studies have shown deviations in mechanical properties for both regimes may have common origins, such as surface stress [24,28,185], but very rarely do experimental studies quantitatively address both elastic and plastic response together [67,186,187].

37

The major points of this thesis are as follows: first, we quantify both the elastic and plastic response in defect-free and –scarce Pd NWs; second, we propose the mechanisms responsible for these responses, including common mechanisms that govern both elastic and plastic response; and finally we address agreements and discrepancies with existing theoretical studies. Chapter 2 will begin with the experimental setup, which consists of the characterization of the Pd NW samples and the tensile testing setups used to evaluate the mechanical behavior. Additionally, extensive detail regarding the development, characterization, and operation of an integrated temperature control system essential to our study of incipient plasticity will be provided here. We cover in Chapter 3 our investigations into the elastic response up to very high strains, which have provided crucial information regarding nanoscale elasticity that has not been accessible in previous studies. Chapter 4 details the experimental characterization of the thermally activated incipient plasticity in Pd NWs over a range of strain rates and temperatures. We used the mean strength and scatter to calculate thermal activation barriers and compare with results from existing analytical and computation models of dislocation nucleation, in particular addressing the important roles of stress dependence and attempt frequency. In Chapter 5 we investigate further the assumptions of thermal activation theory in its application to dislocation nucleation as well as address how some of the features of real materials (e.g. surface flaws) could potentially impact experimental results. Finally, in Chapter 6 we summarize the major findings from this thesis and outline future experimental directions.

2 Materials and Experimental Methods

One of the greatest challenges in accurate measurements of mechanical properties in nanoscale materials has been development of a versatile tensile testing setup. Consequently, a large portion of the work accomplished in this thesis lies in the evaluation and design of experimental tools and procedures, particularly those related to coupling mechanical testing with non-ambient temperature control. The essential steps for completing a successful experiment will be covered, including fabrication and characterization of defect-free or defect-scarce nanowires, preparation of individual samples, features and operation of the testing stage, and determination of the relevant stress and strain information. Several of the following sections will also detail the adaptation of this testing setup to performing controlled temperature experiments both above and below room temperature. Finally, an *in situ* tensile testing stage for transmission electron microscopy (TEM) experiments, which has provided direct observation of deformation mechanisms, will be described.

2.1 Growth and characterization of Pd NWs

Single-crystalline Pd NWs were grown by physical vapor depostion onto ceramic substrates under ultrahigh vacuum conditions at elevated temperature. Bare (001)-$SrTiO_3$ or (0001)-Al_2O_3 substrates were inserted into an ultra-high vacuum molecular beam epitaxy system with pressures at ~10^{-10} mbar or lower. A Pd source was heated up to

1200˚C and deposited at a rate on the order of 0.01 nm s^{-1} onto the substrates, which were maintained at 950˚C during the deposition process. Pd NWs often formed at the edge of the substrates in near-perpendicular directions ideal for nanomanipulation (Figure 2-1(a)). On SrTiO$_3$ substrates they also grow from roots on the substrate face but in a direction that is mostly parallel to the face and are also well aligned for manipulation purposes. Some variation in size is observed in the NWs grown on either substrate: those grown on SrTiO$_3$ often have lengths of at least 5μm to 15 μm and diameters between 30-250 nm. Diameters for samples grown on Al$_2$O$_3$ often have smaller diameters of less than 100 nm and shorter lengths (< 10 μm), although the substrate is prone to charging, which makes the samples very challenging to image and therefore harvest for testing.
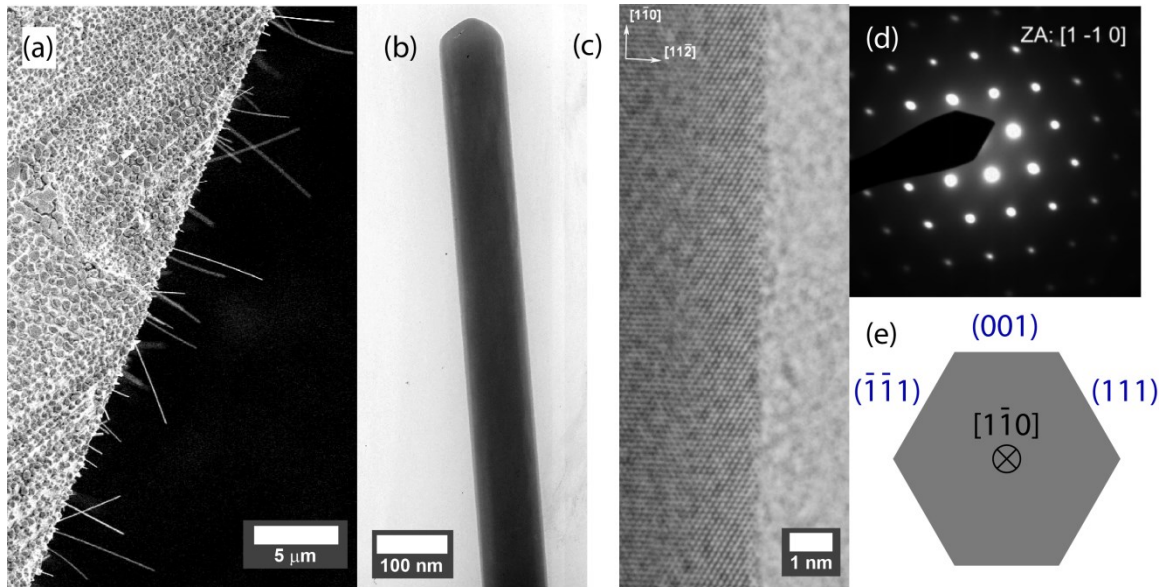
Figure 2-1 Characterization of Pd NWs. (a) SEM micrograph of Pd NWs grown on the Al$_2$O$_3$ substrate. (b) Bright-field TEM micrograph of Pd NW. (c) High-resolution TEM micrograph of the surface morphology of a Pd NW along an edge between two facets. (d) Selected-area electron diffraction (SAED) pattern for a pristine Pd NW. (e) Schematic of ideal Wulff cross-section. *Bright field and high-resolution TEM images courtesy of Dr. Gunther Richter.*

40

The bottom-up growth at near-equilibrium conditions resulted in distinct surface facets, and the NWs showed no evidence of taper or visible roughness on the surfaces (Figure 2-1(b)-(c)). The orientation was confirmed by electron diffraction analysis on at least ten NWs with diameters $30 < d < 150$ nm from each substrate prior to testing (Figure 2-1(d)). Based on the $[1\bar{1}0]$ orientation, the expected cross-section geometry from the Wulff construction is presented schematically in Figure 2-1. This resembles the shape observed for most of the nanowire from investigating over 20 samples (~80%), most of them from the Al_2O_3 substrate, although occasional higher-aspect-ratio elliptical and ribbon geometries were observed (Figure 2-2). Usually the latter are easy to spot during the manipulation period and generally avoided for testing due to the difficulty of determining directly their cross-section area.

It is unclear if the change in shape actually changes the faceting, e.g. the planes forming the elliptical cross section are different from those of the of the round or ribbon shapes. If the planes are the same type, then to a first approximation the shape should not does not change the nucleation strength trends: the number of sites will still be the same, and the critical dislocation configuration has been predicted to have a loop radius of several b [28,188,189], which is small compared to the size of most of the wires ($> 100\ b$).
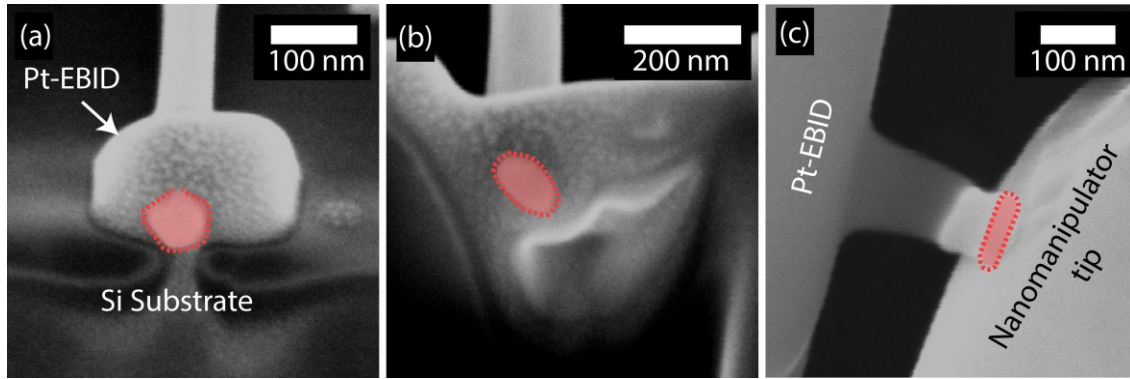
Figure 2-2 Cross-section shape variations for Pd NWs. (a) SEM image of 52˚-tilted focused-ion-beam (FIB)-milled cross section of a NW fragment. (b) Elliptical cross-section, also FIB-milled. (c) Top-down view of ribbon cross-section. Nanowire is being pushed upright by the nanomanipulator tip.

High resolution scanning transmission electron microscopy (TEM) verified the absence of a native oxide layer on the NWs. Since both high temperature (>1000 K) and oxygen partial pressure are required to form oxide layers on Pd [190], these NWs were expected to remain oxide-free during testing at elevated temperatures. For Pd NWs grown on the $SrTiO_3$ substrate (35% of entire data set), TEM imaging showed no visible pre-existing defects such as dislocations or vacancy clusters (Figure 2-1(b)). For the remaining NWs grown on Al_2O_3, about half of the specimens exhibited evidence of an axial grain boundary (~30% of entire data set) along the axis while the remainder were defect-free. The type of boundary and effects on the NW structure is still being determined. Since the boundary is along the NW axis, its resolved shear stress is zero. Postmortem imaging in the TEM confirms that the boundary remains in the NW even after fracture (see Section 5.2), and the nucleation strength distributions from data sets

containing defect-free NWs and those containing stacking faults were not statistically distinct (see Section 7.3 full analysis).

2.2   Tensile Testing of Nanowires

The tensile testing stage is one of several modules built onto the CINT "lab-on-a-chip" discovery platform (Figure 2-3). There are a number of major advantages to using this setup: the chip is operable in both air and in vacuum, so it can be readily adapted to testing in different environments; all the moving components are on a single platform and designed to move in-plane, eliminating many problems with instrumental alignment in other setups [41,191]; and given its small size and low thermal mass, it can be uniformly heated or cooled for non-ambient temperature testing. An overview of the stage's major components is shown in Figure 2-3(a). The testing stage consists of a compound-flexure load cell and a thermal actuator fabricated from polycrystalline silicon. A SiN_x strip fabricated on the actuator-side grip mitigates heat flow to the specimen during testing. The sample of interest, in this case a Pd NW, is mounted across the gap between the load cell and actuator grips (Figure 2-3(b)). The two sets of chevron beams along the length of the actuator shaft are oriented such that upon resistive heating, the beams expand and push the actuator away from the load cell. The rate of thermal expansion and thereby the displacement is controlled by the current (or voltage) set across the beams. Due to the low thermal mass of the beams, the maximum temperature is quickly attained and stabilized, i.e. instantaneous actuation with negligible drift.

43
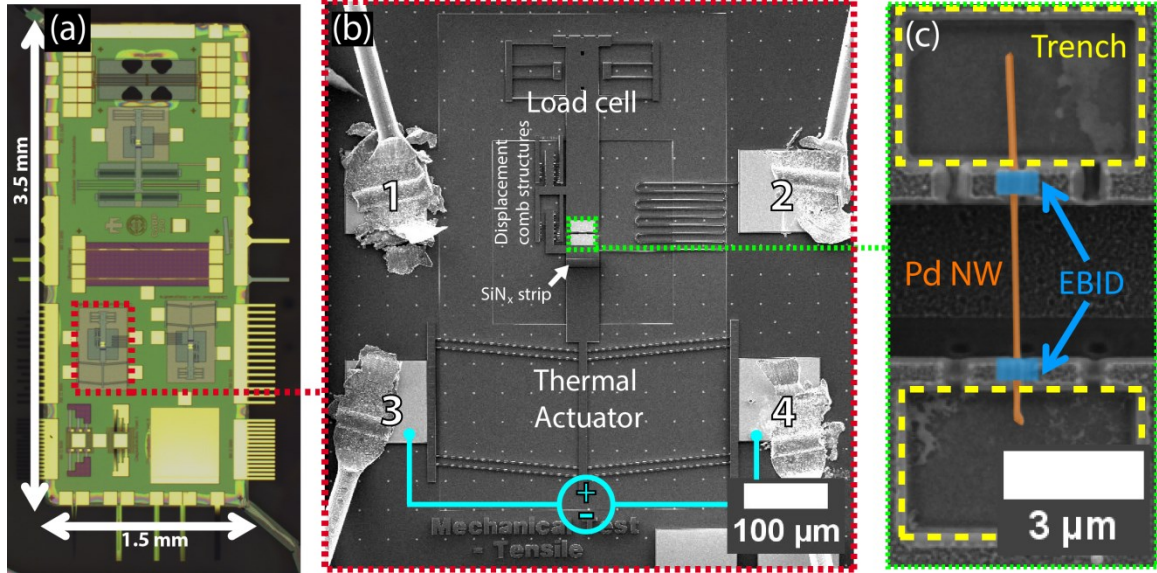
Figure 2-3 MEMS-based testing stage. (a) Optical micrograph of CINT discovery platform with tensile testing stage marked in the red box. (b) SEM micrograph of the MEMS-based tensile testing stage. Wire bonds 1 and 2 are used for grounding the stage during SEM imaging. Wire bonds 3 and 4 are the electrical connections for actuating the chip. Green dotted square indicates area where samples are mounted. (c) SEM micrograph of an individually manipulated NW mounted to the grips.

Strain is determined from the change in the distance between the load cell and actuator during each test. The displacement of the load cell from its initial position is used to determine the stress. The stiffness of the load cell beams has been previously determined through resonance frequency measurements. Separate finite element simulations have been performed to confirm both the compliance value as well as linear elasticity of the load cell structure for the displacement ranges obtained during actual testing. The compound beam geometry is designed to eliminate both in-plane parasitic displacements and out-of-plane rotations.

Since in-plane drift of the entire MEMS device is often unavoidable, anchored points on the chip substrate are also tracked. The displacement of anchored points

44

relative to the frame of the acquired image is then subtracted from the raw load cell and actuator displacements.
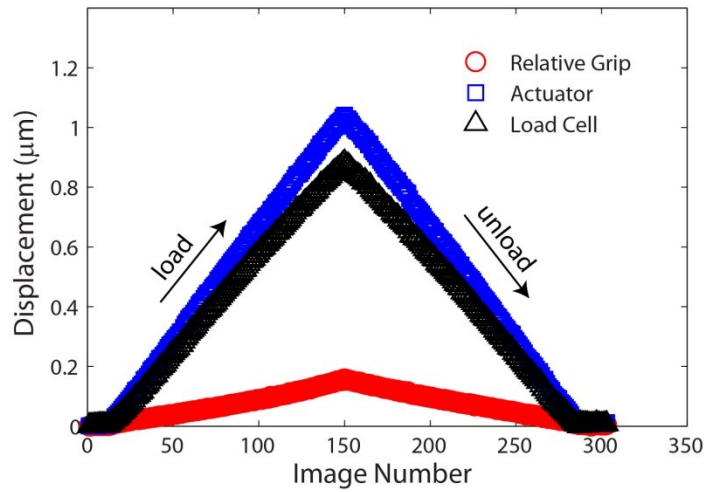
Figure 2-4 Measured displacements of the load cell and actuator during a load-unload test. The relative grip quantity is the change in displacement between the load cell and actuator relative to the original displacement and is used to calculate strain.

2.2.1 Calibration of the Thermal Actuator

The amount of Joule heating in the thermal actuator chevron beams during operation of the MEMS testing device, and therefore the displacement of the actuator, is directly related to the electrical power input (P) as a function of applied current (I) and voltage (V). Since beam degradation over time could lead to an increase in resistance, voltage is sourced instead of current ($P = IR = V/R^2$) to avoid catastrophic run-out of the actuator.

Actuator calibration was performed by capturing images of the testing stage at several voltage values and measuring the displacement. This information was used to

45

linearize the voltage displacement function for different testing conditions, enabling constant displacement rates. Figure 2-5 shows that stage operation in air requires higher voltages to reach displacements comparable to those achieved in vacuum due to conductive heat loss through air. In vacuum, calibration has been performed in the cryostat at various setpoint temperatures, the extremes of which are shown in Figure 2-5. Several properties of Si and their temperature dependencies can affect the resulting actuator displacement induced by Joule heating. A figure of merit directly related to the Joule heating induced displacement ($\delta \propto \alpha C_p / \rho$) can be derived by accounting for the temperature dependence of the linear coefficient of thermal expansion α, the specific heat capacity C_p, and beam resistivity ρ [192–195]. Plotting the figure of merit alongside the measured resistivity at low voltage (inset of Figure 2-5) shows that the changes in material properties dominate the temperature-dependent actuator response. Whereas ρ alone increases with temperature and thus would reduce the power supplied to the beams ($P \propto V^2 / \rho$), the ultimate beam displacement δ response is predominately governed by the temperature dependences of α and C_p ($\delta \propto \alpha C_p / \rho$). Indeed, the actuator calibration at the highest testing temperature yielded the largest displacements for the given voltage range. We note that the crossover at high voltages between the room temperature (295K) and low temperature (144K) calibration curves shown in Figure 2-5 can be attributed to changes in the heating profiles of the thermal actuation beams during Joule heating at cryogenic temperatures, which is not accounted for in the simple figure of merit.
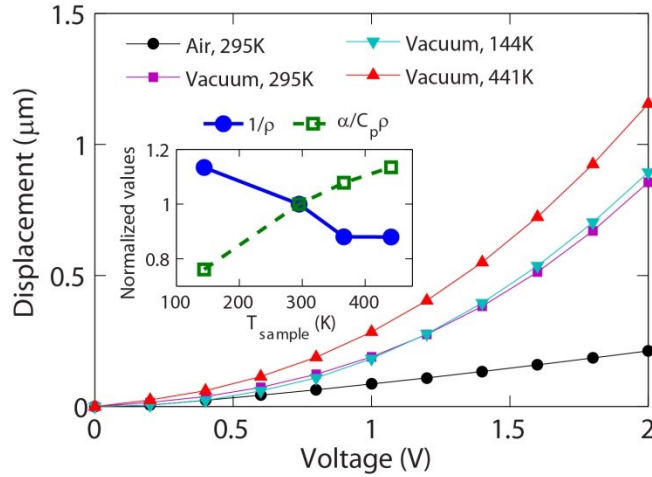
Figure 2-5 Calibration curves for the displacement of the thermal actuator along the tensile axis. In vacuum, the absence of convective heating losses results in larger displacements for the same voltages compared to operation in air. The inset shows that while the resistivity of the beams increases with temperature, the thermophysical properties of the actuator materials manifest in greater lengthening of the chevron beams, and hence larger displacements, at elevated temperatures.

2.2.2 NW Harvesting

Individual NWs were harvested using a nanomanipulator directly from the growth substrate and attached onto the Si grips of a MEMS-based tensile testing stage using Pt-containing electron beam induced (hydrocarbon) deposits (EBID) (Figure 2-3(b)). Selected-area rastering of the electron beam during EBID deposition allowed for control over the geometry and size of the EBID bonds used to harvest and then mount a NW. Since most of the wires are smaller in diameter than the radius of the probe tip used for manipulation (> 100 nm), trenches were etched into the Si grips near the edges during preparation using a focused-ion beam (FIB) to ensure that the mounted NW is flush with the grip surface (Figure 2-3(b)).

For preparing samples to be tested at low temperatures, it was expected that thermal contractions would pull the NW in tension during cooling, leading to a nonzero initial load on the specimen (e.g. as high as 3 GPa for diameters as small as 40 nm, provided a temperature difference $\Delta T = $ -150 K). To compensate for this phenomenon, an approach was developed wherein the specimen is intentionally "pre-buckled" prior to cooling. This was achieved by supplying a fixed voltage to the actuator to increase the grip separation prior to and during mounting (Figure 2-6(a)). Owing to the high aspect ratio of the nanowires, the expected critical buckling stress is less than 100 MPa, at least an order of magnitude smaller than the typical yield strength [196]. After securing the wire with EBID contacts, the voltage was ramped back down to zero, and the NW could be pulled taut during testing or during cooling. We note that this procedure is only necessary for low temperature testing, as this pre-buckling effect naturally occurs during temperature ramping in preparation for high-temperature tensile testing.
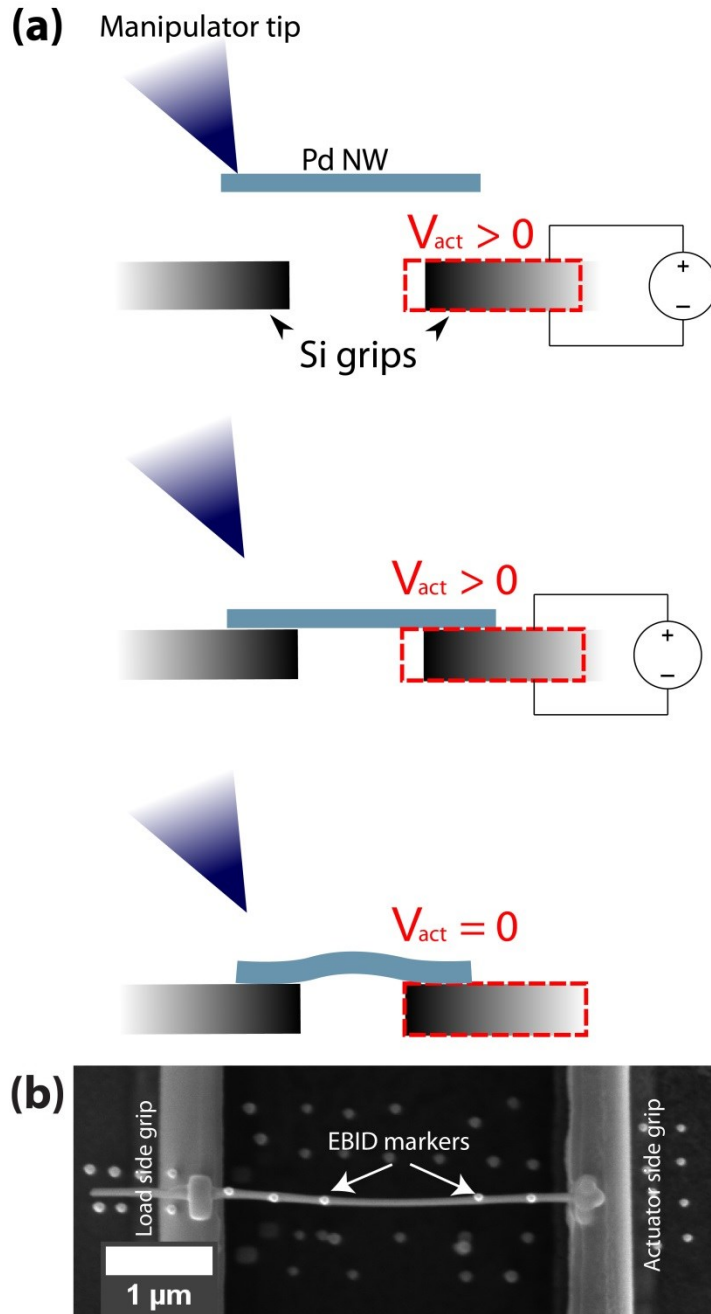
Figure 2-6 Preparing specimens for cryogenic mechanical testing. (a) Schematic illustration of procedure for pre-buckling a nanowire specimen in preparation for a low temperature test. The dotted red outline indicates the initial position of the actuator-side grip when no voltage is applied. (b) SEM micrograph of buckled Pd NW with contrast markers for *in situ* testing.

2.2.3 Digital Image Correlation and Strain Measurements

During a tensile test, images are taken at regular intervals and then processed using digital image correlation (DIC) to track the displacement of these features [40,197,198]. A base image is divided into sub-images around high-contrast, and the positions of these sub-images are updated for each subsequent capture based on maximization of a correlation function providing the best mapping between reference and deformed states. As the tracked structures move in a rigid body fashion, the correlation function is adequately determined via translations of the sub-images. Since the updated sub-image positions may be a fraction of a pixel, this enables extremely high resolution: even using optical imaging in the current setup, we achieved sub-pixel displacement noise floors with typical values of approximately 0.05 pixels.

A sample image for a tensile test in the SEM would resemble Figure 2-6(b). In this case, we track the EBID fiducial markers (white and gray spots in Figure 2-6(b)) deposited using spot mode in the SEM to obtain the displacements of the load cell and actuator. Tests performed in the SEM in fact have two options for strain measurement, either from the difference in displacement between the load cell and actuator grips, which yields a 2-point averaged strain, or directly from the sample with the aid of EBID fiducial markers along the length (Figure 2-7). The higher magnification possible in the SEM allows for direct measurement of strain along the wire axis by tracking the displacement of fiducial markers deposited via EBID on the wire itself. Under the optical microscope, since the NW samples cannot be directly imaged, comb structures directly attached to the load cell and actuator are tracked (Figure 2-3(a)).
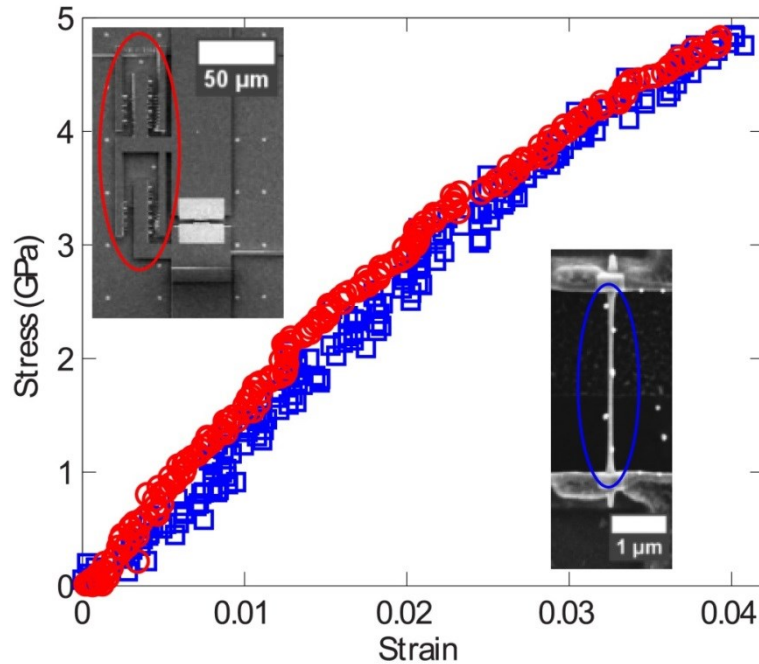
Figure 2-7 Stress-strain curves obtained for a single test to yield using two methods of strain measurement. Red indicates strain obtained from measuring the grip displacement, which can also be tracked by the comb displacements at lower magnifications (e.g. under the optical microscope). Blue indicates strain obtained from fiducial markers deposited via EBID along the length of the test specimen.

Since the grip strain includes both the strain from the sample as well as from the EBID contacts, it is important to ensure that the contacts are sufficiently stiff and produce consistent results with the direct strain measurements [199–202], especially for the temperature-controlled tests that are currently performed exclusively under the optical microscope. Some variability exists between the grip strain and direct strain measurements but for many samples the agreement in the elastic regime is within 10% error, such as in Figure 2-7. For samples that were tested to fracture under the optical microscope, discrepancies in the strain measurement can be corrected by performing load-unload tests under the optical microscope identical to those in the SEM. For

evaluation of the elastic behavior, the importance of accurate strain measurement is obvious; however, the compliance does not influence the load – and therefore strength – measurements that are the focus of the study of dislocation nucleation-mediated plastic deformation [203].

2.3 Non-ambient Temperature Testing

The MEMS-based stage was set in a ceramic electronics package that enabled easy transport between scanning electron microscope (SEM) and optical setups. Wire bonds between the electrical contact pads of the stage to the package enabled connection to an external power supply for operating the actuator. Due to the low thermal mass of the package and stage, a non-ambient temperature testing setup employing a Janis ST-500 microscopy cryostat was used to uniformly heat or cool the stage.
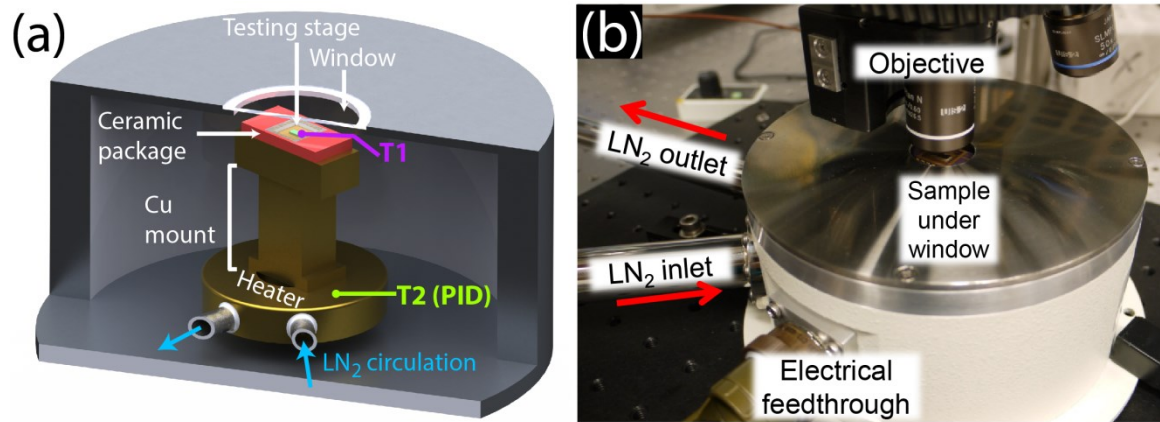
Figure 2-8 (a) Temperature testing configuration in the cryostat with MEMS stage mounted in a ceramic package. A thermocouple mounted on the MEMS chip (T1) provides the sample temperature, and a Si diode sensor at the heat exchange base (T2) provides the reading to a PID temperature controller. (b) Photo of the vacuum cryostat setup under the optical microscope.

The cryostat consists of a sealed vacuum chamber with a fused silica window in the top flange for imaging the stage (Fig. 1a). The cryostat was continuously pumped using a HiCube 80 Eco turbo pumping station (Pfeiffer Vacuum) down to pressures as low as 10^{-6} mbar. Liquid nitrogen (LN_2) entered from the inlet leg via a transfer hose, ran a path directly connected to the mount and heater, and exited through the outlet leg. Each leg is a pair of coaxial pipes, where the outer pipe is isolated from the inner pipe by vacuum to promote the continuous flow of nitrogen in liquid form until it reaches the exhaust in its gaseous state as well as to minimize condensation.

The chamber interior consists of a Cu mount directly coupling the sample to the cryogen path and a thermoresistive coil heater at the bottom (Fig. 1b). The mount includes clamps with copper wires to mechanically secure and electrically connect the ceramic package. Thermal pastes rated for cryogenic and high temperatures were used to further promote conduction between the mount and the sample. The wiring on the mount clamps is connected to electrical feedthroughs that enable the operation of the actuator by an externally connected power supply. Temperature sensor feedthroughs enable measurements of temperature at different points within the cryostat. Three temperature sensors were used inside the chamber: a thermocouple adhered with silver paint to the top of the testing stage substrate; a thermocouple on the mount midway between the cryogen path and sample; and a Si diode sensor at the foot of the mount on the resistive heater that provides feedback to a PID temperature controller. The different temperature

measurements are referred to here as the sample temperature (T_S), mount temperature (T_M), and heater temperature (T_H).

The heater temperature was determined by the cryogen flow and the temperature control parameters, with control feedback enabled at this location by the PID loop. The sample temperature, however, was governed by additional factors and may be significantly different from the setpoint. With the chamber constantly being pumped at high vacuum, convection from the chamber walls is negligible. Due to the close proximity of the top of the ceramic package to the top flange and window (<0.5mm), radiation can, in contrast, be significant and lead to excessive heating of the sample during cooling. Even with thermal paste applied to the bottom of the ceramic package, the sample temperature can be over 100K away from the setpoint owing to radiation as discussed below. This large difference between the sample and heater underscores the importance of measuring temperature at multiple points, especially at or near the sample. The system used here is capable of achieving a nominal temperature range at the heater of 77-475K. We note that this temperature range was selected to avoid high temperature regimes where nanoscale instabilities have been reported to appear [204,205].

2.3.1 Achieving and Controlling Sample Temperature

At a pressure of 10^{-6} mbar, continuous cryogen (LN_2) flow enabled the heater block to achieve steady state at 77 K within 500s of opening the dewar valve. For elevated temperature tests, both thermoresistive coil heating and active cooling were necessary for temperature control. In addition to the PID temperature controller, the flow

of LN$_2$, or an alternative cooling fluid such as N$_2$ gas, provided a stable cold reference temperature. As shown in the top panel in Figure 2-9(a), the flow rate control of the coolant affected the temperature stability, which can be attained upon adjusting the flow properly. Once steady state was attained, noise in the temperature reading at the sample (calculated as the standard deviation of a 1000-second time interval) reached a maximum of 0.08K at a setpoint of 475 K and a value of 0.035K at 77 K.
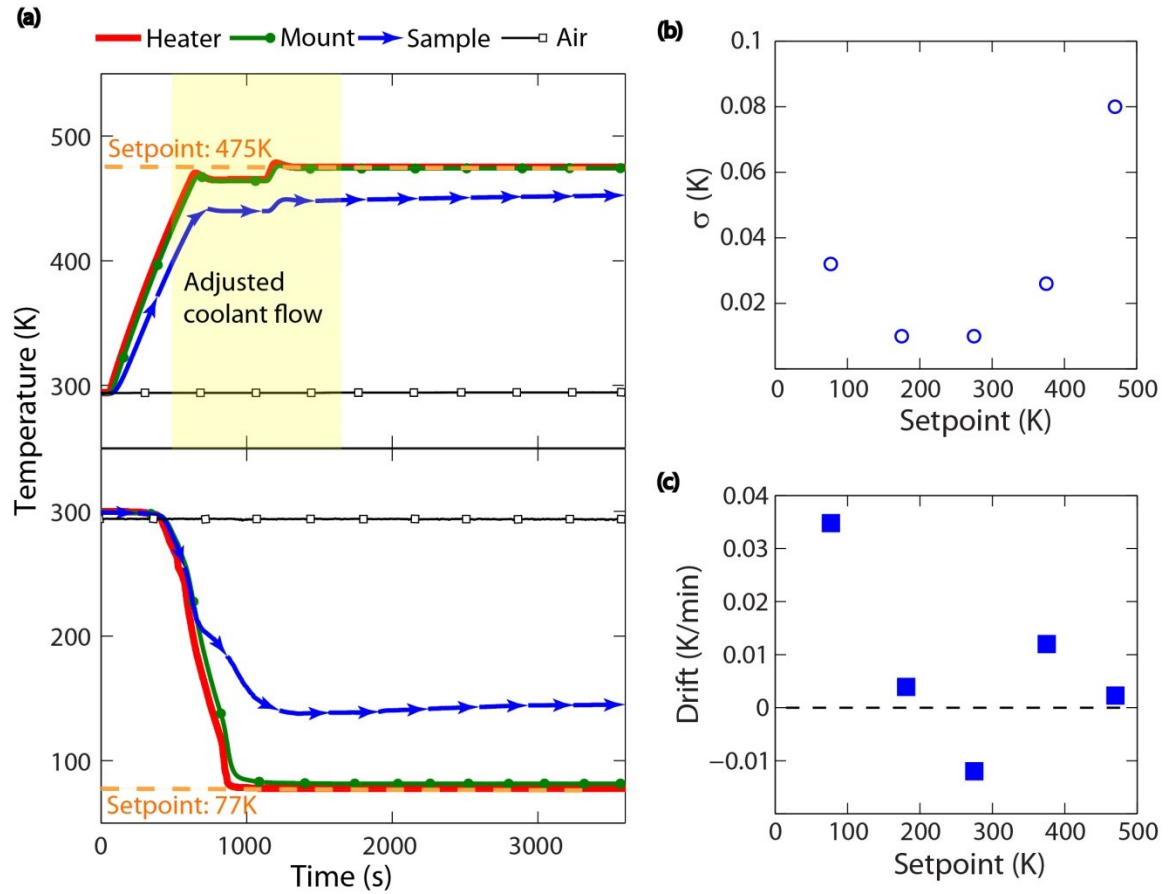
Figure 2-9 Achieving temperature control and stability during cooling. (a) Time dependence of temperature of the thermoresistive heater, copper mount, sample, and laboratory air when heating to a setpoint value of 475 K (top) and during liquid nitrogen cooling (77 K) (bottom). (b) Temperature noise at the sample, measured as the standard deviation σ of a 1000-second time interval after a steady-state temperature is reached. (c) Temperature drift at the sample during the 1000-second interval.

Temperature drift at different setpoints has also been characterized to estimate the overall change in temperature during testing. The drift ranges from a maximum value at 77 K of 0.035 K/min to a minimum at 475 K of 0.002 K/min. For a typical nanomechanical tensile test of 20 minutes, the highest drift value at the 77 K setpoint temperature provides an upper bound for an average temperature change of 0.7 K.

Figure 2-10 shows the sample-to-heater and mount-to-heater temperature differences, measured at five setpoint temperatures with the use of a radiation shield. At the lowest setpoint temperature, the mount-to-heater temperature difference was 4.08 K, whereas the temperature difference between the sample and heater was as high as 67.0 K. At the high-temperature target of 475 K the differences are smaller, with temperature offsets at the mount and sample of 0.9 K and 23.4 K, respectively. Nevertheless, a stable steady-state temperature at the sample was attained during both heating and cooling cycles, although the experimental temperature differences along the thermal path from heater to sample signify the importance of additional heat transfer mechanisms. Namely, the vacuum environment in the cryostat eliminates convective and air conduction heat losses from the chamber, but thermal radiation and solid conduction losses remain. Radiation played an important factor in the measured temperature offset due to the large temperature difference between the cryostat and the laboratory and the close proximity of the sample to the top flange and window. At low temperature, infrared radiation emitted from the cryostat chamber walls was partially absorbed by the sample and its surroundings, while at high-temperature the sample lost heat via radiative losses. To verify if radiation, resulting from a temperature gradient in the system, was the dominant

source of thermal loss, a Peltier module was placed near the cryostat window to cool the window during LN_2 flow into the cryostat. A decrease in sample temperature confirmed that radiation is a main source for temperature offset.
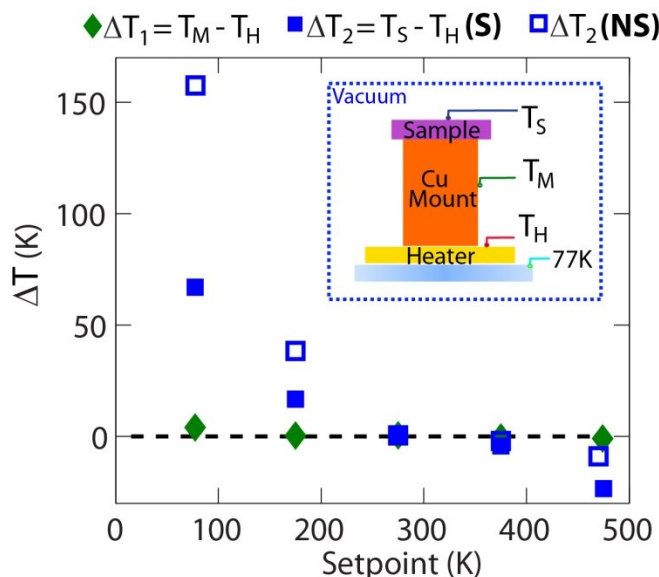
Figure 2-10 Temperature difference between copper mount and heater, ΔT_1, and sample and heater ΔT_2. The latter includes measurements both with a radiation shield (S) and without (NS, open squares). The inset is a schematic of the cryostat cross-section showing the connected temperature sensors (top to bottom) at the sample, copper mount, and heater. The liquid nitrogen flow path is at the base of the cryostat.

In order to reach low temperature offsets at the sample, solutions to reduce the influence of thermal radiation at low setpoint temperatures were implemented. An aluminum radiation shield on the ceramic package was hence introduced to reflect radiation incident from the surroundings. The shield was cut from a sheet of aluminum foil and secured to the top of the ceramic package with Kapton tape. An aperture was cut in the middle of the foil to allow viewing of the testing stage as well as preventing contact between the foil and the wire bonds. During LN_2 cooling down to 77 K, the temperature difference between the sample and heater was reduced by as much as 90 K

57

with the presence of the radiation shield. In general, the shield provides optimal conditions for testing particularly at setpoints below room temperature.

Since the specimen to be tested was mounted on polysilicon grips suspended above the testing stage substrate, it is worth commenting on heat transfer mechanisms to the suspended specimen being tested. In order to determine the temperature difference between the substrate and the grips, a package containing a device without a clamped nanowire was mounted on a Peltier heating stage under a confocal Raman microscope (Figure 2-11). Raman spectra were obtained in air at room and elevated temperatures from both the device grips and substrate. The frequency of the strongest peak in the Si Raman spectrum displays a linear dependence on temperature near room temperature [206,207], and this dependence was used to measure temperature rise as the setpoint was increased (Figure 2-11). Substrate temperatures measured between 295 K to 383 K agreed well with the temperature measured at the grip, with any differences being within the uncertainty of the Raman measurement (~3 K). We attribute this efficient heat transfer primarily to solid conduction through polysilicon and air conduction across a gap of about 2 μm from the substrate, overwhelming the expected heat loss to the surrounding air environment. These mechanisms are consistent with other reports of dominant heat transfer mechanisms in MEMS structures [208,209]. In vacuum, in the absence of air conduction from the substrate, it is expected that conduction through the polysilicon will still enable the grips to stabilize at the substrate temperature within the stabilization timeframe.
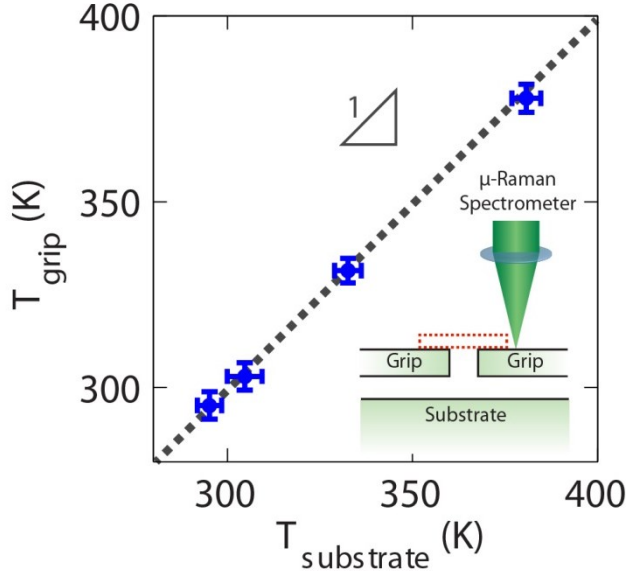
Figure 2-11 Raman thermography measurements of the substrate ($T_{substrate}$) and grip (T_{grip}) temperatures. Error bars represent the standard deviation of 20 measurements. The dotted line has a slope of 1, corresponding to thermal equilibrium between the substrate and the specimen grips. The inset is a schematic of the temperature measurement setup under the Raman objective. The dotted outline indicates where a Pd NW would be placed.

2.3.2 Optimizing Optical Image Quality

The use of conventional infinity-corrected objectives (Olympus SLMPLN-N 100x) in air can produce clear images of the comb structures with high contrast at the edges requisite for precise DIC (Figure 2-12). The degree of contrast can be quantified by examining histograms of gray-scale values (averaged RGB values at each pixel) for each image; for the first configuration there are both a large range and a bipolar distribution representative of the light-dark contrast at the comb finger edges. However, the presence of glass between the objective and sample introduces spherical aberrations: instead of incoming light focusing on a single plane, the focal plane is "spread" along the optical axis, resulting in blurred features and lower contrast. This is evinced in the collapsed gray

value histogram and the fewer sub-image points on only the inner side of the comb features that have been used successfully for correlating images captured under this condition. To compensate for the aberrations from the window, an adjustable multi-lens, aberration-correcting objective (Olympus LUCPLFLN 40x) was successfully employed to recover the high contrast of the window-less setup. The combination of aberration correction and sub-pixel correlation resolution led to peak-to-peak displacement noise below 100 nm, as described below.
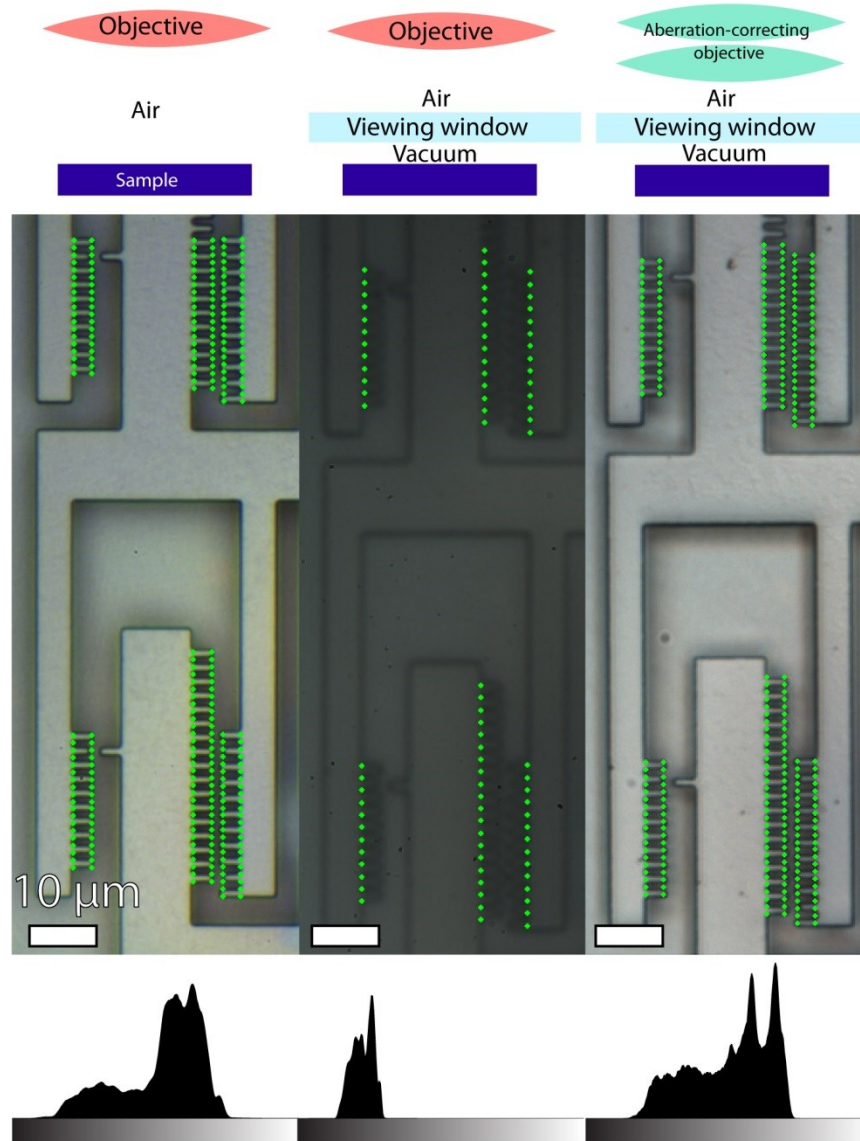
Figure 2-12 Comparison of image contrast for three imaging configuration. From top to bottom, schematics of each imaging setup, optical micrographs showing the comb structures on the tensile testing device as obtained from each setup, and their respective gray value histograms. The gradient bar under each histogram represents averaged RGB values from 0 (black) to 255 (white). The green points overlaid on each micrograph are the sub-image centers used for digital image correlation (DIC) displacement tracking.

2.3.3 Imaging Noise during Non-ambient Temperature Testing

The displacement noise floors at different temperatures reflect the various sources of vibrational noise acting on the cryostat, as shown in Figure 2-13. At room temperature, only the vacuum pump was constantly running and the peak-to-peak displacement noise is at a minimum of 25 nm. The addition of constant cryogen flow at 77K increased the noise slightly. To operate at elevated temperatures, either LN_2 or N_2 gas must circulate through the cryostat to actively compensate for any overshoot by the heater; in addition, the heater power operates intermittently in response to the PID feedback loop. These factors resulted in larger noise in the displacement measurement with a maximum peak-to-peak value of 62 nm at 470 K. Both peak-to-peak and standard deviation values in nanometer and pixel units are reported in Table 2-1 and plotted as a function of setpoint temperature in Figure 2-13(b).
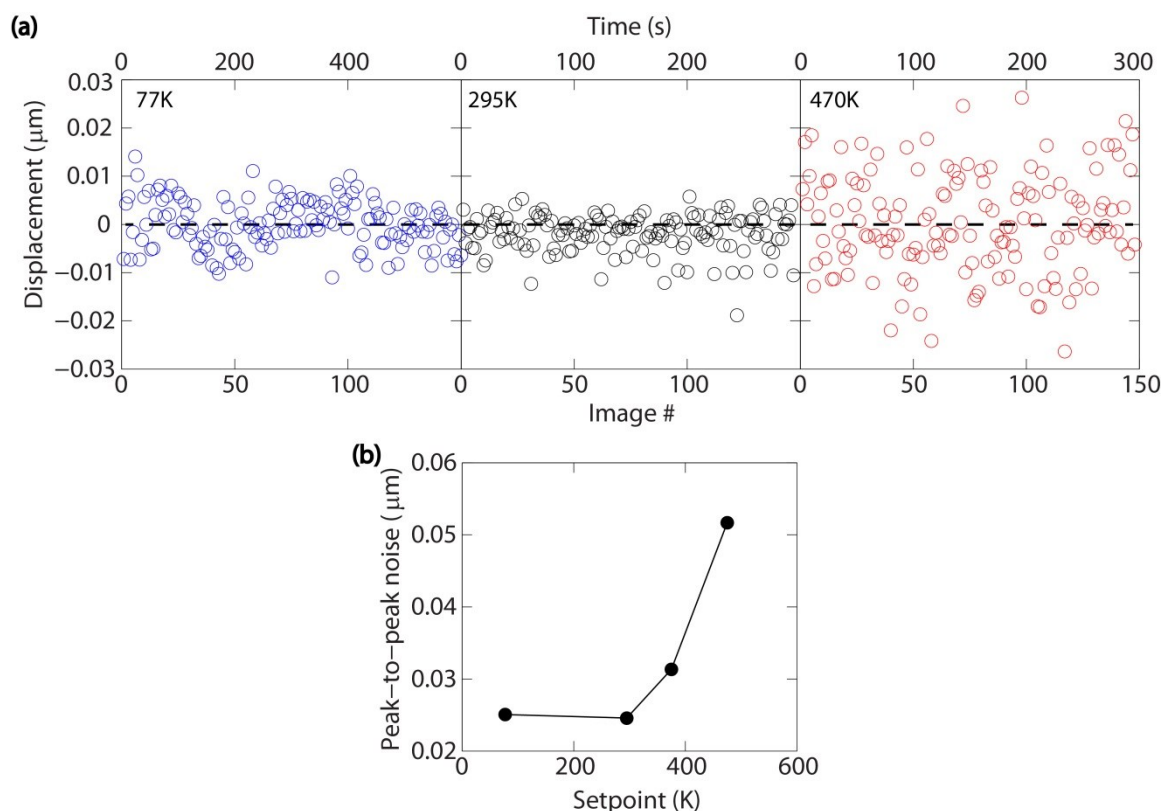
Figure 2-13 Spatial resolution for imaging during cryostat operation. Time-dependent displacement values measured for a stationary setup, representing the noise for each testing temperature. Noise is the lowest at 295 K due to the absence of cryogen or coolant flow and heating. (b) Peak-to-peak displacement noise measured at different setpoint temperatures.

Table 2-1 Measurements of in-plane displacement noise at various setpoint temperatures. All data reported below were measured from 150 sequential images.

Setpoint	Peak-to-peak		Standard deviation		Total Capture Time	Capture Interval
(K)	(nm)	(pixels)	(nm)	(pixels)	(s)	(s)
77	25	0.27	5	0.054	600	4
295	25	0.27	4	0.043	300	2
375	31	0.34	5	0.055	300	2
470	62	0.68	11	0.119	300	2

63

2.3.4 Effects of Drift Along the Optical Axis

Under the optical microscope, out-of-plane drift along the optical axis (z-direction) is prevalent during temperature ramping and tensile testing. This can be compensated by using a closed-loop piezoelectric objective scanner with a range of 200 μm and a resolution of 1 nm. As off-focus imaging can skew relative displacement measurements between the various comb features during load-unload tests and result in false displacement values, a test was conducted to quantify the artificial in-plane displacements as a consequence of the z-drift. Image sequences were taken while adjusting the objective in increments of $z = 0.2$ μm (relative to the z=0 focal plane) to an absolute displacement of 2 μm away from focus. Using z=0 as the base image, DIC conducted on the image sequence determined the net in-plane aberrant displacement between the anchor and actuator combs as a result of defocusing. A maximum value of 0.26 μm in-plane displacement was measured at 2 μm off-focus. Over the course of a typical tensile test in which drift in Δz is less than 0.2 μm, as indicated by the shaded region in Figure 2-14, the artificial in-plane displacement reaches a maximum of 0.012 μm. While the artificial displacement can be substantially minimized by adjusting focus during testing (i.e. this measurement represents an upper bound for drift), the measured maximum displacement of 0.012 μm displacement remains low compared to the minimal peak-to-peak noise of 0.025 μm due to in-plane vibrations, as was shown in Figure 2-13(b).
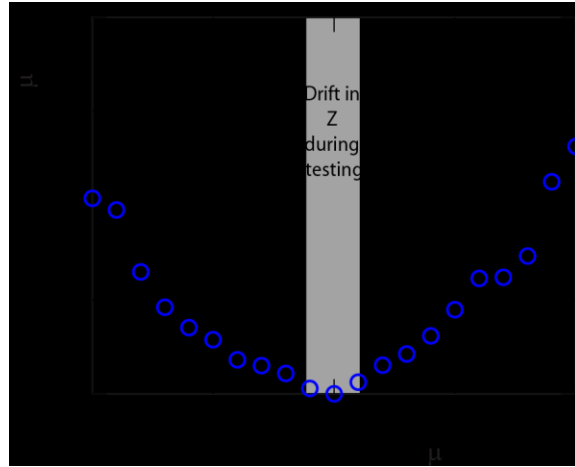
Figure 2-14 Artificial in-plane (XY) displacement due to drift from z-focus, measured as the absolute position relative to focus at z=0. The shaded region, indicating a ±0.2 μm range in z-drift typical for an average test, corresponds to a maximum in-plane displacement of 12 nm.

2.3.5 Cooling/heating to target temperature

Prior to testing at a non-ambient setpoint temperature the ceramic package was first loaded onto the copper mount. A layer of thermal paste (either Apiezon N or Krytox for low- or high-temperature testing, respectively) was applied evenly onto both the mount surface and the bottom side of the ceramic package with a thin flat-edge. The package was then tightly clamped onto the copper mount, limiting any gap spacing between the package and the mount to ensure direct contact as well as to establish electrical connections to the MEMS device. Direct contact of the package and the mount enhanced thermal conduction for heating and cooling and additionally prevented the top of the package from touching the cryostat window. After securing the aluminum radiation shield with Kapton tape onto the ceramic package, the sample thermocouple was adhered onto the silicon chip surface with a double coating of silver paint. A piece of Kapton tape

was placed to flatten the thermocouple onto the ceramic package and prevent contact with the cryostat window.

At that point, the device was ready for testing. After running a load-unload tensile test at ambient conditions to ensure chip actuation and operation, the cryostat chamber was sealed by tightly screwing the top plate. Following a roughing stage, the turbo pump was initialized to achieve vacuum. A transfer line, connecting the LN_2 dewar to the cryostat inlet, was secured for subsequent cryostat cooling. The microscope objective was centered above the MEMS testing stage and the focus was adjusted approximately every 10 minutes. Once a pressure of $\sim 10^{-6}$ mbar was reached (typically after a few hours of pumping), an additional load-unload test at room temperature (this time under vacuum condition) was run to again verify chip actuation. Temperature readings from the Si diode sensor and thermocouples were recorded through a custom LabView program. Once recording was initiated, the cryostat could then be set to reach the designated setpoint.

For heating, a PID temperature controller was used to achieve and maintain the target temperature. Since a coolant was required to actively compensate in case of temperature overshoot, LN_2 flowed from the dewar and into the cryostat via the transfer line. Manual regulation of the flow of cryogen into the chamber was achieved via a valve at the transfer line.

Temperature values reported for a given experiment were calculated from the average temperature profile in the steady-state regime over the duration of a tensile test. A typical time of 1500-2500 seconds was needed to achieve temperature stability, as

shown in Fig. 2. After steady-state temperature was reached, imaging conditions were then verified to prepare for tensile testing at the stable temperature. Tensile testing could proceed once the focus remained fixed, in order to reduce artificial in-plane displacements as discussed in section 2.3.4. A fixed nominal strain rate was programmed and the Pd NW specimen was run through several load-unload cycles before ultimately fracturing. Low-resolution DIC was performed real-time as images were being acquired during tensile testing to monitor progress and identify when yield or fracture occurred.

2.4   In situ TEM experiments

Similar to the manipulation procedure outlined in section 2.2.2, individual Pd NWs were aligned and mounted on a MEMS fabricated push-to-pull (PTP) device [210,211] (Figure 2-15). A PI-95 TEM PicoIndenter from Hysitron Inc. [126,212] was then used to push the semicircle head of the PTP device with a diamond flat punch indenter at a constant displacement rate of 4 nm/s, pulling the bridged Pd NW in tension. Load and displacement data were recorded and converted to stress-strain response of Pd NWs based on a procedure similar to Refs. 60 and 61.
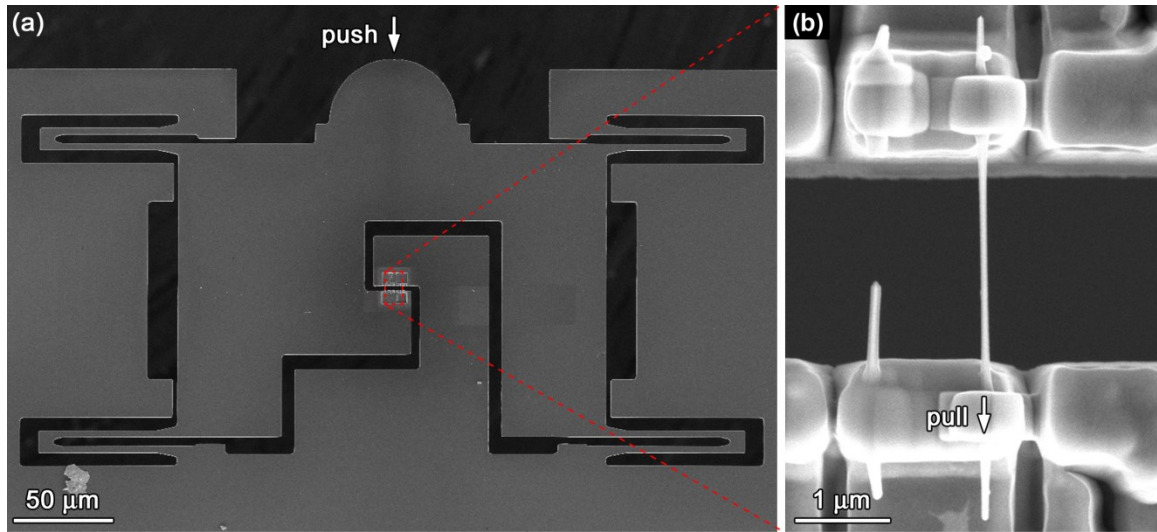
Figure 2-15 (a) SEM micrographs of push-to-pull device and (b) a secured NW. *Images and data courtesy of Dr. Mo-Rigen He.*

The resolution of the recorded load displacement signals was < 0.2 µN and < 1.0nm, respectively. The spring constant of empty PTP device, i.e. the four springs loaded in parallel with the tested NW, was measured after NW fracture. The force applied to NW was thus determined by subtracting the elastic force of PTP device from the total load. The cross-section of NW was approximated as a circle, with the diameter taken as the average of projective widths with specimen holder tilted at 0° and 30°. The initial gauge length of NW was measured by SEM as the distance between the two Pt grips. The elongation of NW was considered to be uniform before fracture and simply equal to the displacement of indenter, since the compliance of Pt grips has been shown to be negligible [190,203].

3 Higher-order and Size-dependent Elasticity in Pd NWs

In this chapter, we look at the room temperature elastic deformation of Pd NWs. Using the MEMS-based tensile testing stage, we have performed tensile tests on single-crystalline, defect-free Pd nanowhiskers (NWs) at room temperature and measured nonlinear elastic response at applied axial strains in excess of 1%. By analyzing the size-dependence of the second and third-order elastic constants, we deduced a size-independent nonlinearity parameter, which allowed for direct comparisons to lattice anharmonicity in bulk FCC metals. Our pristine nanoscale crystals and unique testing approach provided results of both nanoscale mechanical phenomena and bulk behavior beyond the limit accessible by conventional macroscopic methods.

3.1 Verifying Elastic Response in Pd NWs

Figure 3-1(a) shows representative load-unload stress-strain curves for two nanowhiskers with different diameters (110 and 33 nm) as well as subsequent loading curves to fracture. Nonlinear elastic behavior was measured to occur at strains as high as ~5% and stresses in excess of 4 GPa. Some specimens displayed plastic deformation preceding fracture, which could be clearly distinguished from the elastic regime (e.g. 33 nm specimen shown in Figure 3-1(a)). We note that measured fracture strengths were as high as 7.1 GPa (corresponding to resolved shear stresses on the $\{111\}/\langle11\bar{2}\rangle$ slip system

of ~8% of the shear modulus of Pd), which are near estimates of the theoretical shear strength, consistent with other reports of high strength in FCC nanowhiskers [21,27]. To confirm the elastic limit of our Pd nanowhiskers, the actuator position was fixed at various increments of strain, and load was measured for ~1 min hold periods, as shown in Figure 3-1(b). For holds at approximately 0.5, 1.2, and 3.1 GPa, no clear load relaxation was measured, indicating the absence of detectable plastic deformation in this regime of nonlinear mechanical behavior. Measurable load relaxation was only measured at stresses higher than 4 GPa, which directly preceded fracture of the sample. These experiments reveal a large range of elastic strain over which both linear and nonlinear elasticity can be quantified. Our data show a quadratic fit to sufficiently capture the nonlinear response until fracture (inset of Figure 3-1(a)).
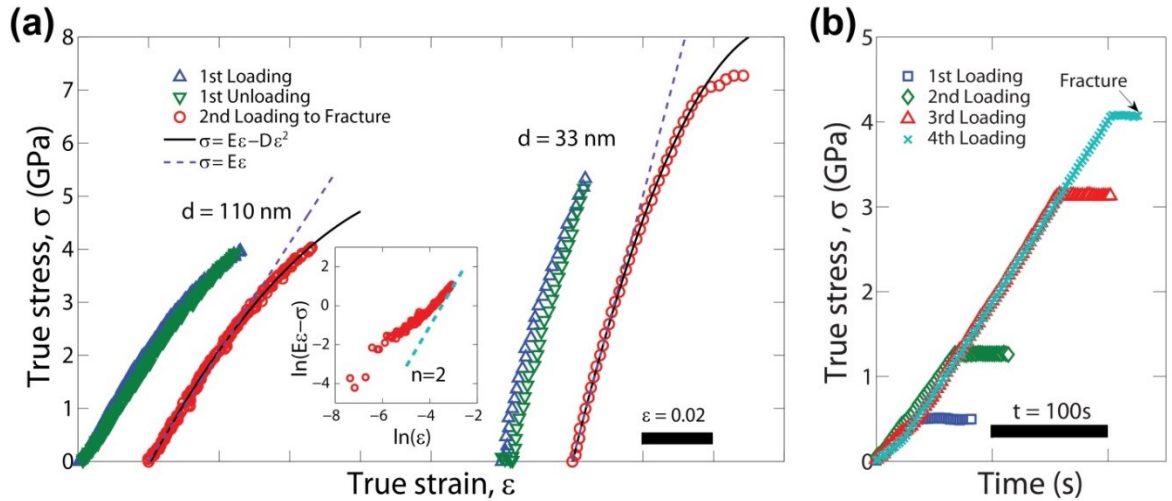
Figure 3-1 Representative elastic behavior in Pd NWs. (a) Loading, unloading, and subsequent fracture (offset along strain axis for clarity) stress-strain curves for two Pd NWs. Load-unload tests indicate no residual strain in NWs after unloading. Linear and quadratic fits (reconciled by the power law exponent shown in the inset) to the fracture curves are shown. (b) Stress-time data for a representative Pd NW, during which the actuator was held stationary, confirming elastic behavior until near the fracture stress.

70

3.2 Characterizing Size-dependent and Higher-order Elastic Behavior

The moduli E and D were directly determined for all tested Pd NWs by nonlinear least-squares fitting of the measured tensile response to Eq. 1-8. D was measured to be negative and with absolute values an order of magnitude larger than E, indicating a strong elastic softening beyond the linear (Hookean) regime. Most notably, both E and D were measured to be size-dependent, with increasing absolute values with decreasing NW diameter (Figure 3-2). E was measured to be approximately 120 GPa for NWs larger than 100 nm, which is close to the bulk value of Young's modulus in Pd for a <110> axial orientation (136 GPa) [214], while increasing to ~290 GPa in the 33 nm NW (Figure 3-2(a)). While the linear response at low strains was shown to stiffen with decreasing size, D was measured to correspondingly decrease (increasing magnitude) (Figure 3-2(a)), revealing a more pronounced deviation from linear behavior in the smallest tested NWs.
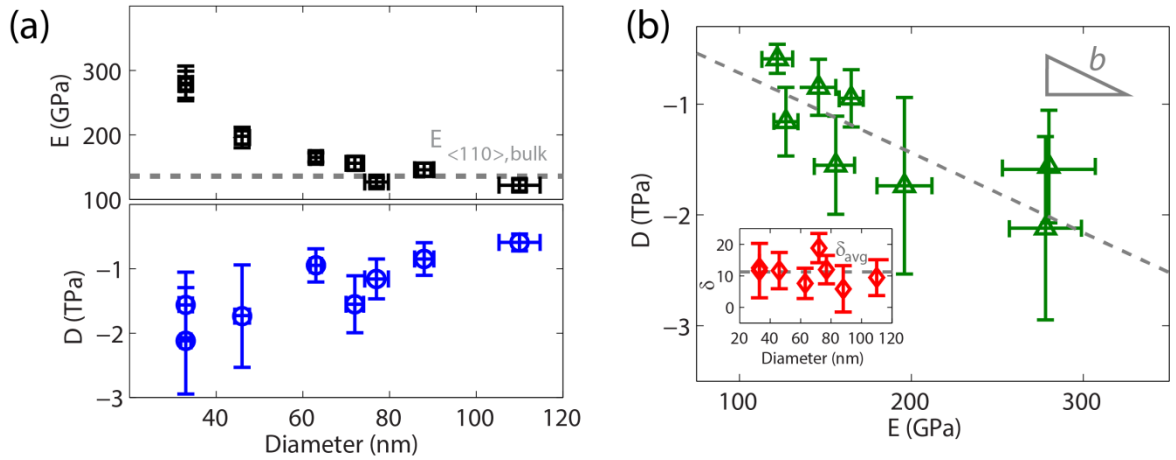
Figure 3-2 Size-dependent elastic behavior. (a) E and D obtained from least-squares quadratic fitting, showing a clear dependence of both quantities on NW size. (b) Plotting E vs. D demonstrates a linear correlation, suggesting that the slope b, the strain-expanded

71

nonlinearity parameter, is an intrinsic size-independent property. The inset confirms that the nonlinearity parameter δ is not a function of diameter over the tested size range. See Section 7.1 for details on the error analysis.

That both linear and higher-order elastic constants show size-dependence is noteworthy. Figure 3-2(b) shows E and D to be roughly linearly correlated, which suggests that an additional material parameter can be defined that is size-independent, and hence, representative of a bulk-like quantity. Such an approach can be reconciled by considering the elastic strain energy as a function of interatomic separation during uniaxial loading of our NWs. Following Diao *et al.*[26], by accounting for Poisson contractions, a relationship between Eq. 1-8 and the strain energy $U(\varepsilon)$ of a nanowire with Poisson's ratio υ and initial volume V_0 subjected to uniaxial tension can be expressed as:

$$\frac{U(\varepsilon)}{V_0} = E\left(\frac{1}{2}\varepsilon^2 + \frac{1}{3}\beta\varepsilon^3\right) = E\left(\frac{1}{2}\varepsilon^2 + \frac{1}{3}(1 - 2\upsilon + b)\varepsilon^3\right) \qquad \textbf{Eq. 3-1}$$

where $b = D/E$, the so-called strain-expanded nonlinearity parameter. Because $b \propto \partial^3 U / \partial\varepsilon^3$ (i.e. related to third-order elastic constants), a constant b implies a signature of the interatomic behavior of a crystal corresponding to nonlinear behavior in bulk Pd. We measure $b = 7.19 \pm 1.94$, i.e. bulk Pd should elastically soften in tension along the <110> direction. While experiments of bulk Pd elastic behavior at high strains are not available, molecular statics simulations of higher-order elastic moduli in other bulk FCC metals have been performed [26,35]. Liang *et al.* found that in bulk Cu along the <110> direction, the instantaneous stress-strain slope decreases ($b_{110} = -9.885$) (agrees with our findings) as well as along <111> ($b_{111} = -0.587$) but increases for <100> ($b_{100} =$

4.155)[35]. A similar trend in atomistic simulations of bulk Au was observed by Diao *et al.* where the Young's modulus along the <100> direction was found to decrease with compressive strain, i.e. b_{100} is positive[26]. Comparing our results with these findings, the response of the tested Pd NWs along the <110>-direction is consistent with predictions for the interatomic behavior of FCC metals. As the magnitude of *b* is a direct measure of the degree of anharmonicity, one can estimate the anharmonic contribution by considering the relative deviation from a harmonic approximation (1st term of Eq. 3-1). We write a dimensionless expression for the fractional anharmonic contribution to the strain energy density as $2/3(1-2\upsilon+b)\varepsilon$. Using $\upsilon = 0.39$ and our measured value of *b* for Pd nanowhiskers, this value would be ~ 5% and ~25% for strains of 0.01 and 0.05, respectively, suggesting that anharmonicity plays a substantial role particularly near the fracture strain.

Further comparisons with nonlinear elastic behavior in FCC metals can be made by expanding in stress rather than strain, according to Eq. 1-10 [57]. Using this framework, we measure $\delta = 11.2 \pm 3.9$ for our <110> Pd NWs (inset of Fig. 3(b)), which, to the best of the authors' knowledge, is the first measurement of δ in Pd. Nevertheless, it is still insightful to compare to δ values obtained in other FCC noble metals [56,57,59,60], which are consistent in sign for each low-index orientation (negative for <100>, positive for <110> and <111>), with the magnitude of δ_{110} usually being the highest (typical values in noble metals range from ~8 to ~11). Also noteworthy is the qualitative agreement between these experimental studies and the simulations by Diao *et al.* of <100>-Au and by Liang *et al* in Cu for all three

directions[26,35]. Comparing with the current work, our value δ_{110} obtained for Pd is the largest among other FCC metals but consistent in sign and magnitude, suggesting a very large degree of anharmonicity (Table 1-1).

3.3   Evaluating the Physical Origins of Size-dependent Elasticity

Having shown a direct measurement of the size-independent nonlinearity parameter in Pd along the <110> direction, we now turn our attention to the size-dependence of E and D. As mentioned in section 1.2, such size-dependence in E is commonly attributed to the effect of increasing surface-to-volume ratio in nanostructures via two separate effects. The first is the contribution of a surface layer with distinct elastic properties from the bulk to the total stiffness of a nanostructure, a direct result of the atomic bonding configuration near a free surface [32,65,79]. In this case, the total surface stress along the nanowire axis is often represented as $\tau = \tau_0 + S\varepsilon$, where S is the surface stiffness (or surface elastic modulus) and τ_0 is the surface stress at zero applied strain [30,64]. This contribution of the surface stiffness S leading to the deviation in E from the bulk value E_0 is estimated by $(E - E_0)/E_0 = \alpha(h/h_0)$ where α is a geometric factor, $h_0 = |S/E_0|$, and h is the characteristic length scale of the structure [32,64]. Using surface stiffness values obtained from atomistic simulations [64], we calculated h for several low-energy surfaces ({100}, {110}, {111}, and {112}) on a <110>-NW assuming a square h x h cross-section under tension ($\alpha = 4$). For a 10% difference in apparent E (sufficiently large so as to be measured in our experimental setup), $h < 4$ nm, which is well below where our Pd NWs begin to show deviations from bulk elastic behavior. We

74

note that other experimental and atomistic simulation studies of nanowires also show deviations in E due to surface stiffness at similarly small length scales [30,71,83,215]. It is important to recognize that this model assumes a linear elastic response of miscoordinated atoms residing at the surface. Also, to account for changes in stiffness in perfectly coordinated atoms, the surface must be able to affect the response of the fully coordinated core atoms. This can be accomplished by way of a second effect, namely, via surface-stress-induced relaxations [35,81,82]. Changes in bond lengths near the surface can result in large values of τ_0, which in equilibrium must be balanced by stresses in the material core [30,64,81]. Surface stress effects on the elastic response of nanowires have been extensively modeled [30,83,215,216], but the core stress is often assumed to exhibit linear elastic response. Both Diao *et al.* and Liang *et al.* have found in their simulations that the variations in E with decreasing size in Au and Cu NWs, respectively, can be attributed to higher-order elastic behavior, arising from a surface stress-induced residual stress state along the axial direction of the wire [26,35]. Compressive residual core strains > 0.01 sufficiently shift the initial stress state and thus the apparent E, giving rise to size-dependent elastic behavior. Since we have determined the E and b values for our Pd NWs, we can similarly estimate the residual axial core strain ε_r by using the expression $\varepsilon_r = (E/E_{bulk} - 1)/2b$ (Figure 3-3). This simple approach does not take into account the effects of the surface in the transverse directions, but it does illustrate the significant role the surface may play in evaluating the yield and fracture strength in FCC metal nanostructures.
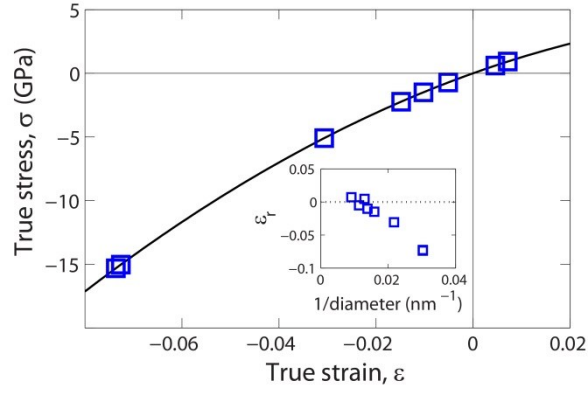
Figure 3-3 Estimation of relaxation strain ε_r along the NW axis. The provided inset shows increasingly compressive relaxation strains for NWs with smaller diameters. The bulk curve for Pd is plotted using the relation in Eq. 1 with D/E = -7.19. The anomalous points indicating positive ε_r result from calculations with E values near the bulk value.

4 Dislocation Nucleation-mediated Plasticity in Pd NWs

In the previous chapter, it was shown that remarkably high yield stresses could be attained in the Pd NWs, enabling characterization of their higher-order elastic response. These high strengths were achievable due to the absence of pre-existing carriers of plasticity such as dislocations. Hence, the initiation of plastic deformation required nucleation of such defects, a process that has been predicted to be thermally activated.

Here, we aim to gain a quantitative description of the energetic and kinetic barriers to surface dislocation nucleation in pristine crystals. We present systematic experimental tensile tests performed on defect-scarce single-crystalline Pd NWs where dislocation nucleation is the predominant mechanism underlying plastic yielding. By employing the MEMS-based testing platform in a temperature-controlled environment, we have probed the quasi-static tensile response over a range of strain rates, sizes, and temperatures, even approaching the athermal limit. With the aid of *in situ* tensile tests in the TEM, we demonstrate a direct connection between incipient plasticity in our NWs and the nucleation of dislocations at free surfaces. Our measurements of over 60 NWs provide values for the energy barriers and kinetics governing dislocation nucleation, as well as insight to the highly probabilistic nature of dislocation nucleation.

4.1 Tensile behavior of Pd NWs

As mentioned in the last chapter, Pd NWs were subjected to successive load-unload tests to increasingly higher displacements until fracture. Even at room temperature, the Pd NWs exhibited large ultimate strengths as high as 7.8 GPa, over 70 times stronger than their bulk counterparts. In all Pd NWs tested, the elastic response became nonlinear at strains above 1% [190]. Systematic unloading beyond the linear (Hookean) regime showed the deformation path to follow the nonlinear loading curves and return to zero strain, indicating elastic behavior. In the vast majority of samples tested, plastic deformation was immediately terminated by a brittle-like response, i.e. no measureable plastic strain in the stress-strain curve (e.g. 110 nm-diameter sample in Figure 3-1(a)).

The load-hold tests are of particular importance, demonstrating sustained elasticity and the absence of relaxation mechanisms at stresses well below the yield or fracture strengths. Figure 3-1(b) shows subsequent loading of a single NW, which sustained a relatively constant load at increasingly higher levels of stress until fracture occurred during the final holding period. The finite duration of time (~24 s at 3.8 GPa, engineering stress) required for yield to occur under constant stress is consistent with a thermally activated mechanism and can be related to the expectation time for the first nucleation event.

4.2 Linking Incipient Plasticity to Dislocation Nucleation

The measured stress-strain response in our Pd NWs indicates that plastic deformation is incipient at the yield point and suggests that defect nucleation is associated with the first measured deviations from elasticity. However, *in situ* TEM tests performed on other metallic nanostructures with nonzero defect density have shown that dislocation motion may still occur during what would otherwise appear to be elastic loading [211]. To fully establish the link between incipient plasticity and the measured departure from elasticity in the stress-strain curve, we performed quantitative *in situ* TEM tensile tests of Pd NWs.
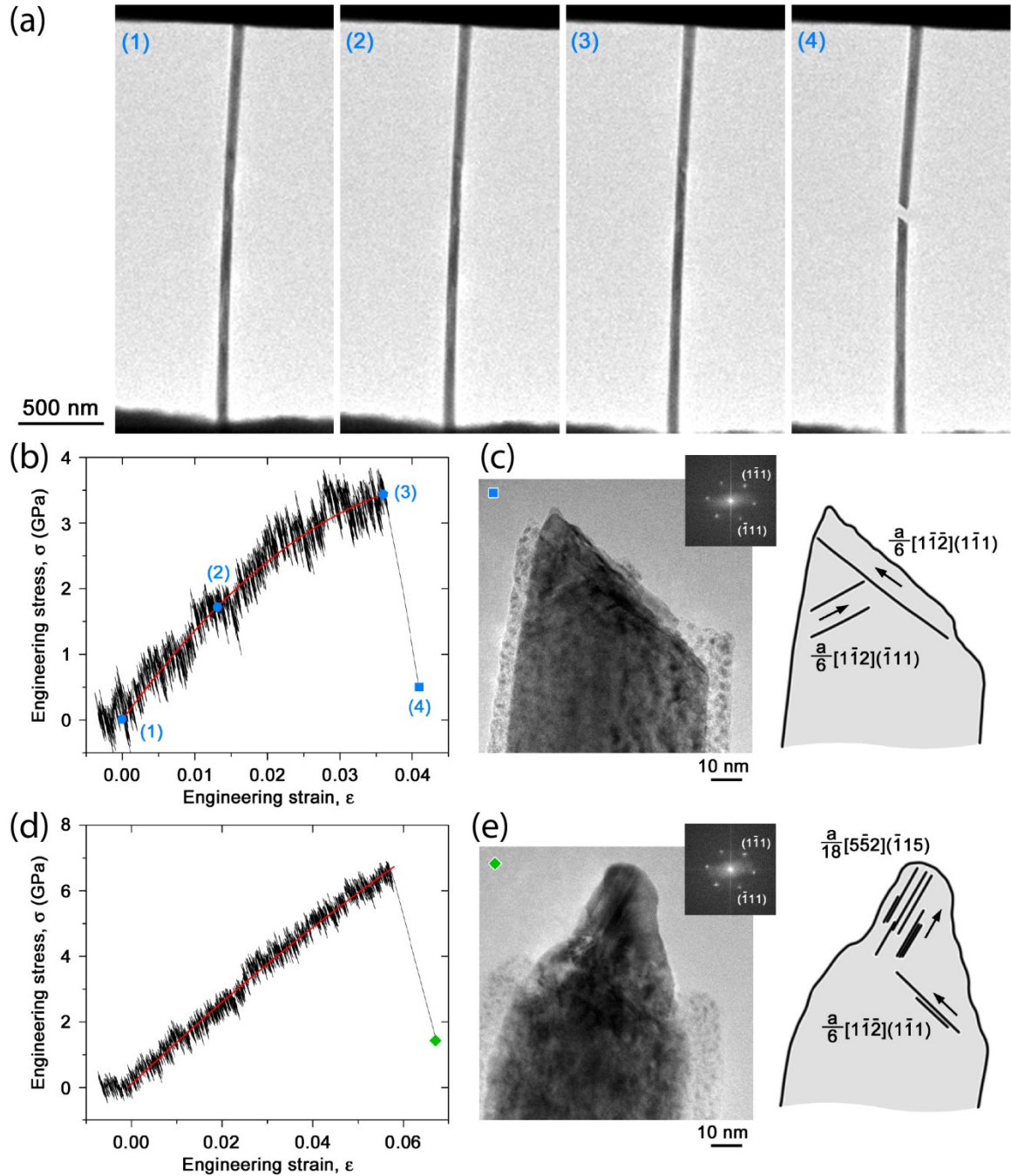
Figure 4-1 In situ TEM tensile testing.

(a) Sequential images from a single tensile test on a Pd NW, (b) the corresponding stress-strain curve with a quadratic fit for the nonlinear response (red line), and (c) the fracture morphology showing stacking faults from equivalent slip systems. (d) A second Pd NW of similar diameter tested under identical conditions and (e) the fracture morphology

showing sequential twinning on different slip systems. *Images and data courtesy of Dr. Mo-Rigen He.*

Figure 4-1(b) shows a series of images captured during tensile testing of a Pd NW with a diameter of 60 nm, and Fig. 2(c) shows the corresponding stress-strain curve, which is well described by a nonlinear (quadratic) elastic relationship before fracture, as reported previously [190]. For this NW, diffraction contrast related to defects, such as dislocations and stacking faults, was not observed at the beginning of test (snapshot 1 in Figure 4-1(b)). Moreover, the NW remained defect-free during the test, e.g. near the onset of nonlinear elasticity (snapshot 2) and before the NW fractured (snapshot 3) at a stress of 3.45 GPa. Subsequently, the NW abruptly fractured (snapshot 4) in a shear mode (see Figure 4-1(d)), with a shear plane determined to be $(1\bar{1}1)$ since the NW was oriented along $[1\bar{1}0]$ and observed in the [110] zone axis. Traces of stacking faults were observed parallel to the major $(1\bar{1}1)$ shear plane (and the equivalent $(\bar{1}11)$ plane), indicating that the shear fracture likely occurred by activation of a series of identical partial dislocations with $\boldsymbol{b} = [\bar{1}12]\,a/6$ (and the equivalent $\boldsymbol{b} = [1\bar{1}2]\,a/6$) from the side surfaces, which accorded well with previous atomistic simulations and *in situ* SEM measurements of Au NWs [213]. Notably, no visible surface steps were evident during or after loading away from the fracture edge, which could arise from dislocation avalanches operating at speeds faster than our video rate. Figure 4-1(e)-(f) shows the stress-strain curve and fracture morphology of another defect-free Pd NW with a diameter of 64 nm, which was elastically loaded to 6.7 GPa and then fractured in a

81

necking-like mode. Traces of stacking faults (or twinning planes) were also observed

only near the fracture edges. A Schmid factor analysis suggested that plastic deformation

in this NW was mediated by partial dislocations (or twinning segments), operating in a

primary slip system with $b = [\bar{1}12]\,a/6$ on a $(1\,\bar{1}1)$ plane, followed by a secondary system

with $b = [5\bar{5}2]\,a/18$ on a $(\bar{1}15)$ plane with respect to the matrix orientation, which is

equivalent to $b = [1\,\bar{1}2]\,a/6$ on the $(\bar{1}11)$ plane in the primary twinned region. Such a

plasticity mechanism mediated by multiple partial dislocations is consistent with previous

studies of Au NWs grown in similar conditions, underscoring the role of dislocation

nucleation from the surface of these NWs.

Our *in situ* TEM testing revealed that mobile dislocations were neither present

inside the Pd NWs prior to testing nor during the entirety of the evidently elastic regime.

However, clear evidence of late-stage plastic deformation strongly suggests that

nucleation of dislocations directly prior to fracture gives rise to highly localized plastic

deformation followed by final fracture. Thus, the yield strengths measured in this study

serve as a reasonable indicator of incipient plasticity and can be used for the evaluation of

the critical strength for dislocation nucleation. In the remainder of this article, we refer to

the measured yield strength as the nucleation strength.

4.3   Trends in Tensile Response and Fracture Morphology

Probing the dependence of nucleation strength on testing parameters such as size, strain rate, and temperature provided further quantitative insight to the nature of the underlying plasticity mechanism. Pd NWs were tested at strain rates in the range of 10^{-5} s^{-1} to 10^{-3} s^{-1} and nominal temperatures from 77 K to 475 K. In order to minimize convolution in the data, we define our benchmark conditions as NWs tested at room temperature (295 K) and an intermediate strain rate range ($\sim 10^{-4}$ s^{-1}), i.e. all non-ambient temperature tests were performed at a strain rate in the 10^{-4} s^{-1} range and all tests performed above or below 10^{-4} s^{-1} were tested at room temperature. In Figure 4-2(a), several characteristics of the tensile response, including ultrahigh yield strength in the gigapascal range and nonlinear elasticity at high strains, remain consistent among the different testing conditions. As with all samples tested on the MEMS stage, elasticity at high strengths was verified by performing load-unload tests prior to the fracture (See section 3.1).
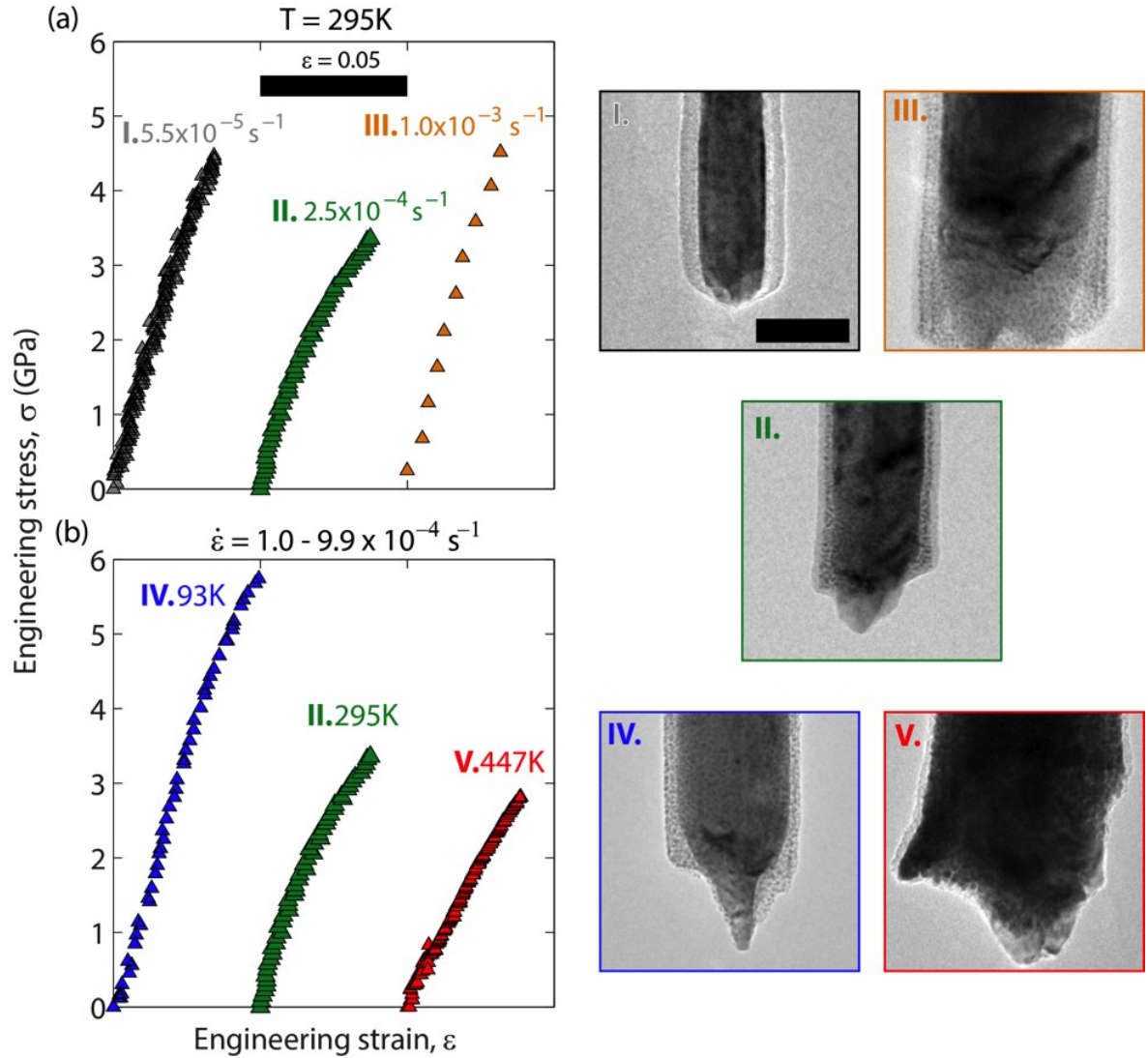
Figure 4-2 Representative stress-strain behavior at various strain rates and temperatures. (a) Stress-strain curves and (b) postmortem fracture morphologies for tensile tests performed under various strain rate and temperature conditions. All fracture micrographs are at the same magnification and correspond to the scale bar in I denoting 50nm. We note that only fractured samples in IV and V are from the respective non-ambient temperature tests in (b), but samples I, II and III were tested under the same conditions as the corresponding tests shown in (a). The hydrocarbon-based coatings are the result of NW manipulation before and after tensile testing; a detailed analysis of its influence is presented in Section 7.2.

84

Our results reveal the following trends for the nucleation strength. Changes of two orders of magnitude in strain rate do not produce significant differences in the yield strengths for all the room temperature tests. In contrast, spanning a temperature range of 300 K demonstrates significant changes in yield strength. For the tensile test performed at 93 K, a yield strength as high as 5.8 GPa was attained. In contrast, the sample tested at 447 K fractured at a much lower strength of 2.8 GPa. This strong temperature dependence points to a deformation mechanism more thermally sensitive than the flow of pre-existing dislocations in FCC crystals, the strength for which would scale only weakly with the elastic constants (for instance, one would expect only a 3.6% drop in strength, in contrast to nearly 50% measured herein, over the same temperature range [214,217]). Similar to the *in situ* TEM test, the measured tensile response indicates a brittle-like response whereas the fracture surface suggests otherwise. Fracture morphologies on all specimens indicate localized necking or shear deformation consistent with the previous *in situ* tests (Figure 4-1), suggesting that dislocation mechanisms govern plastic deformation over the entire range of tested strain rates and temperatures studied here (Figure 4-2 (b)).

4.4   Stochastic Nature of Nucleation Strengths

The experimental trends measured and illustrated in Figure 4-2(a) are qualitatively consistent with theoretical predictions, both from semi-analytical models [110,155] and computational simulations [156,218], where strength is weakly dependent on strain rate but strongly dependent on temperature. The stochasticity of the measured

nucleation strengths, however, adds a statistical facet to the mechanism, which we quantitatively analyze to address the probabilistic nature of thermal activation. For an array of tensile tests under benchmark conditions, we obtained a large range of strengths spanning several gigapascal for effective diameters ranging from 30 to 110 nm (Figure 4-3). Examining the measured strength as a function of size, either represented as diameter (Figure 4-3(a)) or gage length (Figure 4-3(b)), shows a marginal size effect relative to this scatter over the tested range. This observation is likewise consistent with predictions [110,155] and other experiments [39,155] indicating weak size effects in defect-free metallic nanostructures. To determine the origin of the large scatter in measured strengths, we first systematically consider sources of experimental uncertainty, including effects such as variation in the applied strain rate, estimation of the cross-sectional area, and load bearing by a hydrocarbon-based contamination layer. We additionally consider any correlation of measured strength with fracture location and with the presence of the axially aligned stacking faults. As detailed in the Appendix and indicated by error bars on our data, these cumulative uncertainties are substantially smaller than the measured scatter. We therefore attribute the stochasticity of our measurements to a probabilistic thermally activated deformation process.
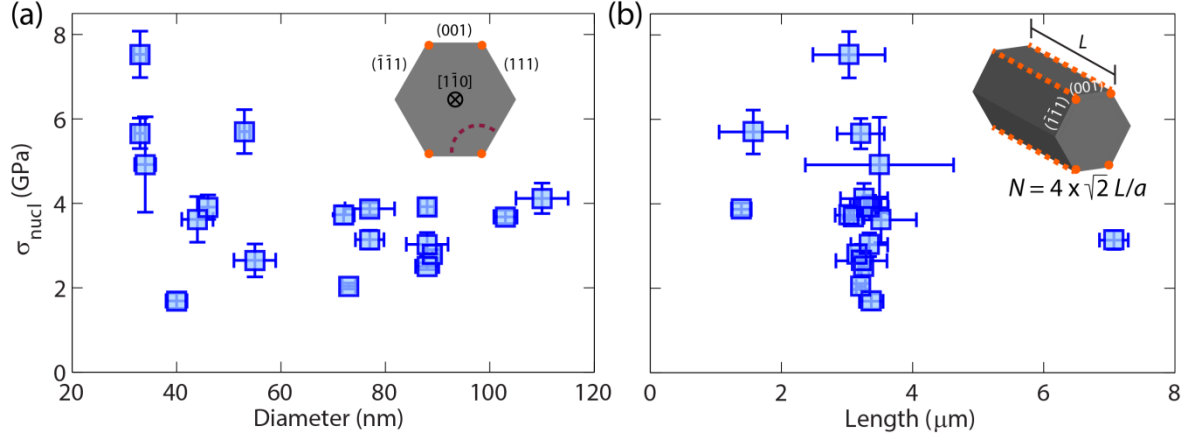
Figure 4-3 Weak size dependence of nucleation strength.
Nucleation strengths measured in Pd NWs across a range of (a) diameters and (b) gage lengths at $T = 295$ K and strain rates of the order of 10^{-4} s^{-1}. Schematics in the upper right-hand corner of each plot illustrate (a) predicted nucleation of a dislocation from a corner site and (b) relationship between length L and number of equally viable nucleation sites N for lattice parameter a. Viable nucleation sites are indicated by orange circles or orange dotted lines.

4.5 Temperature- and Strain Rate-dependence of Nucleation Strengths

Examining the full data set of ~60 NWs, we find that whereas tensile tests performed at various strain rates do not show rate dependence that rises above the scatter (Figure 4-4(a)), the nucleation strength is found to vary significantly with temperature. Comparing the mean strength values at the tested temperature limits shows a strength reduction of nearly 6 GPa over a 350 K increase in temperature (Figure 4-4(b)). This large monotonic decrease in strength with increasing temperature associated with dislocation-mediated deformation unambiguously points to a thermally activated process. In addition to the mean strength, the measured scatter band is also a function of temperature, with the largest variation emerging near room temperature and reducing in

87

both the athermal and high temperature limits. This observation can be intuitively understood as follows: in the absence of thermal fluctuations at 0 K, the NW should nucleate dislocations spontaneously at the athermal strength, resulting in a collapse of the scatter; at finite temperature, the resulting scatter will be bound at low temperatures by the athermal strength and at high temperatures by zero stress, collapsing again at a high temperature limit.

4.6 Evaluating the Thermal Activation Barriers to Dislocation Nucleation

We analyze these temperature-dependent distributions of nucleation strength to evaluate the thermal activation parameters associated with surface dislocation nucleation. For a given strain rate and temperature, the distribution of measured yield strengths can be described by a model for a kinetically-limited thermally activated process. From transition state theory (TST) (see section 1.3), the rate of dislocation nucleation υ is expressed as:

$$\upsilon = N\upsilon_0 \exp\left(-\frac{\Delta G_{act}(\sigma, T)}{k_B T}\right)$$

Eq. 4-1

where υ_0 is the attempt frequency, N is the number of equivalent nucleation sites, $\Delta G_{act}(\sigma, T)$ is the activation free energy dependent on both temperature T and applied stress σ, and k_B is the Boltzmann constant. Several simulation studies have identified a

pronounced temperature dependence for Q, attributing it to thermal effects arising from the stacking fault energy and anharmonicity [112,157]. The latter manifests as thermal expansion and thermal softening, both of which are anharmonic effects. As measurements of the elastic behavior of Pd demonstrate a pronounced anharmonicity compared to other FCC metals [190], we hypothesize that entropic contributions to ΔG are non-negligible. To directly compare our experimental results to proposed temperature- and stress-dependencies of ΔG_{act}, we adopt the simple form for the activation energy following the work of Refs. 29,45, and 46 (see section 1.3.1):

$$\Delta G_{act}(\sigma, T) = \Delta U_{act}\left(1 - \frac{T}{T_m}\right)\left(1 - \frac{\sigma}{\sigma_{ath}}\right)^{\alpha} \qquad \textbf{Eq. 4-2}$$

Here, σ_{ath} is the athermal strength, ΔU_{act} is the athermal activation energy in the absence of applied stress, and both T_m and α are constants governing the temperature and stress dependence, respectively [110]. While the analytical form for the temperature dependence in Eq. 4-2 has been a matter of some debate [112,157], it enables an approximation of the maximum activation entropy, $-\partial\Delta G_{act}/\partial T|_{\sigma=0} = \Delta U_{act}/T_m$, which we can extract from our full data set. We take T_m to be the surface-disordering temperature [110] since the bonding at the surface can significantly affect the thermal and mechanical properties contributing to the activation entropy [219,220]. The value of T_m can vary significantly for different surfaces orientations: for pristine low index surfaces such as in the current NW specimens, the temperature for surface roughening can be a large fraction of or even exceed the bulk melting temperature [221]. For simplicity, we use the convention of approximating T_m as half the bulk melting temperature.

The value of α represents the sensitivity of the activation energy to the applied stress: since the activation volume is $\Omega(\sigma,T) = -\partial\Delta G_{act}/\partial\sigma$, the decrease in the energy barrier due to mechanical work can drop dramatically near the athermal strength. Mechanistically, α is related to the particular obstacle that must be overcome during the thermally activated process. For example, for discrete obstacle-controlled plasticity in bulk crystals, $\alpha \approx 1$ (Ref. 47), thus implying a linear dependence of activation energy with stress. For the case of heterogeneous nucleation at the corner of a faceted NW, a stronger stress dependence has been proposed ($\alpha \approx 4$) based on calculations of the activation energy for simulations of corner dislocation nucleation in a Cu NW under tension [110]. We compute the full temperature-dependent nucleation strength distributions for both $\alpha = 1$ (as has been assumed for dislocation nucleation in Refs. 51 and 52) and $\alpha = 4$ to draw comparisons to our experiments (the details of the derivation for $\alpha = 1$ are included in section 7.5).

For a tensile test under a constant elastic strain rate, we can approximate the relationship between σ and time t as $\sigma = E\dot{\varepsilon}t$, where E is the small-strain Young's modulus and $\dot{\varepsilon}$ is the strain rate (average of 3.88×10^{-4} s^{-1} for benchmark experiments), and use this to define a survival probability [110]. For $\alpha = 4$, the cumulative survival probability representing the statistical transition from elastic to plastic response [110,162] is:

$$f(\sigma,T)=\exp\left(-\frac{1}{E\dot{\varepsilon}}\int_0^{\sigma}\upsilon[\sigma']d\sigma'\right)$$

<div align="right">**Eq. 4-3**</div>

$$=\begin{cases}\exp\left(\frac{N\upsilon_0}{E\dot{\varepsilon}}\left[\frac{\sigma_{ath}}{4}\left(\frac{\Delta U_{act}}{k_B}\left(\frac{1}{T}-\frac{1}{T_M}\right)\right)^{-\frac{1}{4}}\left(\Gamma\left[\frac{1}{4},\frac{\Delta U_{act}}{k_B}\left(\frac{1}{T}-\frac{1}{T_M}\right)\right]\right.\right.\\\qquad\left.\left.-\Gamma\left[\frac{1}{4},\frac{\Delta U_{act}}{k_B}\left(\frac{1}{T}-\frac{1}{T_M}\right)\left(1-\frac{\sigma}{\sigma_{ath}}\right)^4\right]\right)\right]\right) & \text{for } 0\le\sigma\le\sigma_{ath}\\[2em]\exp\left(\frac{N\upsilon_0}{E\dot{\varepsilon}}\left[\frac{\sigma_{ath}}{4}\left(\frac{\Delta U_{act}}{k_B}\left(\frac{1}{T}-\frac{1}{T_M}\right)\right)^{-\frac{1}{4}}\left(\Gamma\left[\frac{1}{4},\frac{\Delta U_{act}}{k_B}\left(\frac{1}{T}-\frac{1}{T_M}\right)\right]\right.\right.\\\qquad\left.\left.-\Gamma\left[\frac{1}{4}\right]\right)+\sigma_{ath}-\sigma\right]\right) & \text{for } \sigma>\sigma_{ath}\end{cases}$$

In the above expression, $\Gamma(a,x)=\int_x^{\infty}t^{a-1}e^{-t}dt$ is the upper gamma function. There are two

expressions for $f(\sigma,T)$ about σ_{ath}, because even in the absence of an energy barrier

nucleation is still kinetically limited by a maximum rate, i.e. $\upsilon(\sigma)=N\upsilon_0$ for $\sigma>\sigma_{ath}$. We

then fit this expression to the cumulative distribution of the experimental data at room

temperature as $F(\sigma)=1-f(\sigma)$ to obtain σ_{ath}, the Arrhenius prefactor $N\upsilon_0$, and the

temperature-scaled activation energy range $\Delta U_{act}(1-T/T_m)$ (Figure 4-4(c)). Using non-

linear least squares regression, we obtain $\sigma_{ath}=7.08\pm0.02$ GPa, $N\upsilon_0=0.065\pm0.003$ s^{-1},

and the Helmholz free energy of activation $\Delta F_{act}(T)=\Delta U_{act}(1-T/T_m)=0.236\pm0.009$ eV.

Assuming $T_m=914$ K (half the melting temperature of bulk Pd), we then calculate

$\Delta U_{act}=0.328$ eV.
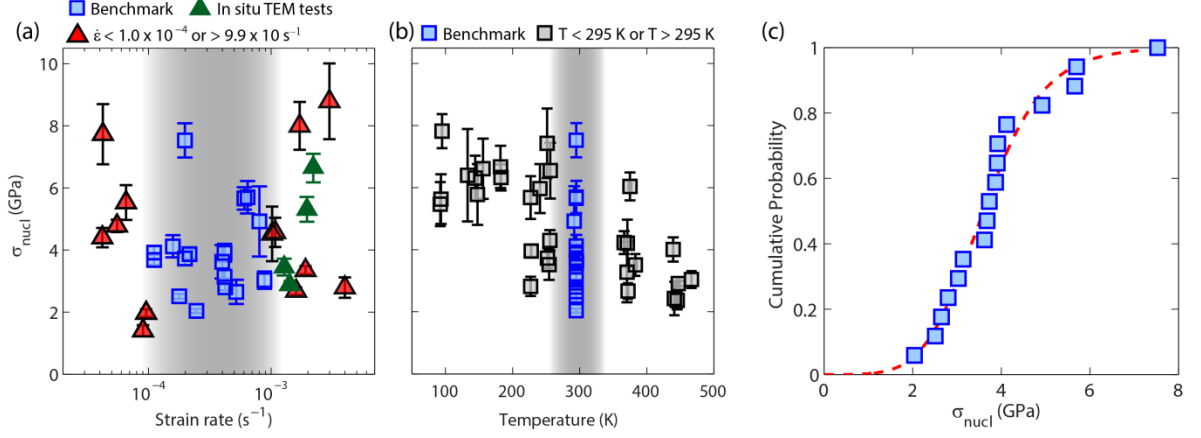
Figure 4-4 Nucleation strength in Pd NWs. Strength measured for (a) different strain rates, including results from the *in situ* TEM tests (green triangles), (b) and temperatures. Blue squares and gray shading represent measurements at 295 K and strain rates of the order of 10^{-4} s^{-1}, as displayed in Fig. 4. Measurements outside of these benchmark conditions are indicated by a different color or symbol (triangles for strain rate outside 10^{-4} s^{-1}, black for *T* outside 295 ± 5 K). (c) Cumulative probability for measured yield strengths. The dotted red line is a fit for the analytically derived cumulative distribution function $F(\sigma)$.

Using these fits, we calculate the most probable critical nucleation strength σ_c at 295 K to be 3.44 GPa, which corresponds to $\Delta G_{act} = 0.016$ eV and $\Omega = 0.13b^3$, where b is the magnitude of the full Burgers vector in FCC. In comparison, simulations of surface dislocation nucleation in a Cu NW in tension yield $\Delta G_{act} = 0.39$ eV and $\Omega = 5b^3$ at the same temperature and fraction of the athermal strength [110], at least an order of magnitude higher than our experiments on Pd NWs. Likewise, our calculated upper-bound activation entropy for Pd is $\Delta U_{act}/T_m = 4.17k_B$, implying a non-negligible contribution to the nucleation rate ($\sim \exp(\Delta S_{act}/k_B)$). This compares with calculations giving $9k_B$ and $48k_B$ for homogeneous nucleation in Cu under constant strain and stress, respectively [112]. Considering the low activation energies deduced from our

experiments, it is plausible that certain pre-existing flaws that go undetected, such as vacancies and atomic surface steps, could lower the nucleation barrier with respect to an ideal crystal. In Pd, the vacancy migration energy is reported as 0.82 eV, and the formation energy and volumes as 1.4 eV and $0.24b^3$, respectively [224]; given these larger barriers, it is unlikely that they contribute significantly to the experimentally observed behavior. On the other hand, surface self-diffusion has a comparable energy to what we measure on the order 0.031 eV for {111} Pd surface and is a process consistent with the small activation volume measured. Additionally, simulations of dislocation nucleation at surface steps have shown that the activation parameters can change significantly in the presence of such defects, which could possibly play a role in the nucleation response in Pd [110,225,226]. However, their role hinges on the configuration of these flaws relative to the applied stress and other defects. For instance, simulations of kinks on existing surface steps were shown to not influence the elastic limit in Al [225]. Additionally, the computed nucleation rate prefactor or effective attempt frequency $N\upsilon_0$ of 0.065 s^{-1} can be compared to time scales for nucleation measured in our experiments. The load-hold test performed and shown in Figure 3-1(b) represents a case where a fixed load is applied below the fracture strength and nucleation is assisted by thermal fluctuations and time. These experiments suggest a nucleation expectation time of 24 s at 3.8 GPa, which agrees with our model's prediction of the order of 10 s. Similar to other experimental studies [222,223], our computed nucleation rate prefactors are approximately nineteen orders of magnitude different from a value that can be estimated assuming the truncated rhombic cross-sectional geometry of the NW and an attempt

frequency on the order of the Debye frequency (5.7×10^{12} s^{-1}). This implies that even a single viable activation site on the surface of our Pd NW ($N = 1$) would possess an attempt frequency of the order of 0.01 s^{-1}. While there have been studies demonstrating a different vibrational frequency of surface atoms from the bulk [143,227], these manifest primarily in small changes of the surface Debye temperature, which alone cannot account for such a large discrepancy. Given that dislocation nucleation does not involve single atoms but rather a collective group, the frequency of individual atomic vibrations may not be a suitable or physically sensible attempt frequency [103].

The probabilistic nature of surface dislocation nucleation instantly emerges when comparing our full data set to computed temperature-dependent probability distribution functions (PDF). The PDF at each temperature is shown in Figure 4-5 and normalized by its maximum probability to highlight the trajectory of σ_c over temperature. Thus, each vertical slice of Figure 4-5 represents the probability distribution at a given temperature, which collapses to a deterministic value in the athermal limit. We compare our data to both cases of strong ($\alpha = 4$) and weak ($\alpha = 1$) stress dependence of the activation energy, whose calculated barrier parameters are presented in Table 4-1. Both models capture the strong temperature dependence of the mean nucleation strength, and more remarkably, of the non-monotonic scatter in probable nucleation strengths observed in experiment. Contour lines indicating the 5th and 95th percentile nucleation strength at each temperature show that the influence of α is most evident at low temperatures, particularly in the athermal limit. We note that the activation parameters deduced from our study and calculated for both values of α, most notably the kinetic prefactor $N\nu_0$, are still below the

values obtained in computational studies. The experimental values of Nv_0 remain only a few orders of magnitude higher than the applied strain rate, so even in the absence of a finite energy barrier (e.g. $T < 100K$, $\sigma > \sigma_{ath}$) nucleation is kinetically limited by the attempt frequency and thus not necessarily instantaneous.
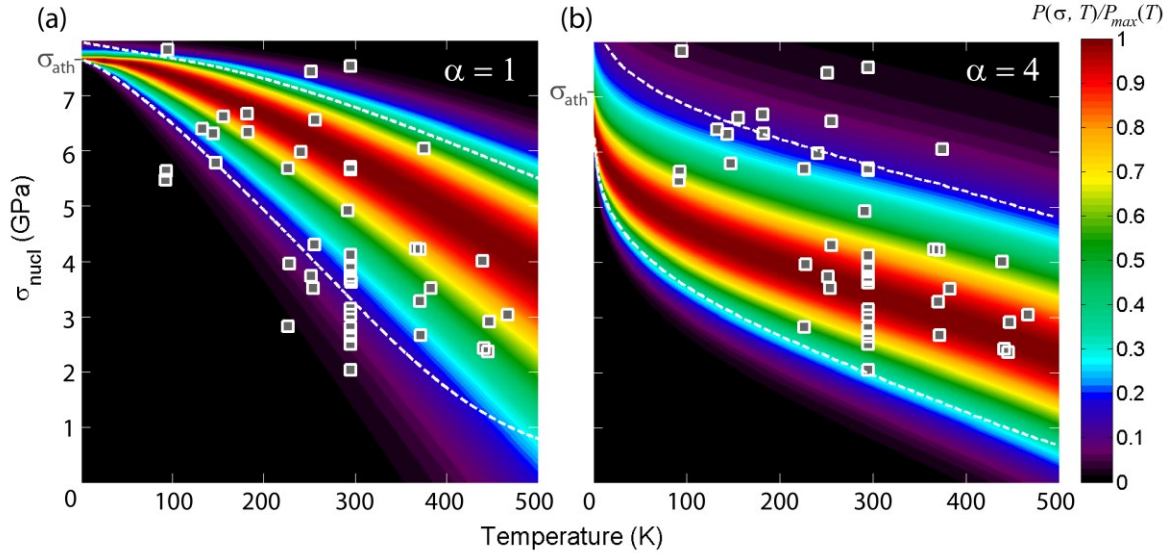
Figure 4-5 The normalized PDF maps for (a) $\alpha = 1$ and (b) $\alpha = 4$ are overlaid with measured nucleation stress (gray squares) at strain rates on the order of 10^{-4} s^{-1} (data points same as in Figure 4-4(c)). The respective values for σ_{ath} are indicated on the vertical axes. Probability values $P(\sigma,T)$ are normalized with respect to the maximum probability at each temperature $P_{max}(T)$. The dashed contour lines represent the 5th (lower) and 95th (upper) percentile nucleation stresses.

Table 4-1 Comparison of activation parameters obtained for different stress dependences of the activation energy.

	$\alpha = 1$	$\alpha = 4$
σ_{ath} (GPa)	7.46	7.08
σ_c at $T = 295K$ (GPa)	5.85	3.44
ΔG_{act} (eV) ($T = 295K$, $\sigma = \sigma_c$)	0.048	0.016
Ω (b^3) ($T = 295K$, $\sigma = \sigma_c$)	0.23	0.13
Nv_0 (s^{-1})	0.47	0.065

Statistically speaking, our experiments demonstrate better agreement with $\alpha = 4$, with about 90% of the measured events falling within the contoured envelope (Figure 4-5(b)). However, the agreement between the calculated temperature dependence of σ_c and the experimental results at low temperature suggest that an α closer to unity represents the physical obstacles to dislocation nucleation more accurately. The difference between the two cases is most pronounced at low temperatures, hence the agreement with the experimental data may be temperature-dependent. We provide a rough comparison by averaging the measured strengths within a given temperature window. As shown in Fig. 5, while the magnitude of the difference between each case and the experimental averages is similar, the agreement varies with temperature: at lower temperatures $\alpha = 1$ agrees better with the data whereas $\alpha = 4$ better models the higher temperature behavior. Since it is within the low temperature regime approaching 0K where the two models are most distinguishable, it is there where experiments can best inform the stress dependence of the activation energy. A similar observation has been noted in simulations of FCC crystals of varying geometries, which effectively change the "shape" of the obstacle that must be overcome [225]. Taken as a whole, this suggests that further measurements at ultralow temperatures would be a promising avenue to gain additional insight to the details of surface nucleation.
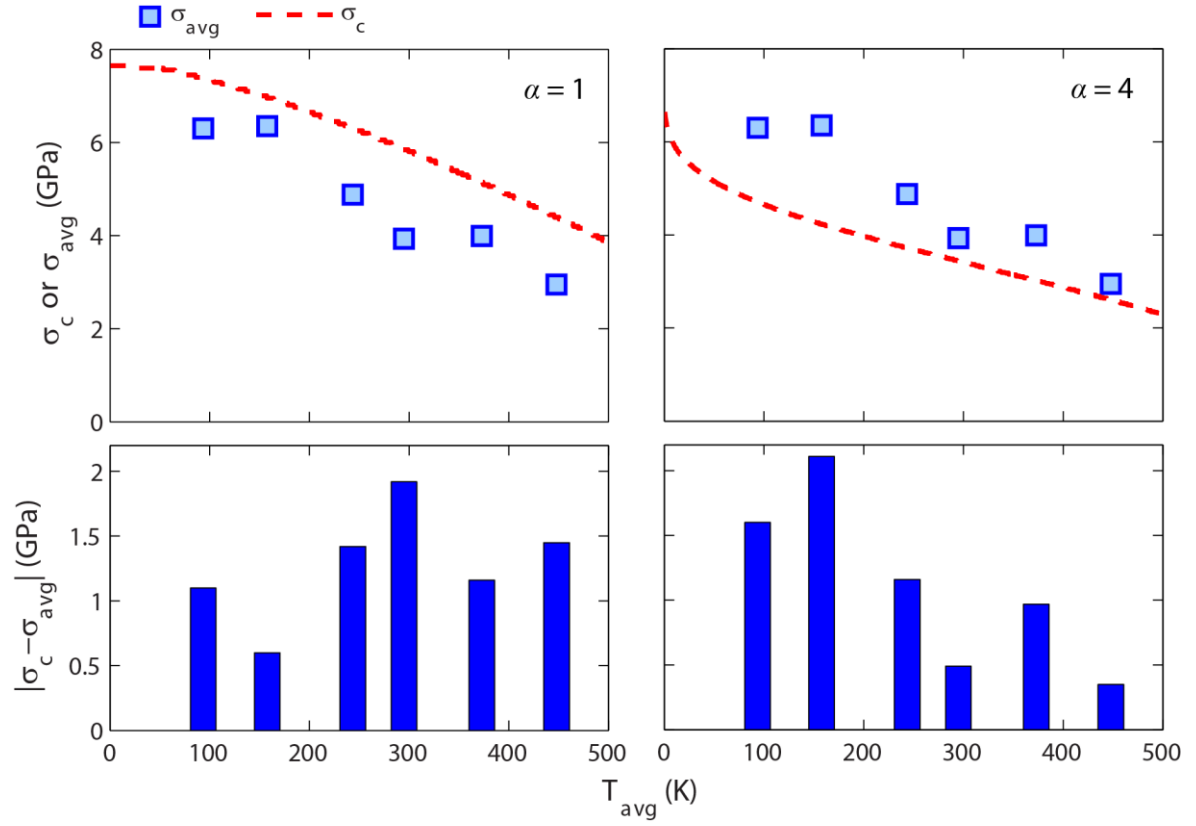
Figure 4-6 Comparison between experimental mean strength σ_{avg} and calculated most probable strength σ_c. T_{avg} represents the average temperature for each temperature window over which σ_{avg} was calculated. The lower bar graphs show the difference between experiment and model at each T_{avg}.

5   Further Discussion of Theoretical Model and Experimental Results

In the last chapter we presented experiments and results on the barriers to dislocation nucleation in defect-free Pd NWs.   Key assumptions were employed to develop an analytical model to not only capture the mean strength but also scatter in the experiments. We discuss these further in detail to highlight on their significance in our analysis as well as address discrepancies between our results and those from previous theoretical studies.   Additionally, we address a number of open questions regarding different characteristics and responses of the Pd NW samples tested.

5.1   Thermal Activation Framework

While many theoretical and computational studies have focused on quantifying the activation energy and strength for dislocation in FCC single crystals [27,28,110,111,143,185,228], there remains limited literature addressing some of the significant parameters and assumptions that enter into the nucleation rate, the starting point for investigating thermally activated dislocation nucleation. Combining Eq. 4-1 and Eq. 4-2, the full expression of the rate for dislocation nucleation in a defect-free nanowire is:

$$\upsilon(\sigma, T) = N\upsilon_0 \exp\left(\Delta U_{act}\left(1 - \frac{T}{T_m}\right)\left(1 - \frac{\sigma}{\sigma_{ath}}\right)^\alpha\right)$$ **Eq. 5-1**

Upon deriving a tractable model to apply directly to our experiments in Chapter 4, our starting point required making assumptions about the temperature dependence scaling by T_m, and the stress dependence of the activation energy α. Additionally, at the end of our analysis we found that among the results we obtained, the largest discrepancy between literature and experiment laid in the attempt frequency υ_0, with a difference of about nineteen orders of magnitude. Here we aim to address the role of these parameters in the physics of dislocation nucleation, including possible origins of discrepancies where applicable, as well as how they could apply to our analysis of dislocation nucleation barriers in our experiments.

5.1.1   *Stress Dependence of the Activation Energy*

According to Aubry *et al.*, for a crystal under constant stress σ, a linear relationship can be readily assumed from the energy of a nucleating dislocation:

$$E(b_p, \sigma) = 2\pi R \frac{\mu b_p^2}{8\pi}\left[\frac{2-v}{1-v}\left(\ln\frac{8R}{r_c} - 2\right) + \frac{1}{2}\right] + A\gamma_{SF} - Ab_p\sigma$$ **Eq. 5-2**

Where R is the radius of the nucleating loop, b_p is the associated partial burgers vector, r_c is the dislocation core radius, v is Poisson's ratio, γ_{SF} is the stacking fault energy, A is the area of the slipped region, and σ is the applied stress [228]. The first term represents the line energy, the second is the energy from the stacking fault area, and the third term is the

99

work done by the applied stress, from which the linear stress dependence arises. While this model captures the main elements of homogeneous nucleation, it was found to severely overestimate the required energy: not only did the generalized stacking fault (GSF) curve need to be taken into account, but also the stress-dependence of the GSF curve due to the high stresses required [28,228]. Thus, the analytical model is modified to reflect this additional stress-dependence [228]:

$$E\left(b_f,\sigma\right)=2\pi R\frac{\mu b_f^2}{8\pi}\left[\frac{2-v}{1-v}\left(\ln\frac{8R}{r_c}-2\right)+\frac{1}{2}\right]$$
$$+A\left(\gamma_{GSF}\left(\sigma,u_0+b_f\right)-\gamma_{GSF}\left(\sigma,u_0\right)\right)-Ab_f\sigma$$

Eq. 5-3

Where b_f is the fractional burgers vector of the nucleating partial dislocation. For most earlier experimental evaluations of the activation barriers to dislocation nucleation under nanoindentation, the value of α has been assumed to be 1 [162,229,230]. While Eq. 5-3 indicates that the relationship between the nucleating loop energy E and σ is not exactly linear owing to the additional stress dependence of the GSF curve, predictions from chain-of-states calculations for homogeneous nucleation in several FCC metals, which yield α values between 1 to 2 [28].

On the other hand, chain-of-states calculations have also indicated that there may be extra factors influencing the heterogeneous nucleation from surfaces. The stress-dependent activation energies determined by Jennings *et al.* for different geometries and surface faceting of Au nanowires require α of at least 2 to sufficiently agree with the data [28]. Likewise, calculations from Zhu *et al.* for corner nucleation in a Cu nanowire determined $\alpha = 4.1$ [110]. Unlike homogeneous deformation in bulk, dislocation

nucleation in nanowires are strongly influenced by surface properties and features. Atomistic studies on various single crystal geometries collectively show that both external geometry and local surface features (e.g. atomic steps) can substantially modify the stress dependence of the activation energy [143,225,231]. Formation of surface steps during nucleation requires taking into account the surface energy γ, which like the GSF energy may be significantly stress-dependent [28]. Furthermore, obstacles involved in surface nucleation such as image stresses will affect the necessary forces to enlarge the nucleating loop to its critical configuration. Jennings *et al.* had managed to develop an analytical model to capture many of these elements and was able to successfully apply it to the measured strengths in Au nanowhiskers, which highlights the complexity required to accurately capture the process of heterogeneous nucleation.

One of the current questions now is to understand how the presence of flaws can change the stress or strain dependence. This can be particularly crucial for comparing simulations with experiments, as often the scatter in the latter is attributed to the presence of surface defects. Simulations by Brochard *et al.* and Hara *et al.* on monatomic film steps have shown that not only is the critical strain at which nucleation occurs dramatically affected, but also the entire activation energy profile as a function of that strain [188,232]. Their work in fact points to a possible strategy to understanding and possibly predicting the stress dependence

Our work in the previous chapter has shown that by measuring at low temperatures, the stress dependence can be estimated. More precise evaluation of α could

be performed iteratively, and such information could be extremely useful in informing more directly on the geometric contributions to dislocation nucleation.

5.1.2   Temperature Dependence of the Activation Energy

As mentioned in the previous chapter, the temperature dependence in the expression for activation energy is related to the significance of activation entropy. Nudged elastic band (NEB) calculations for determining the nucleation energy only address the energy landscape at 0 K [110,233,234], such that the role of entropy is usually ignore, which can lead to severe underestimation of the nucleation rate at finite temperature by orders of magnitude. In extrapolating their values of activation energy to apply to room temperature experiments, Zhu *et al.* used the factor $(1 - T / T_m)$, where T_m is the surface melting temperature (Eq. 5-1) [110], although some authors have provided alternative interpretations of the temperature dependence. For example Warner and Curtin were able to capture the activation energies by considering temperature-dependent material properties and directly attributed the substantial changes in activation energy to the dependences of the shear modulus and unstable stacking fault energy [157]. In particular, they identified that the effect of temperature not only rescaled but also translated the activation energies as a function of stress. This is shown schematically in Figure 5-1, where the significance of the shift becomes clear, as it also changes the stress at which the energy barrier disappears with temperature.
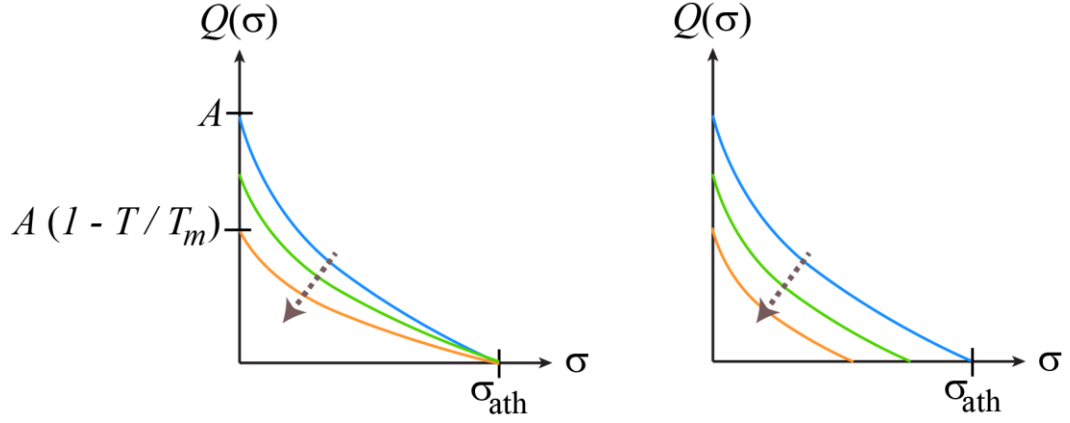
Figure 5-1 Schematic for two cases of temperature dependence on the activation energy $Q(\sigma)$. The case on the left represents the relationship expressed in Eq. 5-1 and the case on the right shows the scale and shift found in Warner and Curtin's study (Ref. [157]). The arrows indicate increasing temperature.

Ryu *et al.* had also looked at the temperature-dependence using umbrella sampling and determined very significant entropy during both homogeneous and heterogeneous dislocation nucleation in Cu [111,112]. For example, heterogeneous nucleation in a nanowire under constant stress and strain, the respective entropies were $\Delta S(\sigma) = 17k_B$ and $\Delta S(\varepsilon) = 9k_B$, respectively [112], which can contribute a difference to υ of at least four orders of magnitude. These large contributions arise from anharmonic effects: under constant strain, thermal expansion enables easier shearing between adjacent planes; additionally, under constant stress the associated strain increases during nucleation owing to thermal softening [111]. Using the entropy to determine when the activation energy barrier for dislocation nucleation disappears, the authors could determine the associated temperature T_m. While they showed for nucleation under constant strain (for $\Delta S(\varepsilon) = 9k_B$) that even the critical T_m for heterogeneous nucleation

(2450 K) was even above the bulk melting temperature of copper (1358 K), which they asserted was consistent with the idea that only thermal expansion contributed to the lower value of $\Delta S(\varepsilon)$ [111,112].

Nonetheless, the unique influence of the surface in dislocation nucleation in nanowires and other nanostructures underlines the importance of accounting for the disorder in the surface and how it could possibly promote nucleation at higher temperatures. Even though the critical configuration for heterogeneous nucleation is attained in the bulk-like interior, its ease of formation and final configuration is heavily shaped by the surface structure [144,216,235]. In their MD study of compression in Au nanopillars, Rabkin and Srolovitz showed that the anharmonicity at the surface determined the yield criterion, i.e. change in the temperature dependence of the yield strength was directly tied to the thermal vibrations of surface atoms [143]. Specifically the temperature dependence of the mean square vibrational amplitude of loosely bound atoms was found to be linear, which indicates very large anharmonicity of the atomic vibrations [227]. This was consistent with the temperature dependence of strength in square pillars and attributed to the presence of sharp corners possessing where the miscoordination is much higher than within a surface facet; on the other hand, the yield strength in circular pillars varied parabolically with temperature, which is consistent with the temperature-dependence of harmonically vibrating surface atoms.

Considering the potentially strong influence of surface anharmonicity due to the faceted geometry of the Pd NWs, it seems reasonable (and analytically feasible) to scale the activation energy directly with T_m. However, given that the above study by Rabkin

and Srolovitz [143] along with work from others [33,236] have asserted that it is the most peripheral atoms, i.e. those at edges, corners, and the ends of nanowires, that govern the critical strength, it is therefore important to consider more carefully the selection of T_m for nanowires and other corner-dominated geometries. Unlike in bulk crystals or even flat surfaces, the source of the nucleation dislocation can be narrowed down to a set of highly preferential, peripheral sites. Thus, it may be worthwhile for future studies, theoretical or otherwise, to study more thoroughly anharmonicity at the very corners.

5.1.3 Attempt Frequency

For many thermally activated processes in crystals, the attempt frequency is assumed to be on the order of or identical to the Debye frequency [103,104,112], which represents the highest energy mode of vibrations in the atomic lattice. This implies that the nucleation of a dislocation is initiated by the attempt of a single atom to move away from its equilibrium position in the lattice at finite temperature. That the vibration and detachment of a single atom is sufficient to attain the critical configuration for nucleation is not the picture that is supported by atomistic simulations. Several such studies have clearly shown that the maximum free energy corresponds to a critical radius or loop [24,28,110,185], which requires the collective displacement of several atoms. Moreover, the direct correlation with the Debye frequency then brings up the question of what happens to the attempt frequency below the Debye temperature.

The direct interpretation of v_0 as the Debye frequency has been brought into question. Ryu *et al.* adopt a different approach by defining the attempt frequency as the product of the molecular attachment frequency (from MD simulations) and the Zeldovich factor, which accounts for backward jumps [111,112]. This frequency was found to be a slowly varying function of σ and T and therefore assumed constant for the temperature range of interest (0 K to 500 K). While their values for simulation nucleation in Cu was found to be on the order of the Debye frequency (10^{13} s^{-1}), they determined a slightly lower frequency value for heterogeneous nucleation than homogeneous nucleation, attributed to fewer atoms being required to form a critical loop in the former case [111].

A more physically reasonable value can be estimated provided by specifying the upper and lower bounds for the frequency factor. At its maximum it is the atomic vibration, but as the critical configuration corresponds to the formation of a loop, the collective behavior of adjacent atoms must also be taken into account [103]. For a dislocation line overcoming obstacles spaced length λ away, the dislocation ground frequency v_g is:

$$v_g = v_D \frac{b}{4\lambda}$$

Eq. 5-4

Where b is the burgers vector. For the formation of a critical surface loop in a nanowire, it may be reasonable to assume that λ is twice the critical radius, which correlates roughly to the distance between the ends, to provide an order of magnitude estimate of v_g. When applied to the nucleation of a dislocation loop with an expected critical radius of about $10b_p$, the ground frequency can be lowered by nearly two orders of magnitude.

106

Additionally, taking into account the lower Debye temperature of surface atoms [227] can scale the ground frequency down further.

Nonetheless, this difference still does not span the great difference between theoretical and computational approaches and the limited experimental work that exists. Schuh *et al.*, for example measured an attempt frequency about 10 orders of magnitude lower than theoretically predicted for homogeneous nucleation in single crystal Pt [222,230]. Our work on Pd nanowhiskers reveal a frequency prefactor on the order of 0.01 s^{-1}, a discrepancy of about nineteen orders of magnitude. This prefactor is consistent with the expectation time measured from the load-hold experiment in Section 3.1 and discussed in Section 4.6, as well as on par with expectation times measured in load-hold experiments performed via nanoindentation [223,237,238]. In contrast, thermal activation parameters from the simulations performed by Zhu *et al.* yield an expectation time on the order of 10^{-10} s for experimental conditions [110].

Zuo *et al.* proposed that the finite duration required for incipient plasticity is consistent with a thermally activated process; moreover, they find using MD simulations of a single crystal under shear that only hot spots, clusters of atoms with displacements above a threshold fraction of the lattice parameter, have the potential to form into dislocation nuclei [223,239]. The mean relative displacement of atoms is directly proportional to a normalized displacement value x_0:

$$x_0 = A(T)\gamma + B(T) \hspace{3cm} \textbf{Eq. 5-5}$$

Where $A(T)$ and $B(T)$ are functions of temperature and γ is the applied shear strain [239]. The first term $A\gamma$ contributes affine displacements due to the applied deformation, and the latter component B represents the contribution of thermally agitated, random displacements. Therefore, a more accurate attempt frequency and thus nucleation rate prefactor would represent the frequency of hot spot appearances (i.e. multiple adjacent atoms where x_0 exceeds some threshold value), which may depend on both strain (or stress) and temperature. This would lead to an effective attempt frequency orders of magnitude lower than that proposed by other theoretical studies, although how it translates to experimental conditions is still not clear.

A final possible source of discrepancy between theory and experiment is the experiment itself, which involves testing instruments which may possess their own vibrational frequency. The MEMS-based tensile testing stage used in the current study on Pd NWs consists effectively of two beam structures, which may vibrate freely in the axial and transverse directions (towards and away from substrate) [240,241]. Looking just at bending (transverse) vibrations, simply supported cantilevers of comparable dimensions to the load cell and actuator grip beams would vibrate at frequencies on the order of 10-100 kHz. While simply substituting in the mechanical frequency as $N\nu_0$ cannot fully account for the difference between our experimental results and theory, it could jointly contribute to other effects, such as by adding an oscillatory component to the affine component of x_0 and thus affecting the frequency of hot spot formation (Eq. 5-5). In order to fully evaluate this effect, one can rewrite x_0 with a time dependence:

108

$$x_0(t) = \varepsilon_{max} \cos(\omega_\varepsilon t) + a_{instr}(\varepsilon)\cos(\omega_{instr}t) + x_{vib}\cos(\omega_{vib}t) \quad \textbf{Eq. 5-6}$$

Here, x_{vib} is the amplitude of atomic vibrations, a_{instr} is the amplitude of the vibrations of the testing instrument (ignoring effects due to the applied strain via the load), ε_{max} is the maximum strain achieved during a loading cycle, and ω_ε, ω_{instr}, and ω_{vib} are the angular frequencies ($2\pi v$) strain rate, instrument, and atomic vibration. The effect of instrumental vibrations could potentially be evaluated either from existing literature on experiments performed with different testing stages on similar material systems or by performing tensile tests on the current specimens using other stages.

5.2 Influence of Axial Boundary on Plastic Deformation

The axial boundaries found in several of the NWs grown on Al_2O_3 appear to be stacking faults that run across the width of the NW. The exact configuration is not yet known, including how the presence of this structure might also change the external faceting. Based on the splitting of the $\{1\,\bar{1}\,1\}$ peaks in the SAED pattern (Figure 5-2(a)), one possible configuration consists of a stacking fault running along the NW length (Figure 5-2(b)). In the simplest case, this could affect the total number of viable nucleation sites N, which is predicted to have a weak impact on the critical nucleation strength [110]. However, such internal boundaries can also potentially introduce lower energy barrier sites that promote nucleation at lower stresses [236]. Additionally, coherent planar boundaries can act as barriers to dislocation slip [84,242,243], requiring very high stresses comparable to the nucleation strength [236,244].

Various configurations of planar defects with zero resolved shear stress have been shown to have significant impact on the deformation behavior of otherwise defect-free nanowires. For example, axially five-fold twinned or "pentatwinned" FCC are found to exhibit higher elastic stiffness and yield strength but reduces ductility compared to single crystal nanowires [68,245]. These effects have been attributed to a combination of the residual stresses required to form the pentatwinned structure [246] and the pinning of dislocations at the twin boundaries. In another study looking at twin boundaries oriented orthogonal to the nanowire axis, Zhang and Huang found that these boundaries can strengthen or soften nanowires depending on their spacing along the length as well as the nanowire cross section [236]. More closely spaced boundaries will require higher stresses to produce yield even after a dislocation is nucleated. However, since the nucleation strength is generally higher in circular than in square geometries (see also 5.1.2), dislocations in circular nanowires often nucleate at twin boundary sites on the surface but still require higher stresses to do so, thus readily traverse twin boundaries in their path [236].
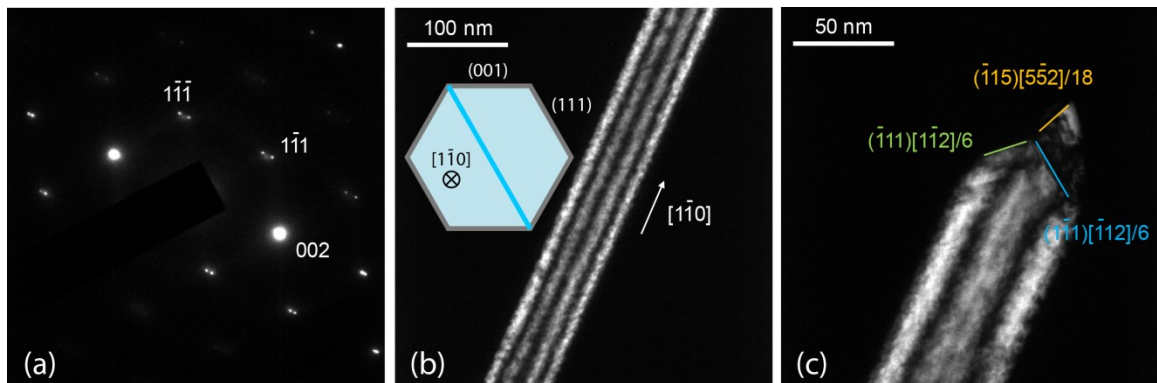
Figure 5-2 Pd NW with axial stacking fault. (a) SAED of the [110] zone axis. (b) Dark field imaging ((002) spot) of undeformed NW with schematic of proposed structure. (b)

Fracture morphology of the same Pd NW after tensile testing. *Courtesy of Dr. Mo-Rigen He.*

To gain a preliminary understanding these defects may have specifically on dislocation nucleation in Pd NWs, in situ TEM tensile tests were performed on these samples using the PTP setup. Much like tests on defect-free specimens, the same remained elastic until localized nucleation activity produced a quasi-brittle response at high strengths. The nucleation strengths are comparable to those measured in defect-free Pd NWs (Appendix chapter 7.2) and do not strongly impact the scatter in our measurements. Moreover, as shown in Figure 5-2 Pd NW with axial stacking fault. (a) SAED of the [110] zone axis. (b) Dark field imaging ((002) spot) of undeformed NW with schematic of proposed structure. (b) Fracture morphology of the same Pd NW after tensile testing.(c) the boundary remains within the NW after deformation and the fracture morphology indicates twinning behavior consistent with that observed in defect-free materials (section 4.1). These preliminary results suggest that for the current testing and sample geometries, the impact these defects have on the measurement of mechanical properties in this system are relatively weak.

5.3 Size-dependence Arising from Surface Stress-induced Relaxations

In Chapter 4, the scatter in the benchmark points overshadowed potential contributions from other factors such as strain rate and even the nucleation strength and potentially contributed to the large discrepancy in the thermal activation barriers when

compared to theoretical studies. Our goal here is to find a way to take the size dependence into account and develop a size-independent strength criterion by which to analyze the data. Utilizing the size dependence power law $\sigma = d^{-m}$ to evaluate the size dependence of σ_{nucl} found in our Pd NW experiments, we find that $m = 0.589$ (Figure 5-3), which is similar to the power laws characterizing other FCC single crystal structures including some of the studies on other defect-free nanowhisker systems [39,138,139]; moreover, the degree of scatter is also very similar. However, as has been addressed in the computational literature, the presence of size-dependent strength should be indicative of surface stress effects [28,185], which has been observed and confirmed in Chapter 2. Since the power law is phenomenological, we attempt to make sense of the size dependence by taking another approach to surface stress contributions.
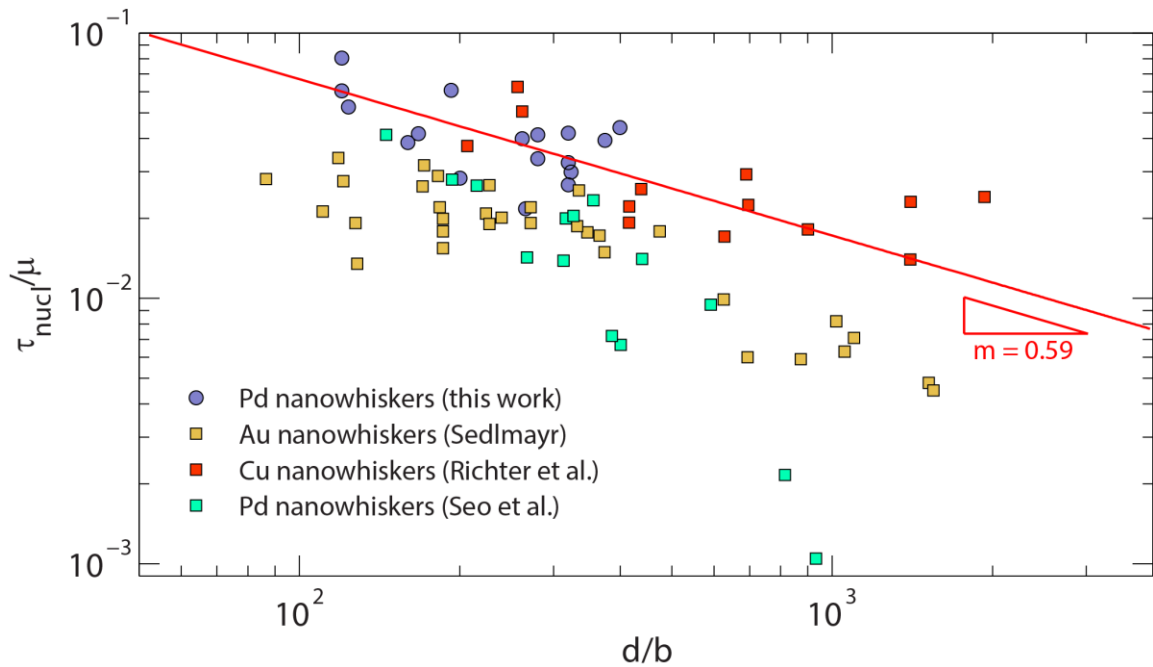
Figure 5-3 Power-law fitting of size-dependence of σ_{nucl} measured in benchmark samples. Strength measured from other nanowhisker tests in the literature are included for comparison (Refs. [39,139,141]).

112

In Chapter 2, we attempted to address the relationship between the elastic and inelastic strength. The low-strain and higher-order elastic moduli exhibited clear size dependence attributed to the increasing influence of surface stresses at smaller diameters. A simple model to relate the low-strain modulus E_{NW} to the nonlinearity of the bulk Pd along [110] led to estimations of significant – and in some cases unrealistic – surface stress-induced relaxations with non-negligible impact on the bulk strength. Existing models looking into the size-dependence of FCC nanowires have widely identified surface stresses as the primary mechanism [24,28,185]; however surface stress effects are not expect to be significant for diameter ranges in excess of about 10-15 nm. Nonetheless, the current work on Pd NWs is not the only one to measure large deviations from bulk behavior for diameters as large as 60 nm (section 1.2). Whereas earlier we used the elastic moduli to determine the relaxation strain and hence the effect on σ_{nucl}, we now use σ_{nucl} in order to determine the requisite surface stress.

Diao *et al.* proposed a continuum approximation of the internal stresses induced by surface stress τ_0 in a NW prior to deformation [25]:

$$\sigma_{\text{int}} = \begin{bmatrix} \sigma_\tau & 0 & 0 \\ 0 & \dfrac{\sigma_\tau}{2} & 0 \\ 0 & 0 & \dfrac{\sigma_\tau}{2} \end{bmatrix}$$

Eq. 5-7

Where

$$\sigma_\tau = -\frac{4\tau_0}{d} \qquad\qquad\qquad \textbf{Eq. 5-8}$$

Consequently, upon yielding, the internal stress in the bulk like core in the axial direction becomes $\sigma_\tau + \sigma_{nucl}$, where σ_{nucl} is the applied stress needed to nucleate the first partial. In other words, experimental strength measurements can be modeled according to

$$\sigma_{nucl} = \sigma_{n,0} - \sigma_\tau \qquad\qquad\qquad \textbf{Eq. 5-9}$$

Where $\sigma_{n,0}$ is nucleation stress necessary to nucleate a dislocation in the absence of surface stress. For our Pd NWs results, this yields $\sigma_{n,0} = 1.702$ GPa and $\sigma_\tau = 131$ GPa or $\tau_0 = 32.8$ J/m^2, which is an order of magnitude above realistic values for the surface stress [247].
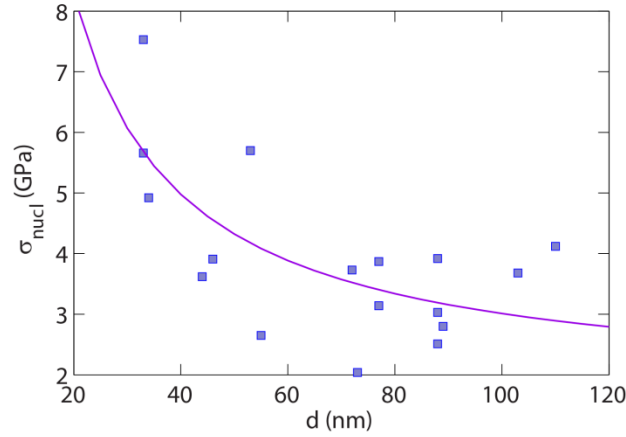
Figure 5-4 Fitting of experimentally measured σ_{nucl} in Pd NWs to surface stress-induced size dependence model in Eq. 5-9.

By incorporating additional elements into the simple model above, it may be possible to develop a more comprehensive size effect predictor with concrete physical grounding in a

simple model. The current value of the surface stress is independent of strain and should ideally be expanded to reflect the contributions of surface stiffness on the deformation [30]. Moreover, additional contributions to the total strain energy should be considered: transverse relaxations in the bulk as indicated in Eq. 5-7 may be included as well as the effects of corners are ignored, both of which impose residual elastic strain on the volume and become significant as the total bulk volume decreases [26,63,248].

5.4 Surface Coatings: Influence of Hydrocarbon Layer

Hydrocarbon contamination of the pristine NW surfaces during electron microscopy imaging results from two primary sources: interaction of the electron beam with organic molecules in the chamber [249,250], and the organometallic gas precursor used to create the Pt-EBID contacts necessary for mechanical testing. The latter can occur from delocalization of the primary electron beam, decomposition of the precursor gas owing to secondary electron scattering events away from the primary beam, or diffusion of the deposited species along the NW. Any influence of such coatings on the measured mechanical response could be a result of either load bearing being borne by the coating or influencing the surface condition and thus the barrier for defect nucleation.

While the resulting coating does not chemically alter the interior of the Pd NWs, its effects on the surface energy and surface atomic coordination are still unknown. We note that all NWs tested have some nominal coating; thus, the surface condition should be similar for all experiments. Even in bulk metals, where the surface-to-volume ratio is much lower, coatings with surface-active media have been shown to significantly alter

115

the resulting strength as well as embrittle otherwise highly ductile materials [251,252]. Given the high surface-to-volume ratio for our specimens and the importance of surface nucleation for our testing geometry, it is crucial to evaluate how modifications to the surface can affect mechanisms for plasticity and elasticity.

Pd is well known for its ability to catalyze reactions on its surface. Moreover, Pd nanoparticles have been identified more chemically active than single crystal surfaces; owing to its small dimensions, access to subsurface hydrogen, which is key to many hydrogenation reactions, is much easier [253]. The high affinity of the surfaces of Pd and other similar noble metals to attract hydrocarbon species is potentially problematic in environments such as an SEM. Hydrocarbons can readily break down in with plasma, ion beam, and electron beam radiation to form various carbon coatings [254–257]. Some forms of carbon coating such as diamondlike carbon (DLC) possess excellent mechanical properties owing to significant sp^3 bonding known [255,258,259]. However, it is highly unlikely that the use of electron beam energies on the order of 3-5 keV typical of our manipulation process will produce DLC. Additionally, our experiments with producing thick hydrocarbon layers failed to show changes in apparent NW stiffness even with large increases in the volume fraction of the coating (Section 7.2). Therefore, with respect to our measurements of mechanical properties in Pd NWs, we are primarily concerned with possible reduction in the surface energy that may reduce the critical stress needed to create surface ledges during the nucleation process. As all the tested Pd NW specimens are manipulated using the same methods and covered by this coating, the surface energy reduction from the coating is less likely to affect the scatter and will be more influential

116

on the mean strength, i.e. determining the σ_{ath}. Our current value for $\sigma_{ath} = 7.08$ GPa is about $\mu/13$, which is within the estimated range of the theoretical strength. From this demonstration of such high strength, it seems unlikely that the coating has a great influence on the measured strength.

6   Summary and Future Directions

Understanding the mechanical behavior of materials at reduced length scales is key to not only exploiting novel properties that are exclusively attainable in small volumes but also crucial to successful development of new technologies that employ nanoscale building blocks. Modelling studies have been indispensable for providing insight into the mechanisms governing deformation; however, direct comparison with real material systems is often quite challenging due to sample quality as well as the availability of appropriate experimental tools. We have been able to overcome many of these challenges for evaluating deformation mechanisms in FCC metals by employing defect-scarce Pd NWs and developing a novel tensile testing setup incorporating precise temperature control. Through systematically executed experiments on a model nanowhiskers system, we have been able to directly quantify the distinct mechanical properties as well as address in detail the mechanisms responsible for elastic and plastic deformation in nanoscale FCC single crystals.

We evaluated the nonlinear elasticity in <110> Pd NWs attributed to lattice anharmonicity characterized by the nonlinearity parameter δ. This quantity, and likewise its strain-expanded counterpart b, show no size-dependence, while the apparent second- and third- order elastic moduli E and D vary with size. The changes in E are attributed to large compressive strains along the axis of the core, which balance the tensile surface stresses. Consequently, the measured E represents the instantaneous slope of the bulk

118

stress-strain curve for the corresponding applied strain, highlighting the importance of using higher-order (post-Hookean) elastic behavior when describing the effects of surface stresses. The measured correlation between D and E also suggests that the size-dependence of the third-order elastic modulus is also related to the nonlinear elastic response of the bulk-like core. Irrespective of the difference in length scales, the measured nonlinearity of Pd is in general agreement with both atomistic and experimental studies on bulk specimens of other FCC transition metals. These results provide a novel method for characterizing size-independent bulk properties, not accessible by conventional methods, via size-dependent elastic behavior in defect-free, high-strength nanostructures. The implications of our results extend beyond material elasticity, as the nature of interatomic bonding and dynamics affect mechanical, thermal, electronic, and physical properties of materials.

We have also investigated the dislocation nucleation-mediated plastic deformation for uniformly strained Pd NWs. The results of Chapter 4 provide new insight to a class of defects that affect material properties and device performance in a host of technological sectors and pave the way for rational operation and lifetime predictions. By systematically performing tensile testing at a range of temperatures, it was found that the plastic deformation is mediated by surface dislocation nucleation at ultrahigh stresses at the theoretical limit of strength and representing the highest ever measured in an FCC metal. The large scatter in nucleation strengths observed for different testing conditions is attributed to the stochastic nature of our thermally activated process. While no clear size or strain rate dependence is detectable beyond the observed scatter, the results

119

uncover strong temperature dependence well in excess of what is observed in bulk FCC metals. The presented model for extracting the energetic and kinetic parameters governing the observed nucleation process takes into account the temperature and stress dependence of the activation energy and volume. Finally, using parameters that capture the statistical distribution of temperature-dependent strengths, one can develop a full statistical model that captures both the mean nucleation strength and scatter measured across the entire tested temperature range. These results can ultimately be used to predict the nucleation behavior under extreme conditions and inform probabilistic models and device design strategies employing nanoscale materials.

This work has shown that the processes responsible for deformation in small volumes are distinct from bulk and even micron-sized specimens due to the absence of pre-existing carriers of plasticity and increasingly important surface contributions. Specifically the quantification of both the elastic and plastic behavior suggests that the their deviations from bulk response and size-dependent properties possess a common origin, which is not the case at larger length scales. There remain several open questions regarding the observed behavior. Some of these areas, such as the role of various types of defects including internal boundaries, are currently being addressed in atomistic simulations conducted by Professor Erik Bitzek at the University of Erlangen. Additionally, there are a number of experimental avenues which can provide further insight into the observed mechanical behavior of Pd NWs.

The elastic moduli and the yield strengths have both shown size-dependent behavior, which was partly addressed in section 5.3. Experiments probing the internal

strain state in the Pd nanowhiskers would provide extremely valuable information about relaxation in the NW interior. We expect the changes to the internal stress state of the bulk-like core to be more complicated than the model proposed in Chapter 3 due to transverse relaxations and edge contributions; moreover, the results of this study could also potentially inform on barriers to incipient plastic deformation. This information could be obtained using a high-resolution strain measurement methods such as coherent X-ray diffraction (CXRD) [260–263]. This method has previously been used to successfully study strain fields induced from substrates and surface coatings of crystalline structures with dimensions comparable to the current NW samples [262,264]. In addition, the sensitivity of this technique to crystal defects such as dislocations would enable potential use to observe plastic events [260,261]. Collaborating with researchers from the Institut Matériaux Microélectronique Nanosciences de Provence, we have been able to develop an in situ tensile testing setup for CXRD by employing CINT tensile stages that have been thru-etched below the sample. This will allow us to perform diffraction experiments in transmission mode to characterize the strain as the NW is being deformed.

We also plan to further investigate the influence of surface modification on the nucleation behavior in FCC metals from two different directions. The first direction involves directly controlling the surface chemistry of the Pd NWs by coating with a known material. This can be done with a method such as atomic layer deposition (ALD), which coats surfaces through layer-by-layer deposition of chemical precursors. Ideally, the deposition would be done shortly after NW growth to avoid possible contamination of

121

the surface upon exposure to air or humidity. Currently we have successfully developed a routine to deposit 5nm layers of Al_2O_3 on the surface of Pd NWs to simulate a stiffer surface, and we can readily extend our study to include other materials of known mechanical properties. By controllably modifying the surface to change the strength and stress-dependence of obstacles to dislocation nucleation, we can more thoroughly address the role of surface quality and surface flaws.

The second experimental direction to address the influence of surface coatings is to avoid carbon contamination altogether. Manipulation of Pd NWs would be performed outside of the SEM using a probe station and a UV-curable adhesive would be used in lieu of Pt-EBID for gripping specimens for testing. Ideally, the surface of the sample could be imaged in the TEM to verify surface quality immediately following fracture; hence, rather than use the MEMS-based testing stage, which would require post-mortem manipulation of the sample, samples are mounted to a PTP device for easy direct transfer. A first attempt has been successfully made in the manipulation of Pd NWs to a PTP device. Given the common presence of hydrocarbon contamination for similar sample manipulation and testing setups, results from this specific investigation would be of widespread importance for many other experimental studies.

Finally, while our experiments have been concerned with introducing dislocations into a defect-free crystal, it would be interesting to consider ways to remove defects following nucleation and returning the crystal to a defect-free state. This seems a natural extension to the many experiments in micro- and nanopillars as well as other structures with pre-existing defects have demonstrated dislocation starvation as a strengthening

mechanism [119,124,125,211,265]. From our tensile testing results on Pd NWs, we have observed that the introduction of dislocations usually leads rapidly to fracture, with very little chance of arresting the process to remove the nucleated defects. On the other hand, hydrogen loading, either via gas [179,180] or electrochemical means [266,267], could potentially be used to controllably introduce dislocations into NWs, after which they are removed by the application of strain. If this concept can be brought to fruition, it could have implications not only for Pd but for other materials whose properties deteriorate in the presence of hydrogen, such as Fe and Ni [268–270]. For Pd specifically, this could be useful for developing novel Pd membrane structures for hydrogen filtration [170,172] or sensing [271–273] that can be "healed" with strain.

7 APPENDIX

7.1 Error Calculation for Elastic Constants

The primary sources of error originate from the diameter of the Pd NW samples and the noise in the digital image correlation (DIC). The cross-section of the Pd NW is a prismatic Wulff shape approximated as a circle with a diameter d. Several measurements (>10) were taken immediately after manipulation but before testing. The presented diameter values are averages and the associated error values are the standard deviations.

The accuracy of DIC is limited by the pixel resolution of the imaging technique. Tests performed in the optical microscope at a magnification of 1000x had a noise floor of 7 nm. Tests performed in the SEM at 40,000x magnification or higher had a noise floor of <2 nm. With a load cell compliance of 40 N/m, load noise floors are 300 and 80 nN for optical microscope and SEM tests, respectively (Figure 7-1). The noise in strain values is dependent on the gage length: for a typical 3 μm gage, the noise floors are 2×10^{-3} and 7×10^{-4} for optical microscope and SEM tests, respectively.
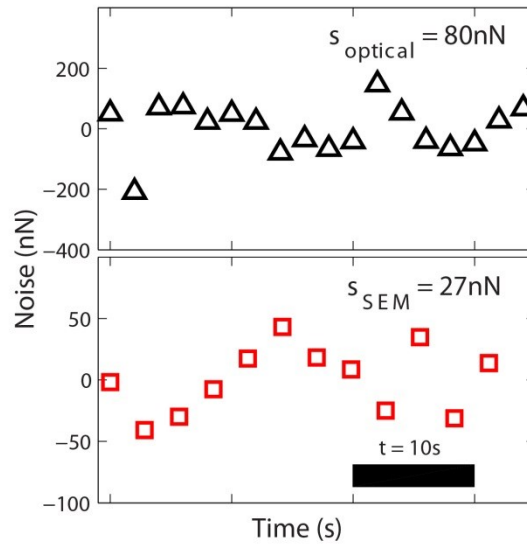
Figure 7-1 Sample load cell noise from optical microscope (above) and SEM (below) tests. The values *s* represent standard deviation values for the noise.

The expressions for error propagation were derived from two general formulas. The first formula calculates the uncertainty on a quantity q that is a product and quotient of other quantities, i.e. $q = \dfrac{r \times ... \times w}{t \times ... \times x}$:

$$\frac{\Delta q}{q} = \sqrt{\left(\frac{\Delta r}{r}\right)^2 + ... + \left(\frac{\Delta w}{w}\right)^2 + \left(\frac{\Delta t}{t}\right)^2 + ... + \left(\frac{\Delta x}{x}\right)^2} \qquad \textbf{Eq. 7-1}$$

If q is an arbitrary function of several variables and the associated errors are independent and random, then

$$q = \sqrt{\left(\frac{\partial q}{\partial r}\Delta r\right)^2 + ... + \left(\frac{\partial q}{\partial w}\Delta w\right)^2 + \left(\frac{\partial q}{\partial t}\Delta t\right)^2 + ... + \left(\frac{\partial q}{\partial x}\Delta x\right)^2} \qquad \textbf{Eq. 7-2}$$

125

In the strain-expanded analysis, the data was least-squares fitted to $\sigma = E\varepsilon + D\varepsilon^2$, and the error values ΔE were calculated through error propagation from the above sources:

$$\frac{\Delta E}{E} = \sqrt{\left(\frac{\Delta\varepsilon}{\varepsilon}\right)^2 + \left(\frac{\Delta f}{f}\right)^2 + 2\left(\frac{\Delta d}{d}\right)^2} \qquad \textbf{Eq. 7-3}$$

$\varepsilon \equiv \text{strain}$
$f \equiv \text{force}$
$d \equiv \text{diameter}$

This form is valid in the low-strain limit where $E = \sigma/\varepsilon = (1/\varepsilon)\ 4f/\pi d^2$. The values used for ε and f are the midpoint values from the series of measured strain and force values for each given test. To determine ΔD, the error in D, least-squares fitting was performed to the functional form $\sigma = E^*\varepsilon + D^*\varepsilon^2$ where $E^* = E \pm \Delta E$. This will yield two values of D^*, one above and the other below the previously solved value for D, and the error ΔD is the lower of the two difference values, i.e. from the best D^* given a fixed ΔE. To determine Δb, the error in b, uncertainties ΔE and ΔD were propagated according to Eq. 1a.

For calculating δ, the above E values were used in the expression $\varepsilon = (\sigma/E) + \delta(\sigma/E)^2$, since in the low-strain limit E should be identical. Accordingly, the previously calculated ΔE values were used as well. The uncertainty $\Delta\delta$ was calculated by averaging the resulting errors from both Eqs. Eq. 7-1and Eq. 7-2, since neither alone sufficiently captures the relationship between the various sources of error ε, σ (with uncertainties from f and d) and E and the resulting quantity δ [274]. In particular, since Eq. 1b

assumes independent errors, to determine the partial derivatives of δ, E was assumed to be independent of ε and σ:

$$\Delta\delta = \sqrt{\left(\left.\frac{\partial\delta}{\partial\varepsilon}\right|_{E.\sigma}\Delta\varepsilon\right)^2 + \left(\left.\frac{\partial\delta}{\partial\sigma}\right|_{E,\varepsilon}\Delta\sigma\right)^2 + \left(\left.\frac{\partial\delta}{\partial E}\right|_{\varepsilon,\sigma}\Delta E\right)^2} \qquad \textbf{Eq. 7-4}$$

7.2   Plastic Response: Quasi-brittle Failure vs. Super-plastic-like Flow

The examined fracture morphologies of Pd NWs indicated not only dislocation-mediated plasticity, but deformation via partial dislocation nucleation resulting in stacking faults and twinning. While Pd has a high stacking fault energy of ($\sim$ 0.2 mJ/m^2) [275,276], this behavior is not unusual in defect-free FCC crystals with comparable stacking fault energies [24,28,225]. In <110>-oriented crystals, the Schmid factor for the leading partial is 0.47, almost twice that of the trailing partial, making it highly likely that several partials would nucleate first prior to any appearance of a trailing partial [185]. Nonetheless, several other parameters can influence the subsequent response, including stacking fault energy, surface facet orientation and surface roughness. For example, MD simulations on <110>-oriented NWs in tension generally show twinning or partial slip [27], except in the case of Al due to its high stacking fault energy [13]. Weinberger and Cai developed a two-parameter criterion for evaluating the propensity of different FCC metals to deform twinning, partial dislocation slip, or full dislocation slip. By employing various features of GSF curve and the Schmid factors for leading and trailing partials, this model has been able to consistently represent much of the behavior observed in

127

atomistic simulations [27]. Additionally, surface influences can have a profound effect: simulations of <100>-oriented nanowires with {100} surfaces were found to deform via twinning under compression due to the reorientation of these surface to {111} type, thus exhibiting much different behavior from <100> nanowires with different faceting [277,278]; and surface roughness on real nanowire specimens can act as weak points for preferential nucleation [139,279], which can lead to different sequences and arrangements of partial dislocations.
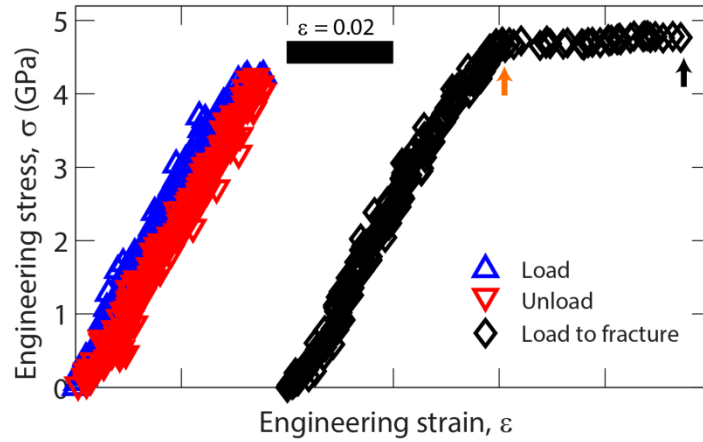
Figure 7-2 Representative stress-strain response in specimens exhibiting plastic flow after yielding for samples #1-4. Flow at roughly constant load was sustained until fracture (black arrow). The reported nucleation strength is the yield point (orange arrow).

Based on the criterion developed by Weinberger and Cai and stacking fault energy values using the tight-binding method, <110>-Pd nanowires have a borderline propensity for twinning and partials slip, which is consistent with our observations. The vast majority of Pd NWs tested exhibited quasi-brittle stress-strain behavior, where fracture immediately followed nucleation; however, in less than 10% of all cases, the Pd

NW undergoes a plastic flow regime at roughly constant load (Table 7-1 List of Pd NWs which exhibited plastic flow after nucleation.), and the cause for this is not yet clear. For most of the specimens, the elastic-to-plastic transitions were demarcated by a clear yield point, and in cases #1-5 plastic flow proceeded at close to constant load to fracture (Figure 7-2); therefore, in this and similar cases, we report the yield strength as the nucleation strength. Our microstructural characterization of these specimens exhibiting plastic flow showed no significant differences from the remainder of the experiments; thus, in Chapter 4 we treated most of the specimens as nominally similar.
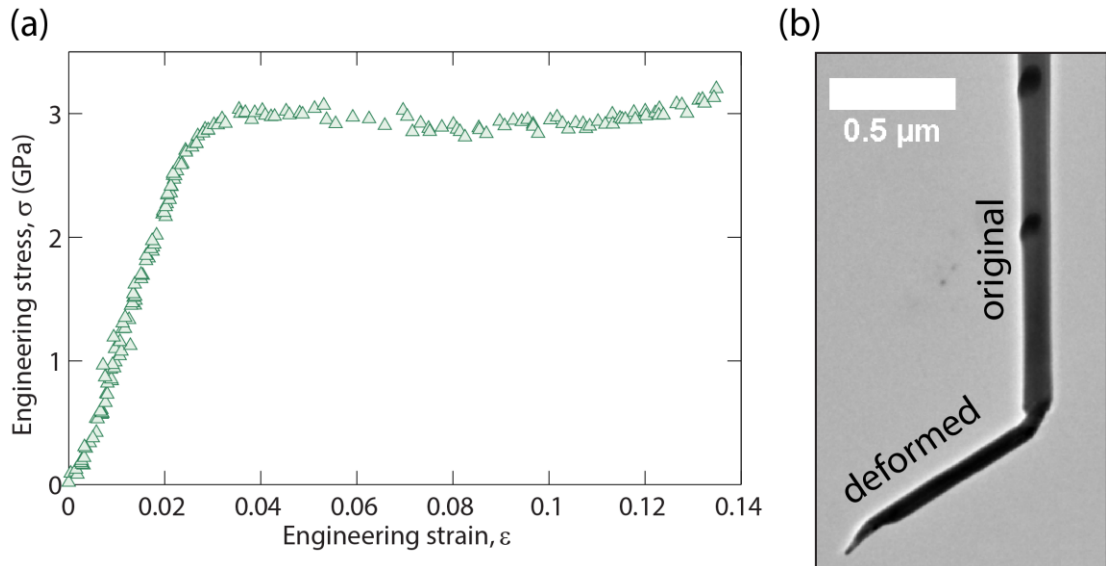
Figure 7-3 Specimen #5. (a) Fracture stress-strain curve and (b) fracture morphology

While not all the specimens could be re-manipulated for postmortem TEM imaging, most of the samples did not appear to exhibit very different fracture morphologies. For specimens #1-4, no distinctions in the fracture morphology compared to other samples could be discerned (#4 is actually sample (I) in Figure 4-2(a)). Samples

were tested with applied strain rates of 10^{-4} s^{-1} or lower. Most of the NWs were tested in the SEM with the exception of specimen #5 (Figure 7-3), which was tested at high temperature in the cryostat. This would likely suggest that heating and/or electron beam interactions, although then it is not entire clear why many other Pd NWs tested under these same conditions did not exhibit the same behavior.

Table 7-1 List of Pd NWs which exhibited plastic flow after nucleation.

#	T (K)	$\dot{\varepsilon}$ (s^{-1})	d (nm)	l (µm)	σ_{nucl} (GPa)	σ_{frac} (GPa)	ε_{pl}	Re-oriented?
1	295	5.5 x 10^{-5}	63	3.00	4.841	4.780	0.022	
2	295	3.4 x 10^{-4}	33	3.03	7.087	7.533	0.011	
3	295	1.8 x 10^{-4}	46	3.34	3.666	3.914	0.008	
4	295	4.2 x 10^{-5}	40	3.33	4.399	4.497	0.010	
5	447	1.0 x 10^{-4}	95	3.87	3.036	3.202	0.014	Y
6	295	---	75	7.49	---	---	0.376	Y

The most anomalous tests were performed for specimen #6, which deformed via clear propagation of a boundary separating the original and new NW orientations. Figure 7-4 shows the load cell and actuator displacement curves for load-unload test01-04. Unlike previous tests, there is a jump in both the load cell and actuator as the displacements during the initiation of the re-oriented segment. The initiation of the re-oriented region is occurs near the actuator, the boundary of which is marked in blue. Throughout test04, the boundary progressed towards the load side with at most a small rise in load at the apex corresponding to 123 MPa engineering stress. The NW did not fracture here but rather in test05, which is not shown in the displacement plot of Figure 7-4. Due to the limitations in actuation of the tensile testing stage, test05 was performed manually by using a Kleindiek nanomanipulator to push on the compliant load cell.

Fracture occurred on the actuator side (near the origin of boundary) most likely due to bending from misalignment (Figure 7-5(c)). In the end, the change in NW orientation along most of the original gage length is obvious and the total strain to fracture almost reaches 40%. This deformation behavior is not an anomaly among FCC metal nanowires. Seo *et al.* performed tensile test on Pd nanowires with {111} surfaces and found that these structures deformed via twinning up to strains as high as 41% [138], due to the re-orientation of the original [110] rhombus cross section to that of a square [100]{010} crystal via twinning. This has also been observed experimentally in Au [213,280] and for some FCC metals in atomistic simulations [13,277]. In all the above examples, however, it appears that the superplastic behavior is the rule and not the exception as it here.
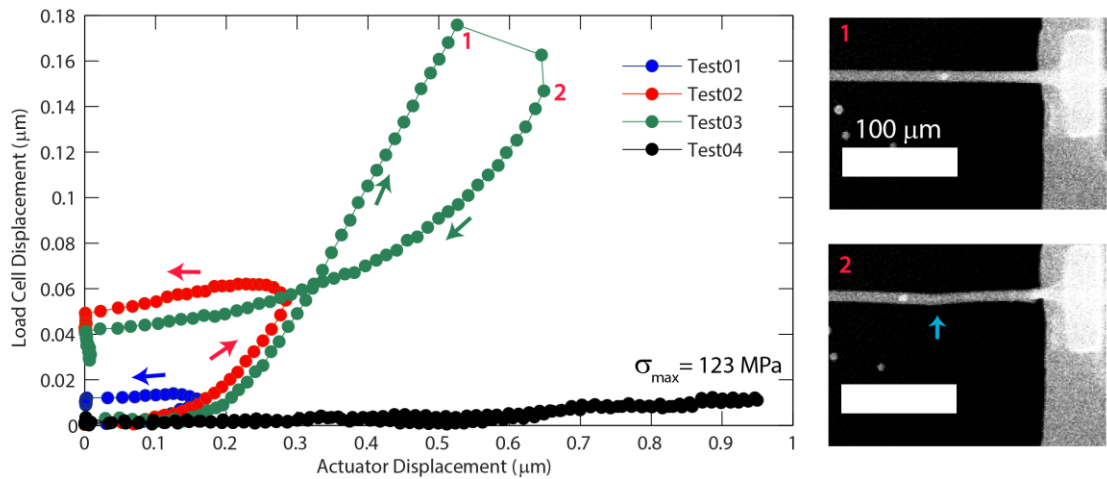
Figure 7-4 Load cell-actuator displacement curves for 4 load-unload tests on Sample 6. Arrows along the curves indicate the load-unload directions except for in test04, where the paths overlap. The simultaneous load drop and displacement shoot during test03 between points 1 and 2 correspond to a change in stress of 287 MPa and 0.02 strain, and corresponding micrographs of the re-orienting flow segment are provided on the right.

131

The blue arrow in image 2 indicates the first appearance of the propagating boundary Upon loading during test04, the load remains very low, maxing at 123 MPa at the apex.

One feature that remained unclear in the first three tests is the behavior of the load cell during actuator unloading: in tests 01 and 02 it displaces positively, indicating higher load as the actuator moves back, and after the actuator has come to rest the load cell gradually moves back to its original position. Also likely due to the strange behavior of the load cell, it is difficult to tell when the NW first yields prior to the evident buckling by the end of test02 (Figure 7-5(b)).
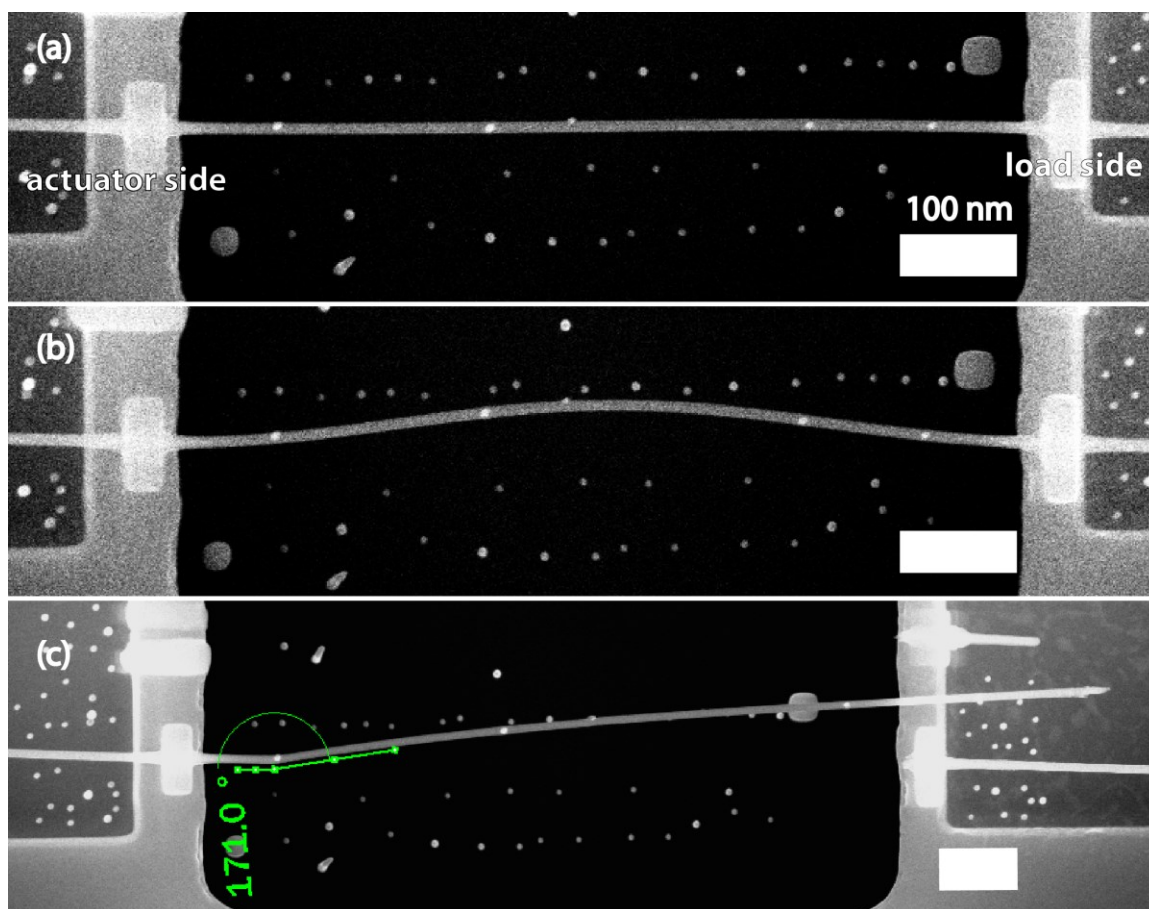
Figure 7-5 Snapshots of Sample #6 (a) prior to testing, (b) buckled at the end of test02, and (c) after fracture.

Other experimental studies on deformation in FCC nanowhiskers have shown some similar characteristics to what has been observed here [39,138,213]. Sedlmayr *et al*. found two different classes of deformation behavior in Au nanowhiskers [139,213]. Class I involved elastic loading up to smooth yielding, which proceeded via slip nucleating at multiple locations, and the flow stresses remained at high levels. This stress-strain response resembles the cases of specimens #1-4, although plasticity in the Pd NWs remained mostly locally concentrated. While the stress-strain response of Pd NW

#5 also resembled more closely the Class I behavior, the fracture morphology is more consistent with Class II, where the second type involved localized twinning forming extended regions which initiated during precipitous load drops. Class II also captures the various elements observed for deformation in #6. In order to understand why such different behavior would result from the same material, the authors also conducted MD simulations and found that the different fracture morphologies could be reproduced in Au by introducing flaws into the NW: Class 1 deformation corresponded to the pristine NW; Class II limited twinning (e.g. #5) required pre-existing stacking faults; and complete twinning reorientation required surface roughening, although the twinning process proceeded via multiple fronts that coalesced rather than the single boundary movement exemplified in #6 [213]. Nonetheless, these results highlight the importance of the surface structure in providing a variety of deformation responses within the same material.

7.3 Dependence of Nucleation Stress on Experimentally Adjustable Parameters

We outline in this section the approach of Zhu *et al*. to predict the relative temperature, strain rate, and size dependences of the nucleation stress σ_{nucl} [110]. This enabled us to develop predictions and therefore design our experiments in order to observe the greatest changes in measured strength beyond potential scatter.

For a tensile specimen held at constant stress σ for time t, the probability distribution of samples nucleating at a given time t is $P(t) = -\partial f(t)/\partial t$, where $f(t)$ is the cumulative survival probability representing the fraction of specimens that have *not* nucleated at t [162]. $P(t)$ is also the product of the nucleation rate $\upsilon(t)$ (increases with t) and $f(t)$ (decreases with t), thus:

$$\frac{df(t)}{dt} = -\upsilon f(t) \qquad \text{Eq. 7-5}$$

To translate time into a constant applied (elastic) strain rate, a change of variables is employed where $\sigma = E\dot{\varepsilon}t$.

$$\frac{df(\sigma)}{d\sigma} = \frac{-\upsilon}{E\dot{\varepsilon}} f(\sigma) \qquad \text{Eq. 7-6}$$

Here, E is the Young's modulus or small-strain elastic modulus (higher-order elasticity effects are ignored for simplicity).

The critical nucleation stress σ_c corresponds to when $P(\sigma)$ is a maximum or

$\frac{\partial^2 f}{\partial \sigma^2} = 0$. Inserting the expression for $\upsilon(\sigma) = N\upsilon_0 \exp\left(-\frac{\Delta G_{act}}{k_B T}\right)$ and $\Omega(\sigma, T) = \frac{\partial \Delta G_{act}}{\partial \sigma}\bigg|_T$

(from section 4.4) the peak at $P(\sigma_c)$ corresponds to the following relationship for $\upsilon(\sigma_c)$:

$$\upsilon(\sigma_c) = \frac{\Omega E \dot{\varepsilon}}{k_B T} \qquad\qquad \textbf{Eq. 7-7}$$

This further leads to the Gibbs free energy of activation for σ_c at a given temperature and

strain rate:

$$\frac{\Delta G_{act}(\sigma_c, T)}{k_B T} = \ln\left(\frac{k_B T N \upsilon_0}{E \dot{\varepsilon} \Omega(\sigma_c, T)}\right) \qquad\qquad \textbf{Eq. 7-8}$$

Now the task is to determine σ_c directly as a function of experimentally tunable

parameters T, $\dot{\varepsilon}$, and N. At finite temperature, the energy required to nucleate a

dislocation in the absence of applied stress is $\Delta F_{act}(T)$. If the activation parameters at a

reference finite stress σ_{ref} is known and one assumes a mostly constant activation volume

Ω_{ref} defined at σ_{ref} (assume stress-dependence of ΔG_{act} $\alpha \sim 1$), then $\Delta G_{act}(\sigma_{ref}) \cong \Delta F_{act} -$

$\Omega_{ref}\sigma_{ref}$. This expression can then be used in combination with Eq. 7-8:

$$\frac{\Delta G_{act}(\sigma_c, T)}{k_B T} \cong \ln\left(\frac{k_B T N \upsilon_0}{E \dot{\varepsilon} \Omega_{ref}}\right) = \frac{1}{k_B T}\left(\Delta F_{act} - \sigma_c \Omega_{ref}\right) \qquad \textbf{Eq. 7-9}$$

Which then can be solved for σ_c:

$$\sigma_c = \frac{\Delta F_{act}}{\Omega_{ref}} - \frac{k_B T}{\Omega_{ref}} \ln\left(\frac{k_B T N \upsilon_0}{E \dot{\varepsilon} \Omega_{ref}}\right) \qquad\qquad \textbf{Eq. 7-10}$$

Assuming your reference is nucleation at the athermal strength, the first term in Eq. 7-10, $\Delta F_{act}/\Omega_{ref}$ can be reduced to $\Delta U_{act}/\Omega_{ref}$ or the athermal stress σ_{ath}. In any case, Eq. 7-10 shows that with respect to a maximum reference stress, the most likely stress σ_c for a given set of testing parameters decreases with $T\ln T$ and $\ln N$ and increases with $\ln\dot{\varepsilon}$. These general trends makes intuitive sense (see Chapter 4) and in particular highlight the strong, almost linear dependence on temperature, showing that T as the most experimentally feasible parameter to vary in order to measure changes in strength. The dependence on T and $\dot{\varepsilon}$ is further illustrated in Figure 7-6.
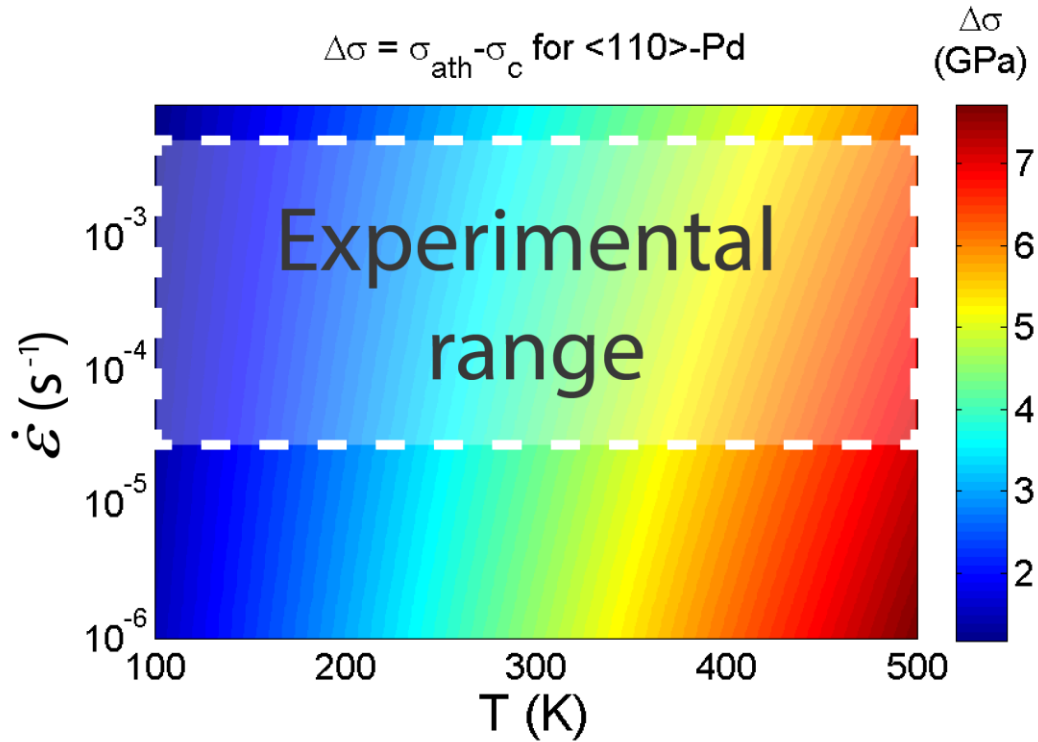
Figure 7-6 Plot of Eq. 7-10 for <110>-oriented Pd NWs. Length and diameter were assumed to be 3μm and 50 nm, respectively. The shaded region represents schematically the experimental range we accessed in the experiments of Chapter 4 and show clearly the much greater change in strength expected due to variation in temperature than strain rate (as well as length via N).

7.4 Contributions to Scatter of Nucleation Strengths Due to Experimental Uncertainties

Given the intrinsic stochastic nature of surface dislocation nucleation, it is important to address the influence of other potential contributors of experimental scatter or error in the measurement of nucleation strengths prior to conducting our full statistical analysis. We consider five primary sources of uncertainty: error due to variation in applied strain rate; errors in measurement of the NW cross-section; load-bearing by the hydrocarbon-based coating; correlation between measured strength and fracture location; and correlation between measured strength and microstructure.

The error owing to variation in strain rate introduced in the benchmark stress measurement can manifest in two manners: the deterministic error from including a range of strain rates within the benchmark data (1.0×10^{-4} s^{-1} < $\dot{\varepsilon}$ < 9.9×10^{-4} s^{-1}), and the experimental uncertainty for individual tests stemming from imaging and time resolution (time elapsed between image captures). These contributions can be calculated by using the approximated relationship between the critical nucleation stress and strain rate from Zhu et al. [110] The influence of strain rate on the strength measurements benchmark conditions is $\Delta\sigma = \left(\dfrac{k_b T}{\Omega}\right)^2 \dfrac{N \upsilon_0}{E \dot{\varepsilon}} \Delta\dot{\varepsilon}$. For the deterministic error contribution, using the parameters from the $\alpha = 4$ case and a maximum difference from the average strain rate of $\Delta\dot{\varepsilon} = 5.0 \times 10^{-4}$ s^{-1}, the upper bound for the increase in mean strength is 1.6 MPa. This

very small predicted change in the mean strength is consistent with the negligible strain rate dependence in Figure 4-4 in the main paper. For a given strength measurement the average uncertainty in the reported strain rate for the benchmark data is $\Delta\dot{\varepsilon} = 5.5\text{x}10^{-5}$ s^{-1}. This yields an uncertainty in the strength measurement of 0.18 MPa, which is orders of magnitude lower than the observed scatter.

For many NW specimens, the cross-sectional shape can be examined after fracture by either using the nanomanipulator to bend up the fractured ends or to use focused ion beam to cross-section the NW at the EBID contact [203]. The cross-section of most Pd NW specimens is hexagonal (truncated rhombic) and consistent with Wulff shape predictions. To assess the error from assuming a circular-cross section based on measurements of the projected effective diameter, we calculated the difference in area between a circle and a regular hexagon. This circular approximation for area can underestimate the true area by 10% or overestimate by as much as 21%, depending on the azimuthal viewing angle. In some cases, a more oblong cross-section had been observed with an aspect ratio of about 2:1 and approximated as an ellipse. The error is bounded by the difference between an ellipse and a rectangle of the same dimensions, which is approximately 21%. For the average NW diameter of 60 nm or equivalent-area cross-section, this would result in an average deviation in measured strength of about 10%, which is comparable to the error from imaging resolution reflected in the current error bars.

Post-manipulation imaging of both postmortem and pristine (not tested) Pd NWs indicate the universal presence of a hydrocarbon-based contamination layer ranging

anywhere between 1-20 nm thick. Contamination of the pristine NW surfaces during electron microscopy imaging results from two primary sources: interaction of the electron beam with organic molecules in the chamber [249,250], and the organometallic gas precursor used to create the Pt-EBID contacts necessary for mechanical testing. The latter can occur from delocalization of the primary electron beam, decomposition of the precursor gas owing to secondary electron scattering events away from the primary beam, or diffusion of the deposited species along the NW. Based on stiffness measurements in unreinforced hydrocarbon deposition of 34-60 GPa [281], the coating volume fraction can be as high as 65% and the apparent load bearing of the NW would be predicted to increase as much as 80% for diameters as small as 30 nm. To evaluate the effect of load-bearing, we performed load-unload tests on samples with increasing amounts of coating and measured the apparent stiffness (load borne by NW cross-section only). For one sample, coating thickness volume fraction increased from 22% to 41% due to long dwell-time imaging in the SEM, where contaminants pre-existing in the chamber decomposed under the electron beam. In another case, we employed both long dwell-time imaging and imaging with the Pt-EBID source over the entire gage to mimic deposition conditions during manipulation, increasing the volume fraction from 26% to 34%. In both cases, we found no increase in apparent load borne by the NW beyond the uncertainty due to imaging noise (~0.08 μN or ~20 MPa). This suggests that even in the most extreme cases of the smallest NW diameters, the hydrocarbon-based coating does not significantly affect our strength measurements.

The uniaxial testing geometry and the high crystal quality of the Pd NWs we employ enable equal likelihood of nucleation at any site along the tested gage length. In practice (and in macroscopic testing), fracture towards the middle of the gage is most easily interpreted because this can be exclusively attributed to the response of the material. In contrast, fracture near the grips or "end fracture" may indicate geometric weakening owing to stress concentrations or misalignment-induced bending, resulting in lower measured strengths. In order to test a null hypothesis that σ_{nucl} is not significantly correlated with fracture location, we have separated the benchmark data in two groups (Table 7-2). Within our "benchmark" data, there are 11 wires that fractured within the gage section and 6 that fractured at or near the grip (Figure 7-7) (this proportion of about 30% end fractures is also representative of the entire data set). The two groups were analyzed with basic statistical methods and results are shown below (Table 7-2 Statistical parameters for two groups representing different fracture locations.). Even though the average strength of wires fractured in the middle was higher by ~1 GPa, a basic t-test shows the difference between these groups to be statistically insignificant (p-value of 0.09).
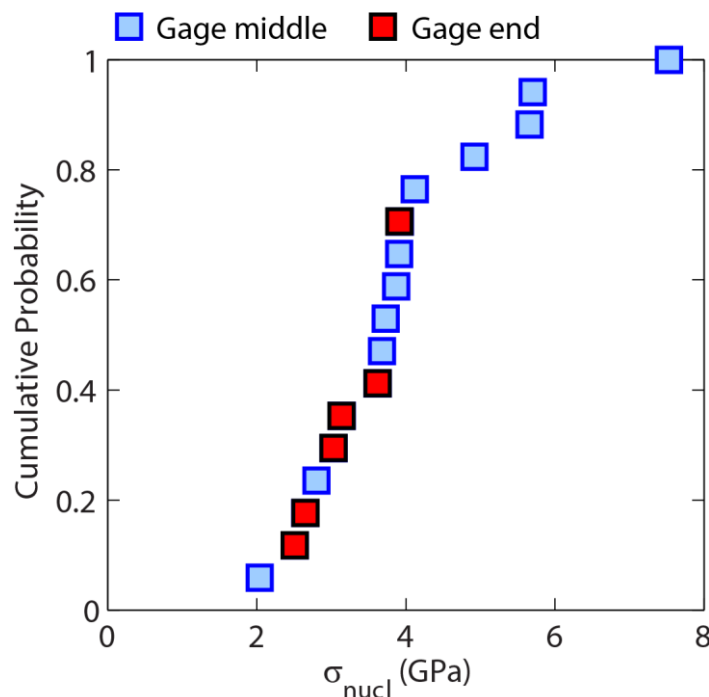
Figure 7-7 Experimental CDF distinguishing the fracture location for each specimen and its corresponding measured strength.

Table 7-2 Statistical parameters for two groups representing different fracture locations.

	Middle fracture	End fracture
Number of samples	11	6
Average σ_{nucl} (GPa)	4.36	3.05
Standard deviation (GPa)	1.52	0.55

The tested Pd NWs were either completely free of defects or contained stacking faults aligned along the axis of the NW. While the stacking fault itself is not expected to be activated during tensile testing since there is no resolved shear stress along the fault, and indeed has been observed to remain in the NW after fracture, it could have an influence on the nucleation of a dislocation via a back stress or by intersecting with corner nucleation sites, creating an atomically modified corner geometry. No such

142

defects were observed in NW specimens harvested from the $SrTiO_3$ substrate, but about 50% of the NWs from Al_2O_3 investigated in the TEM possessed such defects. Among the benchmark data, 12 samples were from $SrTiO_3$ and the remaining 5 are from Al_2O_3 (Figure 7-8). Our t-test results indicate that the difference between the two groups is not statistically significant (p-value of 0.30). This suggests that any difference in strength related to the presence of the stacking fault defect is dwarfed by the thermal uncertainty of the nucleation process, which is the primary objective of this work.
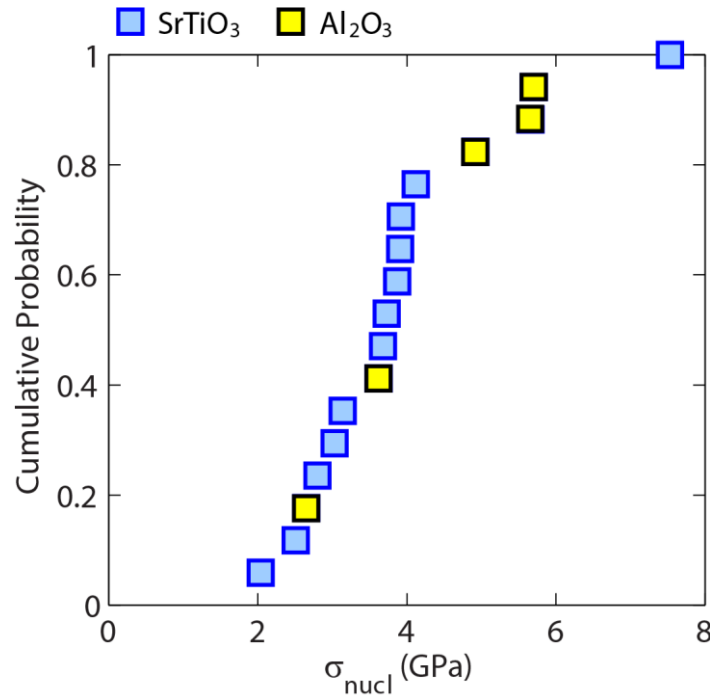
Figure 7-8 Experimental CDF distinguishing growth substrate for each specimen and the respective nucleation strength.

Table 7-3 Statistical parameters for two groups representing different growth substrates.

	SrTiO$_3$	Al$_2$O$_3$
Number of samples	12	5
Average σ_{nucl} (GPa)	3.69	4.51
Standard deviation (GPa)	1.44	1.34

The cumulative effect of these sources of experimental error is dominated by the uncertainty in the cross-section area. For most samples, this error is comparable to the uncertainties in diameter measurement and, consequently, in the resulting uncertainty in strength measurement displayed as error bars in Figure 4-3. Clearly the measured scatter at benchmark conditions alone surpasses the breadth of these uncertainties; therefore, we attribute the scatter primarily to the thermally activated nature of plastic deformation in these NWs.

7.5 Determining the Thermal Activation Parameters for Weak Stress Dependence of the Activation Energy (α = 1)

Previous experimental studies extracting the activation parameters for dislocation nucleation assume a linear stress dependence of the enthalpy of activation, i.e. $\Delta H_{act}(\sigma) = \Delta U_{act}(1 - \sigma/\sigma_{ath})$, where ΔU_{act} is the activation energy. (It should also be noted that ΔH_{act} in these earlier studies has been treated as temperature-independent, and we maintain this convention for the current analysis. Within the low temperature regime accessed in our study, we find that the $(1 - T/T_m)$ factor does not significantly affect the resulting fit.) This results in a stress-independent activation volume $\Omega = \Delta H_{act}/\sigma_{ath}$, which is in

contradiction to results found in many theoretical studies. Aside from its mathematical simplicity and application in other experimental studies [149,223], it represents the weaker limit of stress-dependence that has been identified in theoretical studies in literature [282]. We have been able to apply this model to our data successfully, enabling us to compare both extreme cases of weak ($\alpha = 1$) and strong ($\alpha = 4$) temperature dependence.

For a given strain rate and temperature, the spread of measured yield strengths provides a cumulative distribution function to which an assumed analytical model can be applied. From transition state theory (TST), the rate of dislocation nucleation υ can be expressed as:

$$\upsilon = \begin{cases} N\upsilon_0 \exp\left(-\dfrac{\Delta U_{act}}{k_B T}\right) \exp\left(\dfrac{E\dot{\varepsilon}t\Omega}{k_B T}\right) \text{ for } 0 \leq \sigma \leq \sigma_{ath} \\ N\upsilon_0 \text{ for } \sigma > \sigma_{ath} \end{cases}$$

Eq. 7-11

where we assume $\sigma = E\dot{\varepsilon}t$ and E, the Young's modulus is stress-independent. This formulation takes into account that even in the absence of an energy barrier, nucleation is limited by the kinetics of the system. Plugging this into the following expression for the cumulative distribution function (CDF) [222]

$$F(t) = 1 - \exp\left(-\int \upsilon(t)dt\right)$$

Eq. 7-12

yields the final expression:

$$F(\sigma) = \begin{cases} \left(1 - \exp\left(\frac{N\upsilon_0 k_B T}{E\dot{\varepsilon}\Omega}\left[\exp\left(-\frac{\Delta U_{act}}{k_B T}\right) - \exp\left(\frac{\Omega\sigma - \Delta U_{act}}{k_B T}\right)\right]\right)\right) & \text{for } 0 \leq \sigma \leq \sigma_{ath} \\[4mm] \left(1 - \exp\left(\frac{N\upsilon_0 k_B T}{E\dot{\varepsilon}\Omega}\left[\exp\left(-\frac{\Delta U_{act}}{k_B T}\right) - 1 - \frac{\Omega\sigma - \Delta U_{act}}{k_B T}\right]\right)\right) & \text{for } \sigma > \sigma_{ath} \end{cases}$$

<div align="right">**Eq. 7-13**</div>

When fitting the first part of Eq. S2b to the experimental cumulative distribution function, we can solve for the relevant parameters Ω, $N\upsilon_0$, and ΔU_{act}. For the activation volume, we obtain a value of $0.23b^3$, where b is the full Burger's vector in Pd. Similar to the $\alpha = 4$ case, this fitted value for Ω is much lower than the range of 1-$10b^3$, which has been theoretically predicted for heterogeneous nucleation [110]. On the other hand, for the fitting of the rate prefactor $N\upsilon_0$ to the experimental we obtain 0.47 s^{-1}, orders of magnitude lower than theoretical predictions based on the Debye frequency (as discussed in the main text). However, this prefactor is also consistent with the expectation time provided in the load-hold test in the main paper, yielding an expectation time of 150 s at 3.8 GPa.

From Eq. 7-13 it is also possible to extract values for ΔU_{act} from the room temperature CDF. While the value for ΔU_{act} (and thereby the athermal strength) should be determined by temperature-dependent behavior, this fit provides an initial estimate of 0.18 eV. To comprehensively evaluate the temperature-dependent behavior and extract ΔU_{act}, Eq. S2b is solved for stress as a function of temperature:

$$\sigma(T) = \begin{cases} \dfrac{k_B T}{\Omega} \ln\left(\exp\left(-\dfrac{\Delta U_{act}}{k_B T}\right) - \dfrac{E\dot{\varepsilon}\Omega}{k_B T N \upsilon_0} \ln\left(1 - F(\sigma)\right)\right) + \dfrac{\Delta U_{act}}{\Omega} & \text{for } 0 \le \sigma \le \sigma_{ath} \\[3ex] \dfrac{k_B T}{\Omega}\left(\exp\left(-\dfrac{\Delta U_{act}}{k_B T}\right) - 1\right) - \dfrac{E\dot{\varepsilon}}{N\upsilon_0} \log\left(1 - F(\sigma)\right) + \dfrac{\Delta U_{act}}{\Omega} & \text{for } \sigma > \sigma_{ath} \end{cases} \qquad \textbf{Eq. 7-14}$$

This yields $\Delta U_{act} = 0.23$ eV, which agrees very well with the fit derived from the room-temperature CDF alone of 0.18 eV. At room temperature, σ_c is then 5.85 GPa, leading to a $\Delta H_{act} = \Delta U_{act} - \Omega\sigma$ of 0.047 eV, which is still lower than predictions from NEB calculations for partial dislocation nucleation in single-crystal Cu NWs (0.1 and 0.6 eV) [110]. Nonetheless, the current value for ΔU_{act} yields an athermal strength in Pd NWs of 7.46 GPa, which is comparable to the highest strengths measured at low temperatures.

8 BIBLIOGRAPHY

[1]   Hummel R E 2004 *Understanding Materials Science* (New York: Springer)

[2]   Callister W D 2007 *Materials Science and Engineering: An Introduction* (New York: Wiley)

[3]   Kayser F X and Patterson J W 1998 Sir William Chandler Roberts-Austen — His role in the development of binary diagrams and modern physical metallurgy *J. Phase Equilibria* **19** 11–8

[4]   Faraday M 1833 On a New Law of Electric Conduction; On Conducting Power Generally *R. Soc.*

[5]   Michalet X, Pinaud F F, Bentolila L A, Tsay J M, Doose S, Li J J, Sundaresan G, Wu A M, Gambhir S S and Weiss S 2005 Quantum dots for live cells, in vivo imaging, and diagnostics. *Science* **307** 538–44

[6]   Yamauchi M, Ikeda R, Kitagawa H and Takata M 2008 Nanosize Effects on Hydrogen Storage in Palladium *J. Phys. Chem. C* **112** 3294–9

[7]   Jang S, Kim B, Geier M L, Prabhumirashi P L, Hersam M C and Dodabalapur A 2014 Fluoropolymer coatings for improved carbon nanotube transistor device and circuit performance *Appl. Phys. Lett.* **105** 122107

[8]   Kim D-H, Lu N, Ma R, Kim Y-S, Kim R-H, Wang S, Wu J, Won S M, Tao H, Islam A, Yu K J, Kim T, Chowdhury R, Ying M, Xu L, Li M, Chung H-J, Keum H, McCormick M, Liu P, Zhang Y-W, Omenetto F G, Huang Y, Coleman T and Rogers J A 2011 Epidermal electronics. *Science* **333** 838–43

[9]   Ferrari M 2005 Cancer nanotechnology: opportunities and challenges. *Nat. Rev. Cancer* **5** 161–71

[10]   Schroeder A, Goldberg M S, Kastrup C, Wang Y, Jiang S, Joseph B J, Levins C G, Kannan S T, Langer R and Anderson D G 2012 Remotely activated protein-producing nanoparticles. *Nano Lett.* **12** 2685–9

[11]   Agrawal R, Loh O and Espinosa H D 2010 The Evolving Role of Experimental Mechanics in 1-D Nanostructure-Based Device Development *Exp. Mech.* **51** 1–9

[12]   Shea H R 2006 Reliability of MEMS for space applications ed D M Tanner and R Ramesham **6111** 61110A – 61110A – 10

[13]   Liang W and Zhou M 2006 Atomistic simulations reveal shape memory of fcc metal nanowires *Phys. Rev. B* **73** 115409

[14]   Jankovic L, Gournis D, Trikalitis P N, Arfaoui I, Cren T, Rudolf P, Sage M-H, Palstra T T M, Kooi B, De Hosson J, Karakassides M a, Dimos K, Moukarika A and Bakas T 2006 Carbon nanotubes encapsulating superconducting single-crystalline tin nanowires. *Nano Lett.* **6** 1131–5

[15]   Buchner S, Rapchun D A, Moseley H, Meyer S E, Oldham T, Ray K, Tuttle J, Quinn E, Buchanan E, Bloom D, Hait T, Pearce M, Beamer A and Stage A R 2007 Response of a MEMS Microshutter Operating at 60 K to Ionizing Radiation **54** 2463–7

[16]   Yang F, Taggart D K and Penner R M 2009 Fast, sensitive hydrogen gas detection using single palladium nanowires that resist fracture. *Nano Lett.* **9** 2177–82

[17]   Brenner S S 1956 Tensile Strength of Whiskers *J. Appl. Phys.* **27** 1484

[18]   Brenner S S 1957 Plastic Deformation of Copper and Silver Whiskers *J. Appl. Phys.* **28** 1023

[19]   Piper W and Roth W 1953 Perfect Crystals of Zinc Sulfide *Phys. Rev.* **92** 503–503

[20]   Gyulai Z 1954 Festigkeits- und Plastizitatseigenschaften von NaCl-Nadelkristallen *Zeitschrift fur Phys.* **138** 317–21

[21]   Pearson G ., Read W . and Feldmann W . 1957 Deformation and fracture of small silicon crystals *Acta Metall.* **5** 181–91

[22]   Brenner S S 1958 Growth and Properties of "Whiskers": Further research is needed to show why crystal filaments are many times as strong as large crystals. *Science* **128** 569–75

[23]   Weibull W 1951 A statistical distribution function of wide applicability *J. Appl. Phys.* **18** 293–7

[24]   Diao J, Gall K and Dunn M L 2004 Yield Strength Asymmetry in Metal Nanowires *Nano Lett.* **4** 1863–7

[25]   Diao J, Gall K, Dunn M L and Zimmerman J a. 2006 Atomistic simulations of the yielding of gold nanowires *Acta Mater.* **54** 643–53

[26]   Diao J, Gall K and L. Dunn M 2004 Atomistic simulation of the structure and elastic properties of gold nanowires *J. Mech. Phys. Solids* **52** 1935–62

[27]   Weinberger C R and Cai W 2012 Plasticity of metal nanowires *J. Mater. Chem.* **22** 3277

149

[28]   Jennings A T, Weinberger C R, Lee S-W, Aitken Z H, Meza L and Greer J R 2013 Modeling dislocation nucleation strengths in pristine metallic nanowires under experimental conditions *Acta Mater.* **61** 2244–59

[29]   Park H S, Cai W, Espinosa H D and Huang H 2009 Mechanics of Crystalline Nanowires *MRS Bull.* **34** 178–83

[30]   Song F, Huang G L, Park H S and Liu X N 2011 A continuum model for the mechanical behavior of nanowires including surface and surface-induced initial stresses *Int. J. Solids Struct.* **48** 2154–63

[31]   He J and Lilley C M 2008 Surface effect on the elastic behavior of static bending nanowires. *Nano Lett.* **8** 1798–802

[32]   Miller R E and Shenoy V B 2000 Size-dependent elastic properties of nanosized structural elements *Nanotechnology* **11** 139–47

[33]   Diao J, Gall K and Dunn M 2004 Surface stress driven reorientation of gold nanowires *Phys. Rev. B* **70** 075413

[34]   Kobayashi H and Hiki Y 1973 Anharmonicity in Noble Metals; Nonlinear Elasticity in Whiskers *Phys. Rev. B* **7** 594–601

[35]   Liang H, Upmanyu M and Huang H 2005 Size-dependent elasticity of nanowires: Nonlinear effects *Phys. Rev. B* **71** 241403(R)

[36]   WUWEI L and MIN Z Pseudoelasticity of single crystalline cu nanowires through reversible lattice reorientations : Nanomaterials and Nanomechanics *J. Eng. Mater. Technol.* **127** 423–33

[37]   Zhu T and Li J 2010 Ultra-strength materials *Prog. Mater. Sci.* **55** 710–57

[38]   Li J, Van Vliet K J, Zhu T, Yip S and Suresh S 2002 Atomistic mechanisms governing elastic limit and incipient plasticity in crystals. *Nature* **418** 307–10

[39]   Richter G, Hillerich K, Gianola D S, Mönig R, Kraft O and Volkert C a 2009 Ultrahigh strength single crystalline nanowhiskers grown by physical vapor deposition. *Nano Lett.* **9** 3048–52

[40]   Gianola D S and Eberl C 2009 Micro- and nanoscale tensile testing of materials *JOM* **61** 24–35

[41]   Haque M and Espinosa H 2010 MEMS for In Situ Testing — Handling , Actuation , Loading , and Displacement Measurements *MRS Bull.* **35** 375–81

[42]   Haque M a and Saif M T a 2002 In-situ tensile testing of nano-scale specimens in SEM and TEM *Exp. Mech.* **42** 123–8

150

[43]   Ganesan Y, Lu Y, Peng C, Lu H, Ballarini R and Lou J 2010 Development and Application of a Novel Microfabricated Device for the In Situ Tensile Testing of 1-D Nanomaterials **19** 675–82

[44]   Tan E P S and Lim C T 2004 Novel approach to tensile testing of micro- and nanoscale fibers *Rev. Sci. Instrum.* **75** 2581

[45]   Lu Y and Lou J 2011 Quantitative in-situ nanomechanical characterization of metallic nanowires *Jom* **63** 35–42

[46]   Hiki Y 1981 Higher Order Elastic Constants of Solids *Annu. Rev. Mater. Sci.* **11** 51–73

[47]   Hiki Y, Thomas J and Granato A 1967 Anharmonicity in Noble Metals: Some Thermal Properties *Phys. Rev.* **153** 764–71

[48]   Thomas J 1968 Third-Order Elastic Constants of Aluminum *Phys. Rev.* **175** 955–62

[49]   Seeger A and Buck O 1960 Die experimentelle Ermittlung der elastischen Konstanten höherer Ordnung *Zeitschrift Naturforsch. Tl. A* **15** 1056–67

[50]   Lambson E, Lambson W, Macdonald J, Gibbs M, Saunders G and Turnbull D 1986 Elastic behavior and vibrational anharmonicity of a bulk $Pd_{40}Ni_{40}P_{20}$ metallic glass *Phys. Rev. B* **33** 2380–5

[51]   Weinmann C and Steinemann S 1974 Temperature and volume dependence of the elastic constants of palladium *Phys. Lett. A* **47** 275–6

[52]   Peters R, Breazeale M and Paré V 1970 Ultrasonic Measurement of the Temperature Dependence of the Nonlinearity Parameters of Copper *Phys. Rev. B* **1** 3245–50

[53]   Soma T, Satoh H and Matsuo H 1981 Equation of state and elastic stiffness constants under pressure of noble metals *Solid State Commun.* **40** 933–6

[54]   Lee C, Wei X, Kysar J W and Hone J 2008 Measurement of the elastic properties and intrinsic strength of monolayer graphene. *Science* **321** 385–8

[55]   Hearmon R F S 1953 `Third-order' elastic coefficients *Acta Crystallogr.* **6** 331–40

[56]   Milstein F and Rasky D 1982 Anharmonicity and symmetry in crystals *Philos. Mag. A* **45** 49–61

[57]   Powell B and Skove M 1968 Measurement of Higher-Order Elastic Constants, Using Finite Deformations *Phys. Rev.* **174** 977–83

[58]   Haque M a and Saif M T a 2003 A Review of MEMS-Based Microscale and Nanoscale Tensile and Bending Testing *Exp. Mech.* **43** 248–55

[59] Riley M and Skove M 1973 Higher-Order Elastic Constants of Copper and Nickel Whiskers *Phys. Rev. B* **8** 466–74

[60] Hiki Y and Granato A 1966 Anharmonicity in Noble Metals; Higher Order Elastic Constants *Phys. Rev.* **144** 411–9

[61] Park H and Klein P 2007 Surface Cauchy-Born analysis of surface stress effects on metallic nanowires *Phys. Rev. B* **75** 085408

[62] Zhou L G and Huang H 2004 Are surfaces elastically softer or stiffer? *Appl. Phys. Lett.* **84** 1940

[63] Gurtin M and Ian Murdoch A 1975 A continuum theory of elastic material surfaces *Arch. Ration. Mech. Anal.* **57**

[64] Shenoy V 2005 Atomistic calculations of elastic properties of metallic fcc crystal surfaces *Phys. Rev. B* **71** 094104

[65] Cammarata R C and Sieradzki K 1994 Surface and Interface Stresses *Annu. Rev. Mater. Sci.* **24** 215–34

[66] Wang G-F and Feng X-Q 2007 Effects of surface elasticity and residual surface tension on the natural frequency of microbeams *Appl. Phys. Lett.* **90** 231904

[67] Wu B, Heidelberg A and Boland J J 2005 Mechanical properties of ultrahigh-strength gold nanowires. *Nat. Mater.* **4** 525–9

[68] Wu B, Heidelberg A, Boland J J, Sader J E, Sun X and Li Y 2006 Microstructure-hardened silver nanowires. *Nano Lett.* **6** 468–72

[69] Jing G, Duan H, Sun X, Zhang Z, Xu J, Li Y, Wang J and Yu D 2006 Surface effects on elastic properties of silver nanowires: Contact atomic-force microscopy *Phys. Rev. B* **73** 235409

[70] Chang I-L and Chen Y-C 2007 Is the molecular statics method suitable for the study of nanomaterials? A study case of nanowires *Nanotechnology* **18** 315701

[71] McDowell M T, Leach A M and Gall K 2008 On the elastic modulus of metallic nanowires. *Nano Lett.* **8** 3613–8

[72] Cuenot S, Frétigny C, Demoustier-Champagne S and Nysten B 2004 Surface tension effect on the mechanical properties of nanomaterials measured by atomic force microscopy *Phys. Rev. B* **69** 165410

[73] Treacy M M J, Ebbesen T W and Gibson J M 1996 Exceptionally high Young's modulus observed for individual carbon nanotubes *Nature* **381** 678–80

[74] Petrova H, Perez-Juste J, Zhang Z, Zhang J, Kosel T and Hartland G V. 2006 Crystal structure dependence of the elastic constants of gold nanorods *J. Mater. Chem.* **16** 3957

[75] Heidelberg A, Ngo L T, Wu B, Phillips M A, Sharma S, Kamins T I, Sader J E and Boland J J 2006 A generalized description of the elastic properties of nanowires. *Nano Lett.* **6** 1101–6

[76] Wong, E. W., Sheehan, P. E., Lieber C M 1997 Nanobeam Mechanics: Elasticity, Strength, and Toughness of Nanorods and Nanotubes *Science (80-.).* **277** 1971–5

[77] Chen Y, Dorgan B L, McIlroy D N and Eric Aston D 2006 On the importance of boundary conditions on nanomechanical bending behavior and elastic modulus determination of silver nanowires *J. Appl. Phys.* **100** 104301

[78] Nilsson S G, Borrisé X and Montelius L 2004 Size effect on Young's modulus of thin chromium cantilevers *Appl. Phys. Lett.* **85** 3555

[79] Chen C, Shi Y, Zhang Y, Zhu J and Yan Y 2006 Size Dependence of Young's Modulus in ZnO Nanowires *Phys. Rev. Lett.* **96** 075505

[80] Zhu Y, Qin Q, Xu F, Fan F, Ding Y, Zhang T, Wiley B J and Wang Z L 2012 Size effects on elasticity, yielding, and fracture of silver nanowires: In situ experiments *Phys. Rev. B* **85** 045443

[81] Yun G and Park H 2009 Surface stress effects on the bending properties of fcc metal nanowires *Phys. Rev. B* **79** 32–5

[82] Wang Z-J, Liu C, Li Z and Zhang T-Y 2010 Size-dependent elastic properties of Au nanowires under bending and tension—Surfaces versus core nonlinearity *J. Appl. Phys.* **108** 083506

[83] Dingreville R, Qu J and Cherkaoui M 2005 Surface free energy and its effect on the elastic behavior of nano-sized particles, wires and films *J. Mech. Phys. Solids* **53** 1827–54

[84] Hertzberg R W 1996 *Deformation and Fracture Mechanics of Engineering Materials* (Hoboken: Wiley)

[85] Hirsch P B, Horne R W and Whelan M J 1956 LXVIII. Direct observations of the arrangement and motion of dislocations in aluminium *Philos. Mag.* **1** 677–84

[86] Bollmann W 1956 Interference Effects in the Electron Microscopy of Thin Crystal Foils *Phys. Rev.* **103** 1588–9

[87] Taylor G I 1934 The Mechanism of Plastic Deformation of Crystals. Part I. Theoretical *Proc. R. Soc. A Math. Phys. Eng. Sci.* **145** 362–87

[88] Orowan E 1934 Zur Kristallplastizität. I *Zeitschrift für Phys.* **89** 605–13

153

[89] Polanyi M 1934 Über eine Art Gitterstörung, die einen Kristall plastisch machen könnte *Zeitschrift für Phys.* **89** 660–4

[90] Burgers J M 1939 Some considerations on the fields of stress connected with dislocations in a regular crystal lattice. I. *K. Ned. Akad. van Wet.* **42** 293

[91] Pashley D W 1965 The direct observation of imperfections in crystals *Reports Prog. Phys.* **28** 291–330

[92] Frank F C 1949 The influence of dislocations on crystal growth *Discuss. Faraday Soc.* **5** 48

[93] Penn R L 1998 Imperfect Oriented Attachment: Dislocation Generation in Defect-Free Nanocrystals *Science (80-.).* **281** 969–71

[94] Cullity B D and Stock S R 2001 *Elements of X-Ray Diffraction* (Prentice Hall)

[95] Hirth J P and Pond R C 1996 Steps, dislocations and disconnections as interface defects relating to structure and phase transformations *Acta Mater.* **44** 4749–63

[96] Swann P R 1963 Dislocation Substructure vs Transgranular Stress Corrosion Susceptibility Of Single Phase Alloys *Corrosion* **19** 102t – 114t

[97] Farvacque J L, Douehan J C, von Alpen U and Gmelin E 1977 Screw-dislocation-induced scattering processes and acceptor states in Te *Phys. Status Solidi* **79** 763–73

[98] Rogers D J, Hosseini Teherani F, Yasan A, Minder K, Kung P and Razeghi M 2006 Electroluminescence at 375 nm from a ZnO∕GaN:Mg∕c-Al2O3 heterojunction light emitting diode *Appl. Phys. Lett.* **88** 141918

[99] Nam S-W, Chung H-S, Lo Y C, Qi L, Li J, Lu Y, Johnson a T C, Jung Y, Nukala P and Agarwal R 2012 Electrical wind force-driven and dislocation-templated amorphization in phase-change nanowires. *Science* **336** 1561–6

[100] Chu M, Sun Y, Aghoram U and Thompson S E 2009 Strain: A Solution for Higher Carrier Mobility in Nanoscale MOSFETs *Annu. Rev. Mater. Res.* **39** 203–29

[101] Cottrell A H 1953 *Dislocations and Plastic Flow in Crystals* (Oxford: Clarendon Press)

[102] Caillard D and Martin J L 2003 *Thermally Activated Mechanisms in Crystal Plasticity* (Oxford: Elsevier)

[103] Kocks U F, Argon A . and Ashby M F 1973 *Thermodynamics and Kinetics of Slip* (Argonne National Laboratory)

[104] Frost H J and Ashby M F 1982 *Deformation-Mechanism Maps* (Elmsford, NY: Pergamon Press Inc.)

[105] Gibbs G B 1965 The Thermodynamics of Thermally-Activated Dislocation Glide *Phys. status solidi* **10** 507–12

[106] Hirth J P and Nix W D 1969 An Analysis of the Thermodynamics of Dislocation Glide *Phys. status solidi* **35** 177–88

[107] Glasstone S, Laidler K J and Eyring H 1941 *The Theory of Rate Processes* (New York: McGraw-Hill)

[108] Jacobs T D B, Gotsmann B, Lantz M a. and Carpick R W 2010 On the Application of Transition State Theory to Atomic-Scale Wear *Tribol. Lett.* **39** 257–71

[109] Vineyard G 1957 Frequency factors and isotope effects in solid state rate processes *J. Phys. Chem. Solids* **3** 121–7

[110] Zhu T, Li J, Samanta A, Leach A and Gall K 2008 Temperature and Strain-Rate Dependence of Surface Dislocation Nucleation *Phys. Rev. Lett.* **100** 025502

[111] Ryu S, Kang K and Cai W 2011 Predicting the dislocation nucleation rate as a function of temperature and stress *J. Mater. Res.* **26** 2335–54

[112] Ryu S, Kang K and Cai W 2011 Entropic effect on the rate of dislocation nucleation. *Proc. Natl. Acad. Sci. U. S. A.* **108** 5174–8

[113] Ashby M 1972 A first report on deformation-mechanism maps *Acta Metall.* **20**

[114] Wang Y M, Hamza a. V. and Ma E 2005 Activation volume and density of mobile dislocations in plastically deforming nanocrystalline Ni *Appl. Phys. Lett.* **86** 241917

[115] Brenner S S 1959 Strength of Gold Whiskers *J. Appl. Phys.* **30** 266

[116] Eisner R L 1955 Tensile tests on silicon whiskers *Acta Metall.* **3** 414–5

[117] Frank F and Read W 1950 Multiplication Processes for Slow Moving Dislocations *Phys. Rev.* **79** 722–3

[118] Kiener D and Minor A M 2011 Source Truncation and Exhaustion : Insights from Quantitative in situ TEM Tensile Testing *Nano* **11** 3816–20

[119] Zhou C, Beyerlein I J and LeSar R 2011 Plastic deformation mechanisms of fcc single crystals at small scales *Acta Mater.* **59** 7673–82

[120] Oh S H, Legros M, Kiener D and Dehm G 2009 In situ observation of dislocation nucleation and escape in a submicrometre aluminium single crystal *Nat. Mater.* **8** 95–100

[121] Volkert C a. and Lilleodden E T 2006 Size effects in the deformation of sub-micron Au columns *Philos. Mag.* **86** 5567–79

[122] Frick C P, Clark B G, Orso S, Schneider A S and Arzt E 2008 Size effect on strength and strain hardening of small-scale [111] nickel compression pillars *Mater. Sci. Eng. A* **489** 319–29

[123] Parthasarathy T a., Rao S I, Dimiduk D M, Uchic M D and Trinkle D R 2007 Contribution to size effect of yield strength from the stochastics of dislocation source lengths in finite samples *Scr. Mater.* **56** 313–6

[124] Greer J and Nix W 2006 Nanoscale gold pillars strengthened through dislocation starvation *Phys. Rev. B* **73** 245410

[125] Cao A, Wei Y and Mao S X 2008 Alternating starvation of dislocations during plastic yielding in metallic nanowires *Scr. Mater.* **59** 219–22

[126] Shan Z W, Mishra R K, Syed Asif S a, Warren O L and Minor A M 2008 Mechanical annealing and source-limited deformation in submicrometre-diameter Ni crystals. *Nat. Mater.* **7** 115–9

[127] Greer J R and De Hosson J T M 2011 Plasticity in small-sized metallic systems: Intrinsic versus extrinsic size effect *Prog. Mater. Sci.* **56** 654–724

[128] Dou R and Derby B 2009 A universal scaling law for the strength of metal micropillars and nanowires *Scr. Mater.* **61** 524–7

[129] Dimiduk D M, Uchic M and Parthasarathy T A 2005 Size-affected single-slip behavior of pure nickel microcrystals *Acta Mater.* **53** 4065–77

[130] Greer J R, Oliver W C and Nix W D 2005 Size dependence of mechanical properties of gold at the micron scale in the absence of strain gradients *Acta Mater.* **53** 1821–30

[131] Brinckmann S, Kim J-Y and Greer J 2008 Fundamental Differences in Mechanical Behavior between Two Types of Crystals at the Nanoscale *Phys. Rev. Lett.* **100** 1–4

[132] Jennings A T and Greer J R 2011 Tensile deformation of electroplated copper nanopillars *Philos. Mag.* **91** 1108–20

[133] Peng C, Ganesan Y, Lu Y and Lou J 2012 Size dependent mechanical properties of single crystalline nickel nanowires *J. Appl. Phys.* **111** 063524

[134] Peng C, Zhan Y and Lou J 2012 Size-Dependent Fracture Mode Transition in Copper Nanowires. *Small* 1889–94

[135] Weinberger C R, Tucker G J and Foiles S M 2013 Peierls potential of screw dislocations in bcc transition metals: Predictions from density functional theory *Phys. Rev. B* **87** 054114

156

[136] Lu Y, Song J, Huang J Y and Lou J 2011 Fracture of Sub-20nm Ultrathin Gold Nanowires *Adv. Funct. Mater.* **21** 3982–9

[137] Frick C P, Clark B G, Orso S, Schneider a. S and Arzt E 2008 Size effect on strength and strain hardening of small-scale [111] nickel compression pillars *Mater. Sci. Eng. A* **489** 319–29

[138] Seo J-H, Park H S, Yoo Y, Seong T-Y, Li J, Ahn J-P, Kim B and Choi I-S 2013 Origin of size dependency in coherent-twin-propagation-mediated tensile deformation of noble metal nanowires. *Nano Lett.* **13** 5112–6

[139] Sedlmayr A 2012 *Experimental Investigations of Deformation Pathways in Nanowires* (Karlsruhe: Karlsruher Institut für Technologie)

[140] Bei H, Shim S, Pharr G M and George E P 2008 Effects of pre-strain on the compressive stress–strain response of Mo-alloy single-crystal micropillars *Acta Mater.* **56** 4762–70

[141] Seo J-H, Park H S, Yoo Y, Seong T-Y, Li J, Ahn J-P, Kim B and Choi I-S 2013 Origin of size dependency in coherent-twin-propagation-mediated tensile deformation of noble metal nanowires. *Nano Lett.* **13** 5112–6

[142] Weinberger C R, Jennings A T, Kang K and Greer J R 2012 Atomistic simulations and continuum modeling of dislocation nucleation and strength in gold nanowires *J. Mech. Phys. Solids* **60** 84–103

[143] Rabkin E and Srolovitz D J 2007 Onset of plasticity in gold nanopillar compression. *Nano Lett.* **7** 101–7

[144] Jennings A T, Li J and Greer J R 2011 Emergence of strain-rate sensitivity in Cu nanopillars: Transition from dislocation multiplication to dislocation nucleation *Acta Mater.* **59** 5627–37

[145] Wagner R S and Ellis W C 1964 Vapor-Liquid-Solid Mechanism of Single Crystal Growth *Appl. Phys. Lett.* **4** 89

[146] Menon M, Ponomareva I and Chernozatonskii L A 2004 Nanomechanics of silicon nanowires *Phys. Rev. B* **70** 125313

[147] Han X D, Zheng K, Zhang Y F, Zhang X N, Zhang Z and Wang Z L 2007 Low-Temperature In Situ Large-Strain Plasticity of Silicon Nanowires *Adv. Mater.* **19** 2112–8

[148] Smith D A, Holmberg V C and Korgel B A 2010 Flexible germanium nanowires: ideal strength, room temperature plasticity, and bendable semiconductor fabric. *ACS Nano* **4** 2356–62

[149] Schuh C a, Mason J K and Lund a C 2005 Quantitative insight into dislocation nucleation from high-temperature nanoindentation experiments. *Nat. Mater.* **4** 617–21

[150] Zheng H, Cao A, Weinberger C R, Huang J Y and Du K Discrete plasticity in sub-ten-nanometer-sized Au crystals 1–12

[151] Jennings A T, Li J and Greer J R 2011 Emergence of strain-rate sensitivity in Cu nanopillars: Transition from dislocation multiplication to dislocation nucleation *Acta Mater.* **59** 5627–37

[152] Lu Y, Song J, Huang J Y and Lou J 2011 Surface dislocation nucleation mediated deformation and ultrahigh strength in sub-10-nm gold nanowires *Nano Res.* **4** 1261–7

[153] Bei H, Gao Y, Shim S, George E and Pharr G 2008 Strength differences arising from homogeneous versus heterogeneous dislocation nucleation *Phys. Rev. B* **77** 060103

[154] Gerberich W W, Nelson J C, Lilleodden E T, Anderson P and Wyrobek J T 1996 Indentation induced dislocation nucleation: The initial yield point *Acta Mater.* **44** 3585–98

[155] Jennings A T, Weinberger C R, Lee S-W, Aitken Z H, Meza L and Greer J R 2013 Modeling dislocation nucleation strengths in pristine metallic nanowires under experimental conditions *Acta Mater.* **61** 2244–59

[156] Weinberger C R and Cai W 2012 Plasticity of metal nanowires *J. Mater. Chem.* **22** 3277

[157] Warner D H and Curtin W a. 2009 Origins and implications of temperature-dependent activation energy barriers for dislocation nucleation in face-centered cubic metals *Acta Mater.* **57** 4267–77

[158] Zhu T, Li J and Yip S 2004 Atomistic Study of Dislocation Loop Emission from a Crack Tip *Phys. Rev. Lett.* **93** 025503

[159] Uchic M D, Dimiduk D M, Florando J N and Nix W D 2004 Sample dimensions influence strength and crystal plasticity. *Science* **305** 986–9

[160] Volkert C a. and Lilleodden E T 2006 Size effects in the deformation of sub-micron Au columns *Philos. Mag.* **86** 5567–79

[161] Bahr D F, Wilson D E and Crowson D A 2011 Energy considerations regarding yield points during indentation *J. Mater. Res.* **14** 2269–75

[162] Ngan A H W, Zuo L and Wo P C 2006 Size dependence and stochastic nature of yield strength of micron-sized crystals: a case study on Ni3Al *Proc. R. Soc. A Math. Phys. Eng. Sci.* **462** 1661–81

[163] Jewell L and Davis B 2006 Review of absorption and adsorption in the hydrogen–palladium system *Appl. Catal. A Gen.* **310** 1–15

[164] Conrad H, Ertl G and Latta E E 1974 Adsorption of hydrogen on palladium single crystal surfaces *Surf. Sci.* **41** 435–46

[165] Flanagan T B and Oates W A 1991 The Palladium-Hydrogen System *Annu. Rev. Mater. Sci.* **21** 269–304

[166] Kibler L a, El-Aziz A M, Hoyer R and Kolb D M 2005 Tuning reaction rates by lateral strain in a palladium monolayer. *Angew. Chem. Int. Ed. Engl.* **44** 2080–4

[167] Tateishi N, Yahikozawa K, Nishimura K, Suzuki M, Iwanaga Y, Watanabe M, Enami E, Matsuda Y and Takasu Y 1991 Electrochemical properties of ultra-fine palladium particles for adsorption and absorption of hydrogen in an aqueous HClO4 solution *Electrochim. Acta* **36** 1235–40

[168] Jimenez G, Dillon E, Miller R, Massicotte F, Nesbit S and Craft A 2008 The role of hydrogen-exposure temperature on the mechanical properties of hydrogen-cycled palladium *Scr. Mater.* **59** 870–3

[169] Tripodi P, Avveduto A and Vinko J D 2010 Strain and resistivity of PdHx at hydrogen composition x>0.8 *J. Alloys Compd.* **500** 1–4

[170] Breger V and Gileadi E 1971 Adsorption and absorption of hydrogen in palladium *Electrochim. Acta* **16** 177–90

[171] Grochala W and Edwards P P 2004 Thermal Decomposition of the Non-Interstitial Hydrides for the Storage and Production of Hydrogen

[172] Yun S and Ted Oyama S 2011 Correlations in palladium membranes for hydrogen separation: A review *J. Memb. Sci.* **375** 28–45

[173] Offermans P, Tong H D, van Rijn C J M, Merken P, Brongersma S H and Crego-Calama M 2009 Ultralow-power hydrogen sensing with single palladium nanowires *Appl. Phys. Lett.* **94** 223110

[174] Im Y, Lee C, Vasquez R P, Bangar M a, Myung N V, Menke E J, Penner R M and Yun M 2006 Investigation of a single Pd nanowire for use as a hydrogen sensor. *Small* **2** 356–8

[175] Okuyama S and Mitobe Y 2000 Hydrogen gas sensing using a Pd-coated cantilever *Japanese J. ...* **3584**

[176] Goods S and Guthrie S 1992 Mechanical properties of palladium and palladium hydride *Scr. Metall. Mater.* **26** 561–5

[177] Zhirov G, Goltsova M and Shatalova G 2006 Hydrogen phase naklep influence on palladium grain and fine structures *Int. J. Hydrogen Energy* **31** 231–6

[178] Dillon E, Jimenez G, Davie A, Bulak J, Nesbit S and Craft A 2009 Factors influencing the tensile strength, hardness, and ductility of hydrogen-cycled palladium *Mater. Sci. Eng. A* **524** 89–97

159

[179] Ho E, Goldberg H A, Weatherly G C and Manchester F D 1979 An in situ electron microscope study of precipitation in palladium-hydrogen alloys *Acta Metall.* **27** 841–53

[180] Jamieson H C, Weatherly G C and Manchester F D 1976 The β → α phase transformation in palladium-hydrogen alloys *J. Less Common Met.* **50** 85–102

[181] Jeon K J, Jeun M, Lee E, Lee J M, Lee K-I, von Allmen P and Lee W 2008 Finite size effect on hydrogen gas sensing performance in single Pd nanowires. *Nanotechnology* **19** 495501

[182] Kishimoto S, Inoue M, Yoshida N and Flanagan T B 1986 Solution of hydrogen in thin palladium films *J. Chem. Soc. Faraday Trans. 1 Phys. Chem. Condens. Phases* **82** 2175

[183] Pundt A 2004 Hydrogen in Nano-sized Metals *Adv. Eng. Mater.* **6** 11–21

[184] Kuji T, Matsumura Y, Uchida H and Aizawa T 2002 Hydrogen absorption of nanocrystalline palladium *J. Alloys Compd.* **330-332** 718–22

[185] Gall K, Diao J and Dunn M L 2004 The Strength of Gold Nanowires *Nano Lett.* **4** 2431–6

[186] Xu F, Qin Q, Mishra A, Gu Y and Zhu Y 2010 Mechanical properties of ZnO nanowires under different loading modes *Nano Res.* **3** 271–80

[187] Wen B, Sader J and Boland J 2008 Mechanical Properties of ZnO Nanowires *Phys. Rev. Lett.* **101** 175502

[188] Hara S, Izumi S and Sakai S 2011 Reaction pathway analysis for dislocation nucleation from a Ni surface step Reaction pathway analysis for dislocation nucleation from a Ni surface **093507**

[189] Brochard S, Beauchamp P, Grilhé J, Spmi U F R S, Marie B and Cedex F C 2001 Combination of Continuum and Atomistic Approaches for the Study of Dislocation Nucleation from Atomic Size Surface Defects Sandrine Brochard, Pierre Beauchamp and Jean Grilhé **677** 1–6

[190] Chen L, Richter G, Sullivan J and Gianola D 2012 Lattice Anharmonicity in Defect-Free Pd Nanowhiskers *Phys. Rev. Lett.* **109** 1–5

[191] Zhu Y and Espinosa H D 2005 An electromechanical material testing system for in situ electron microscopy and applications. *Proc. Natl. Acad. Sci. U. S. A.* **102** 14503–8

[192] Flubacher P, Leadbetter A J and Morrison J A 1959 The heat capacity of pure silicon and germanium and properties of their vibrational frequency spectra *Philos. Mag.* **4** 273–94

[193] Swenson C A 1983 Recommended Values for the Thermal Expansivity of Silicon from 0 to 1000 K *J. Phys. Chem. Ref. Data* **12** 179

[194] Lyon K G, Salinger G L, Swenson C A and White G K 1977 Linear thermal expansion measurements on silicon from 6 to 340 K *J. Appl. Phys.* **48** 865

[195] Glazov V and Pashinkin A 2001 The thermophysical properties (heat capacity and thermal expansion) of single-crystal silicon *High Temp.* **39** 443–9

[196] Chen L, Richter G, Sullivan J and Gianola D 2012 Lattice Anharmonicity in Defect-Free Pd Nanowhiskers *Phys. Rev. Lett.* **109** 125503

[197] Eberl C, Gianola D S and Hemker K J 2008 Mechanical Characterization of Coatings Using Microbeam Bending and Digital Image Correlation Techniques *Exp. Mech.* **50** 85–97

[198] Eberl C, Thompson R, Gianola D, Sharpe W J and Hemker K 2006 Digital image correlation and tracking *MatLabCentral, Mathworks file Exch. server, FileID* **12413**

[199] Gianola D S and Eberl C 2009 Micro- and nanoscale tensile testing of materials *JOM* **61** 24–35

[200] Utke I, Friedli V, Fahlbusch S, Hoffmann S, Hoffmann P and Michler J 2006 Tensile Strengths of Metal-Containing Joints Fabricated by Focused Electron Beam Induced Deposition *Adv. Eng. Mater.* **8** 155–7

[201] Friedli V, Utke I, Mølhave K and Michler J 2009 Dose and energy dependence of mechanical properties of focused electron-beam-induced pillar deposits from Cu(C5HF6O2)2. *Nanotechnology* **20** 385304

[202] Liang L, Zeng D, Wei X, Chen Q and Li X 2009 Strength Analysis of Clamping in Micro/Nano Scale Experiments *Acta Mech. Solida Sin.* **22** 584–92

[203] Murphy K F, Chen L Y and Gianola D S 2013 Effect of organometallic clamp properties on the apparent diversity of tensile response of nanowires. *Nanotechnology* **24** 235704

[204] Karim S, Balogh A G and Ensinger W 2006 Morphological evolution of Au nanowires *Nanotechnology* **17** 5954–9

[205] Toimil Molares M E, Balogh A G, Cornelius T W, Neumann R and Trautmann C 2004 Fragmentation of nanowires driven by Rayleigh instability *Appl. Phys. Lett.* **85** 5337

[206] Burke H H and Herman I P 1993 Temperature dependence of Raman scattering in Ge1-xSix alloys *Phys. Rev. B* **48** 15016–24

[207] Hart T R, Aggarwal R L and Lax B 1970 Temperature Dependence of Raman Scattering in Silicon *Phys. Rev. B* **1** 638–42

[208] Qin Q and Zhu Y 2013 Temperature control in thermal microactuators with applications to in-situ nanomechanical testing *Appl. Phys. Lett.* **102** 013101

[209] Hickey R, Kujath M and Hubbard T 2002 Heat transfer analysis and optimization of two-beam microelectromechanical thermal actuators *J. Vac. Sci. Technol. A Vacuum, Surfaces, Film.* **20** 971

[210] Guo H, Chen K, Oh Y, Wang K, Dejoie C, Syed Asif S A, Warren O L, Shan Z W, Wu J and Minor A M 2011 Mechanics and dynamics of the strain-induced M1-M2 structural phase transition in individual VO_2 nanowires. *Nano Lett.* **11** 3207–13

[211] Chisholm C, Bei H, Lowry M B, Oh J, Syed Asif S a., Warren O L, Shan Z W, George E P and Minor a. M 2012 Dislocation starvation and exhaustion hardening in Mo alloy nanofibers *Acta Mater.* **60** 2258–64

[212] Minor A M, Asif S a S, Shan Z, Stach E a, Cyrankowski E, Wyrobek T J and Warren O L 2006 A new view of the onset of plasticity during the nanoindentation of aluminium. *Nat. Mater.* **5** 697–702

[213] Sedlmayr A, Bitzek E, Gianola D S, Richter G, Mönig R and Kraft O 2012 Existence of two twinning-mediated plastic deformation modes in Au nanowhiskers *Acta Mater.* **60** 3985–93

[214] Rayne J 1960 Elastic Constants of Palladium from 4.2-300°K *Phys. Rev.* **118** 1545–9

[215] Guo J-G and Zhao Y-P 2007 The size-dependent bending elastic properties of nanobeams with surface effects *Nanotechnology* **18** 295701

[216] Diao J, Gall K and Dunn M L 2003 Surface-stress-induced phase transformation in metal nanowires. *Nat. Mater.* **2** 656–60

[217] Masumoto H, Saitô H and Kadowaki S 1967 Young's Modulus of Single Crystals of Palladium at High Temperatures *Sci. reports Res. Institutes, Tohoku Univ. Ser. A, Physics, Chem. Metall.* **19** 294–303

[218] Ryu S, Kang K and Cai W 2011 Predicting the dislocation nucleation rate as a function of temperature and stress *J. Mater. Res.* **26** 2335–54

[219] Wu H a. 2006 Molecular dynamics study on mechanics of metal nanowire *Mech. Res. Commun.* **33** 9–16

[220] Gu M, Sun C, Chen Z, Au Yeung T, Li S, Tan C and Nosik V 2007 Size, temperature, and bond nature dependence of elasticity and its derivatives on extensibility, Debye temperature, and heat capacity of nanostructures *Phys. Rev. B* **75** 125403

[221] Kern K 1994 Thermal roughening of surfaces: experimental aspects *Phase Transitions and Adsorbate Restructuring at Metal Surfaces, The Chemical Physics of Solid Surfaces* (Amsterdam: Elsevier) pp 291–340

[222] Mason J, Lund a. and Schuh C 2006 Determining the activation energy and volume for the onset of plasticity during nanoindentation *Phys. Rev. B* **73** 054102

[223] Wo P C, Zuo L and Ngan a. H W 2011 Time-dependent incipient plasticity in Ni3Al as observed in nanoindentation *J. Mater. Res.* **20** 489–95

[224] Foiles S, Baskes M and Daw M 1986 Embedded-atom-method functions for the fcc metals Cu, Ag, Au, Ni, Pd, Pt, and their alloys *Phys. Rev. B* **33** 7983–91

[225] Brochard S, Hirel P, Pizzagalli L and Godet J 2010 Elastic limit for surface step dislocation nucleation in face-centered cubic metals: Temperature and step height dependence *Acta Mater.* **58** 4182–90

[226] Salehinia I and Bahr D F 2012 The impact of a variety of point defects on the inception of plastic deformation in dislocation-free metals *Scr. Mater.* **66** 339–42

[227] Nascimento V, Soares E, de Carvalho V, Lopes E, Paniago R and de Castilho C 2003 Thermal expansion of the Ag(110) surface studied by low-energy electron diffraction and density-functional theory *Phys. Rev. B* **68** 245408

[228] Aubry S, Kang K, Ryu S and Cai W 2011 Energy barrier for homogeneous dislocation nucleation: Comparing atomistic and continuum models *Scr. Mater.* **64** 1043–6

[229] Schuh C a. and Lund A C 2011 Application of nucleation theory to the rate dependence of incipient plasticity during nanoindentation *J. Mater. Res.* **19** 2152–8

[230] Schuh C a, Mason J K and Lund a C 2005 Quantitative insight into dislocation nucleation from high-temperature nanoindentation experiments. *Nat. Mater.* **4** 617–21

[231] Hara S, Izumi S and Sakai S 2009 Reaction pathway analysis for dislocation nucleation from a Ni surface step *J. Appl. Phys.* **106** 093507

[232] Brochard S, Beauchamp P and Grilhé J 2000 Dislocation nucleation from surface steps: Atomistic simulation in aluminium *Philos. Mag. A* **80** 503–24

[233] Henkelman G, Uberuaga B P and Jónsson H 2000 A climbing image nudged elastic band method for finding saddle points and minimum energy paths *J. Chem. Phys.* **113** 9901

[234] Vanden-Eijnden E and Venturoli M 2009 Revisiting the finite temperature string method for the calculation of reaction tubes and free energies. *J. Chem. Phys.* **130** 194103

[235] Weinberger C R and Cai W 2008 Surface-controlled dislocation multiplication in metal micropillars. *Proc. Natl. Acad. Sci. U. S. A.* **105** 14304–7

[236] Zhang Y and Huang H 2009 Do Twin Boundaries Always Strengthen Metal Nanowires? *Nanoscale Res. Lett.* **4** 34–8

[237] Gerberich W W, Venkataraman S K, Huang H, Harvey S E and Kohlstedt D L 1995 The injection of plasticity by millinewton contacts *Acta Metall. Mater.* **43** 1569–76

[238] Chiu Y L and Ngan A H W 2002 A TEM investigation on indentation plastic zones in Ni 3 Al(Cr,B) single crystals **50** 2677–91

[239] Zuo L, Ngan A and Zheng G 2005 Size Dependence of Incipient Dislocation Plasticity in Ni3Al *Phys. Rev. Lett.* **94** 095501

[240] Basu J and Bhattacharyya T K 2012 Microelectromechanical system cantilever-based frequency doublers *J. Intell. Mater. Syst. Struct.* **24** 240–6

[241] Kong S, Zhou S, Nie Z and Wang K 2008 The size-dependent natural frequency of Bernoulli–Euler micro-beams *Int. J. Eng. Sci.* **46** 427–37

[242] Afanasyev K a. and Sansoz F 2007 Strengthening in Gold Nanopillars with Nanoscale Twins *Nano Lett.* **7** 2056–62

[243] Christian J W and Vítek V 1970 Dislocations and stacking faults *Reports Prog. Phys.* **33** 307–411

[244] Anderson P M and Li Z 2001 A Peierls analysis of the critical stress for transmission of a screw dislocation across a coherent, sliding interface *Mater. Sci. Eng. A* **319-321** 182–7

[245] Wen Y-H, Huang R, Zhu Z-Z and Wang Q 2012 Mechanical properties of platinum nanowires: An atomistic investigation on single-crystalline and twinned structures *Comput. Mater. Sci.* **55** 205–10

[246] Niekiel F, Bitzek E and Spiecker E 2014 Combining atomistic simulation and X-ray diffraction for the characterization of nanostructures: a case study on fivefold twinned nanowires. *ACS Nano* **8** 1629–38

[247] Wan J, Fan Y L, Gong D W, Shen S G and Fan X Q 1999 Surface relaxation and stress of fcc metals: Cu, Ag, Au, Ni, Pd, Pt, Al and Pb *Model. Simul. Mater. Sci. Eng.* **7** 189–206

[248] Yue Y, Eres G, Wang X and Guo L 2009 Characterization of thermal transport in micro/nanoscale wires by steady-state electro-Raman-thermal technique *Appl. Phys. A* **97** 19–23

[249] Hillier J 1948 On the Investigation of Specimen Contamination in the Electron Microscope *J. Appl. Phys.* **19** 226

[250] Ennos A E 1953 The origin of specimen contamination in the electron microscope *Br. J. Appl. Phys.* **4** 101–6

[251] Likhtman V I and Shchukin E D 1960 SURFACE PHENOMENA IN THE DEFORMATION AND FRACTURE OF METALS *Russ. Chem. Rev.* **29** 576–89

164

[252] Rehbinder P and Shchukin E 1972 Surface phenomena in solids during deformation and fracture processes *Prog. Surf. Sci.* **3** 97–188

[253] Doyle A M, Shaikhutdinov S K, Jackson S D and Freund H-J 2003 Hydrogenation on metal surfaces: why are nanoparticles more active than single crystals? *Angew. Chem. Int. Ed. Engl.* **42** 5240–3

[254] Moravec T J 1981 Electron spectroscopy of ion beam and hydrocarbon plasma generated diamondlike carbon films *J. Vac. Sci. Technol.* **18** 226

[255] Anttila A, Koskinen J, Lappalainen R, Hirvonen J-P, Stone D and Paszkiet C 1987 Comparison of diamondlike coatings deposited with C+ and various hydrocarbon ion beams *Appl. Phys. Lett.* **50** 132

[256] Whitmell D S and Williamson R 1976 The deposition of hard surface layers by hydrocarbon cracking in a glow discharge *Thin Solid Films* **35** 255–61

[257] Fountzoulas C G 1994 Mechanical properties of Si-diamondlike carbon films formed by ion beam assisted deposition *J. Vac. Sci. Technol. B Microelectron. Nanom. Struct.* **12** 977

[258] Robertson J 1994 Diamond-like carbon *Pure Appl. Chem.* **66** 1789–96

[259] Aisenberg S 1971 Ion-Beam Deposition of Thin Films of Diamondlike Carbon *J. Appl. Phys.* **42** 2953

[260] Beutier G, Verdier M, Boissieu M De, Gilles B, Livet F, Richard M-I, Cornelius T W, Labat S and Thomas O 2013 Combined coherent x-ray micro-diffraction and local mechanical loading on copper nanocrystals *J. Phys. Conf. Ser.* **425** 132003

[261] Cornelius T W, Davydok a, Jacques V L R, Grifone R, Schülli T, Richard M I, Beutier G, Verdier M, Metzger T H, Pietsch U and Thomas O 2012 In situ three-dimensional reciprocal-space mapping during mechanical deformation. *J. Synchrotron Radiat.* **19** 688–94

[262] Pfeifer M a, Williams G J, Vartanyants I a, Harder R and Robinson I K 2006 Three-dimensional mapping of a deformation field inside a nanocrystal. *Nature* **442** 63–6

[263] Rodrigues M S, Cornelius T W, Scheler T, Mocuta C, Malachias a., Magalhães-Paniago R, Dhez O, Comin F, Metzger T H and Chevrier J 2009 In situ observation of the elastic deformation of a single epitaxial SiGe crystal by combining atomic force microscopy and micro x-ray diffraction *J. Appl. Phys.* **106** 103525

[264] Haag S, Richard M and Welzel U 2013 Concentration and Strain Fields inside a Ag/Au Core–Shell Nanowire Studied by Coherent X-ray Diffraction *Nano ...*

[265] Chen M 2008 Mechanical Behavior of Metallic Glasses: Microscopic Understanding of Strength and Ductility *Annu. Rev. Mater. Res.* **38** 445–69

165

[266] Tripodi P, Di Gioacchino D and Vinko J D 2009 AC electrical resistance measurements of PdHx samples versus composition x *J. Alloys Compd.* **486** 55–9

[267] Flanagan T B and Lewis F a. 1959 Hydrogen absorption by palladium in aqueous solution *Trans. Faraday Soc.* **55** 1400

[268] Wen M and Li Z 2012 Thermally activated process of homogeneous dislocation nucleation and hydrogen effects : An atomistic study *Comput. Mater. Sci.* **54** 28–31

[269] Kirchheim R 2010 Revisiting hydrogen embrittlement models and hydrogen-induced homogeneous nucleation of dislocations *Scr. Mater.* **62** 67–70

[270] Barnoush A and Vehoff H 2010 Recent developments in the study of hydrogen embrittlement: Hydrogen effect on dislocation nucleation *Acta Mater.* **58** 5274–85

[271] Baselt D R, Fruhberger B, Klaassen E, Cemalovic S and Jr C L B 2003 Design and performance of a microcantilever-based hydrogen sensor **88** 120–31

[272] Chou Y-I, Chiang H-C and Wang C-C 2008 Study on Pd functionalization of microcantilever for hydrogen detection promotion *Sensors Actuators B Chem.* **129** 72–8

[273] Iannuzzi D, Slaman M, Rector J, Schreuders H, Deladi S and Elwenspoek M 2007 A fiber-top cantilever for hydrogen detection *Sensors Actuators B Chem.* **121** 706–8

[274] Taylor J R 1982 Propagation of Uncertainties *An Introduction to Error Analysis* (Sausalito: University Science Books)

[275] Bernstein N and Tadmor E 2004 Tight-binding calculations of stacking energies and twinnability in fcc metals *Phys. Rev. B* **69** 094116

[276] Dillamore I L and Smallman R E 1965 The stacking-fault energy of F.C.C. metals *Philos. Mag.* **12** 191–3

[277] Park H, Gall K and Zimmerman J 2005 Shape Memory and Pseudoelasticity in Metal Nanowires *Phys. Rev. Lett.* **95** 255504

[278] Park H S, Gall K and Zimmerman J a. 2006 Deformation of FCC nanowires by twinning and slip *J. Mech. Phys. Solids* **54** 1862–81

[279] Zheng H, Cao A, Weinberger C R, Huang J Y, Du K, Wang J, Ma Y, Xia Y and Mao S X 2010 Discrete plasticity in sub-10-nm-sized gold crystals. *Nat. Commun.* **1** 144

[280] Seo J, Yoo Y, Park N, Yoon S, Lee H, Han S, Lee S, Seong T, Lee S, Lee K, Cha P, Park H S, Kim B and Ahn J 2011 Superplastic Deformation of Defect-Free Au Nanowires via Coherent Twin Propagation 3499–502

[281] Ding W, Dikin D a., Chen X, Piner R D, Ruoff R S, Zussman E, Wang X and Li X 2005 Mechanics of hydrogenated amorphous carbon deposits from electron-beam-induced deposition of a paraffin precursor *J. Appl. Phys.* **98** 014905

[282] Wang L, Bei H, Li T L, Gao Y F, George E P and Nieh T G 2011 Determining the activation energies and slip systems for dislocation nucleation in body-centered cubic Mo and face-centered cubic Ni single crystals *Scr. Mater.* **65** 179–82